MATEMATICKO-FYZIKÁLNÍ
FAKULTA
Univerzita Karlova

DISERTAČNÍ PRÁCE

Klaudia Horváth

Studium pokročilých hořčíkových slitin s vysokou pevností pomocí *in-situ* metod

Katedra fyziky materiálů

Vedoucí disertační práce: doc. Ing. Patrik Dobroň, Ph.D.

Studijní program: Fyzika

Studijní obor: Fyzika kondenzovaných soustav a materiálů

Praha 2019

FACULTY
OF MATHEMATICS
AND PHYSICS
Charles University

DOCTORAL THESIS

Klaudia Horváth

Study of advanced high strength magnesium alloys by *in-situ* techniques

Department of Physics of Materials

Supervisor of the doctoral thesis: doc. Ing. Patrik Dobroň, Ph.D.

Study programme: Physics

Specialization: Physics of condensed matter and materials

Prague 2019

I declare that I carried out this doctoral thesis independently, and only with the cited sources, literature and other professional sources.

I understand that my work relates to the rights and obligations under the Act No. 121/2000 Coll., the Copyright Act, as amended, in particular the fact that the Charles University has the right to conclude a license agreement on the use of this work as a school work pursuant to Section 60 paragraph 1 of the Copyright Act.

In Prague 13/06/2019

Klaudia Horváth

Acknowledgement

First of all, I would like to express my gratitude above all to my supervisor Doc. Patrik Dobroň for introducing me to the field of materials science and for his support and guidance throughout my studies since my bachelor years. My sincere thanks go to Doc. Kristián Máthis, who among his many duties has found some time to provide help and advice.

I am grateful to all my colleagues at the Department of Physics of Materials for creating a wealthy atmosphere during work and for the interesting discussions. I am especially indebted to Dr. Daria Drozdenko for her helpful ideas, support and help during writing my thesis. Without her, the present work would be less colorful. I also appreciate the help of Dr. Jan Čapek and Dr. Gergely Farkas with the diffraction data evaluation.

I would thank to Dr. Gerardo Garcés Plaza for providing the experimental material and to Dr. Domonkos Tolnai for his help with the synchrotron measurements at DESY.

The last but not least, I owe more than thanks to my parents, my friends and to my fiancée for their never-ending support and for their faith in me.

This work was financially supported by the Charles University Grant Agency (GAUK) under the research project number 1262217.

Název práce: Studium pokročilých hořčíkových slitin s vysokou pevností pomocí *in-situ* metod

Autor: RNDr. Klaudia Horváth

Katedra: Katedra fyziky materiálů, Matematicko-fyzikální fakulta, Univerzita Karlova

Vedoucí disertační práce: doc. Ing. Patrik Dobroň, Ph.D., Katedra fyziky materiálů

Abstrakt:

Hlavním cílem disertační práce bylo stanovení aktivních deformačních mechanismů v moderních hořčíkových slitinách s vysokou pevností s využitím pokročilých *in-situ* metod umožňující vysoké rozlišení v čase a v prostoru. Zkoumalo se deformační chování dvou extrudovaných Mg-LPSO slitin s různým objemovým podílem LPSO (long-period stacking order) fáze v průběhu deformace v tahu při pokojové teplotě a v tlaku při pokojové teplotě a při teplotách 200 °C, 300 °C a 350 °C. Výsledky získané pomocí *in-situ* metod akustické emise a difrakce synchrotronového záření byly ověřeny pomocí transmisní a rastrovací elektronové mikroskopie, zejména zobrazováním zpětně odražených elektronů a difrakcí zpětně odražených elektronů.

Z dosažených výsledků vyplývá, že jak teplota, tak i obsah LPSO fáze významně ovlivňují plasticitu hořčíkové matrice, zejména aktivaci tahových dvojčat a nebazálního skluzu. Navíc mají velký vliv na tvorbu deformačních vybočení (kinking) v LPSO fázi.

Klíčová slova:

Mg-LPSO slitiny, deformační mechanismy, akustická emise, difrakce synchrotronového záření, *in-situ* metody.

Title: Study of advanced high strength magnesium alloys by *in situ* techniques

Author: RNDr. Klaudia Horváth

Department / Institute: Department of Physics of Materials, Faculty of Mathematics and Physics, Charles University

Supervisor of the doctoral thesis: doc. Ing. Patrik Dobroň, Ph.D., Department of Physics of Materials

Abstract:

The aim of the present doctoral thesis was to reveal the active deformation mechanisms in novel high strength magnesium (Mg) alloys using advanced *in-situ* techniques with high time and space resolutions. The deformation behavior of two extruded Mg-LPSO alloys with a different volume fraction of the long-period stacking ordered (LPSO) phase was investigated in tension and compression at room temperature and in compression at 200 °C, 300 °C, and 350 °C. In order to support the results obtained by *in-situ* acoustic emission and synchrotron diffraction methods, detailed microstructure investigation was provided by transmission and scanning electron microscopy, particularly the backscattered electron imaging and electron backscatter diffraction technique were used.

The results indicate that both temperature and the LPSO phase content significantly influence the plasticity of the magnesium matrix, particularly they affect the activation of extension twins and non-basal slip. Moreover, both parameters have a high impact on the formation of the deformation kinks in the LPSO phase.

Keywords:

Mg-LPSO alloys, deformation mechanisms, acoustic emission, synchrotron diffraction, *in-situ* methods.

Contents

List of symbols and abbreviations

a, c ..... lattice parameter in a hexagonal close-packed structure

A/D converter..... analog to digital converter

AE ..... acoustic emission

ASK..... adaptive sequential k-means procedure

b..... Burger´s vector

bcc ..... body-centered cubic

BSE ..... backscattered electrons

c^*..... lattice parameter of the reciprocal lattice

CI..... confidence index

CRSS (τ_{CRSS})..... critical resolved shear stress

CYS..... compressive yield strength

d..... grain size

$d_{0,hkl}$ ..... planar spacing of the *hkl* plane the stress-free (initial) crystal

d_{hkl} ..... planar spacing of the *hkl* plane (lattice spacing) in the deformed material

DESY ..... Deutsches Elektronen-Synchrotron

DRX ..... dynamically-recrystallized

DS..... directionally solidified

E ..... energy

EBSD ..... electron backscatter diffraction

ED ..... extrusion direction

EDX ..... energy dispersive X-ray

ER..... extrusion ratio

F ..... applied force

fcc ..... face-centered cubic

f_{DRX}, $f_{non\text{-}DRX}$, f_{LPSO}..... volume fraction of the recrystallized grains, non-recrystallized grains, and LPSO phase

f_m..... median frequency

f_t ..... sampling frequency

FEG ..... field emission gun

g..... magnitude of twinning

G..... shear modulus

GOS ..... grain orientation spread

h, k, l ..... Miller indices

HAADF-STEM ..... high-angle annular dark-field imaging in scanning transmission electron microscopy

hcp ..... hexagonal closed packed

HDT ..... hit definition time or dead time

HR-TEM ..... high-resolution transmission electron microscopy

IPF ..... inverse pole figure

k ..... material constant (Hall-Petch equation)

$\vec{k}$ ..... diffracted wave vector

$\overrightarrow{k_0}$ ..... initial wave vector

LPSO ..... long-period stacking ordered

m ..... Schmid factor

M ..... Taylor factor

Mg ..... magnesium

MMC ..... metal matrix composite

m.r.d. ..... multiple of random density

OIM ..... orientation image map

PAC ..... Physical Acoustic Corporation

PSD ..... power spectral density

$\vec{q}$ ..... diffraction vector

RE ..... rare earth

RMS ..... root mean square

RT ..... room temperature

S ..... shear plane

S_0 ..... initial diameter of a single crystalline cylinder

S_1 ..... initial cross-section during the extrusion process

S_2 ..... final cross-section during the extrusion process

SAED ..... selected area electron diffraction

SE ..... secondary electrons

SEM ..... scanning electron microscopy

STEM ..... scanning transmission electron microscopy

TEM ..... transmission electron microscopy

TVF ..... twin volume fraction

TYS ..... tensile yield strength

U_r ..... reference voltage

UCS ..... ultimate compression strength

UTS ..... ultimate tensile strength

ε_{hkl} ..... lattice strain

η_1, η_2 ..... shear direction of twinning

θ_{hkl} ..... Bragg angle

κ_1, κ_2 ..... invariant planes of twinning

λ ..... angle between the loading axis and the glide direction or the wavelength of the X-rays

ρ_D ..... dislocation density

σ ..... applied stress

σ_0 ..... friction stress

$\sigma_{0.2}$ ..... yield strength

$\sigma_{DRX}, \sigma_{non-DRX}, \sigma_{LPSO}$ ... contribution to the yield strength of the recrystallized grains, non-recrystallized grains, and LPSO phase

φ ..... angle between the loading axis and the normal to the slip plane

Ψ ..... azimuthal angle

Preface

The global trends motivate the transportation industry to fabricate light, environmentally friendly, safe and cheap vehicles. The leader manufacturers are mainly concentrating on weight reduction since it affects fuel consumption and, thus, the CO_2 emission [1]. It was already reported that reducing the weight of the vehicles by 10% results in reduced fuel consumption by approximately 5 % [2]. Magnesium (Mg) alloys, owing to excellent strength to weight ratio, represent a highly interesting material for the transportation industry. At the same time, their widespread application is limited by several factors, as generally low formability at ambient temperatures, low yield strength, degradation of mechanical properties above 200 °C or poor creep resistance. Moreover, their low corrosion resistance and flammability require protective atmosphere or coatings, which result in relatively high production costs.

Progress in the development of Mg alloys brought already useful results and they are effectively applied in industry. For example, in 2015 the ban to use Mg alloys in aircraft was lifted by the Society of Automotive Engineers (SAE) after satisfying the flammability performance requirements by the Federal Aviation Administration (FAA) [3]. An Italian seat manufacturer, Geven, has already integrated the Elektron® 43 (WE43C) alloy containing Y and Nd into their seats.

The recently developed Mg-Y-Zn alloys received significant attention thanks to their excellent mechanical properties at both room and elevated temperatures [4–9]. The addition of yttrium (Y) and rare earth (RE) elements in a ratio of 2:1 leads to a formation of a long-period stacking ordered (LPSO) phase [10], what has been found to be beneficial for the strengthening of Mg alloys at ambient temperatures [11–14].

The majority of the studies is focused on alloys with at least 2 at.% of Y and/or RE elements. However, there is a new policy proposal in Europe, USA, and Japan [15] to reduce the content of the RE elements since their future availability is not guaranteed. Therefore, two Mg-LPSO alloys: one with a reduced and one with an increased amount of alloying element, compared to the above-mentioned alloy, have been chosen to investigate the influence of the amount of alloying elements, and thus the amount of the LPSO phase on the resulting mechanical properties. The detailed analysis of their deformation mechanisms at room and elevated temperatures is of key importance for the further expansion of their application. However, the experimental

study of the deformation mechanisms in Mg-LPSO alloys is rather difficult thanks to their complex microstructure. Generally, the microscopic methods examine only a small volume of the material and the results are barely representative for the whole specimen. Statistically representative data for complex characterization of the plasticity of Mg alloys can be obtained by the combination of *in-situ* acoustic emission and diffraction experiments [16–18].

The main advantage of the acoustic emission technique is its fine time resolution and sensitivity to twin nucleation and collective dislocation motion. Nevertheless, the differentiation between particular signal types and the determination of the respective source is a difficult task due to their simultaneous appearance. A recently developed statistical method, the so-called adaptive sequential k-means (ASK) analysis enables to determine the dominant deformation mechanism at various stages of deformation [19]. Diffraction experiments, as well as high-resolution microstructure observations, can complete the full picture to understand the deformation behavior of the Mg-LPSO alloys.

In the present work, advanced techniques with high time and space resolution are employed to analyze the deformation behavior of Mg alloys with respect to the volume fraction of the LPSO phase.

1. Theoretical background

1.1. Hexagonal closed packed structure

Magnesium (Mg), one of the lightest construction metals, has a hexagonal closed packed (*hcp*) crystal lattice, as shown in Fig. 1.1. Its structure is characterized by six-fold symmetry along the *c*-axis and three equivalent directions a_1, a_2, and a_3 perpendicular to the *c*-axis. The lattice parameters of the pure Mg at room temperature (RT) are c = 0.52105 nm and a = 0.32092 nm. In materials with an *hcp* lattice, the plastic deformation strongly depends on the ratio of the crystallographic axes c to a [20]. The ideal ratio of c/a equals to $\sqrt{\frac{8}{3}} \cong 1.633$. This is the closest configuration of atoms in an *hcp* lattice. If the ratio of c/a is higher than the ideal value, the atomic density of non-basal lattice planes decreases and causes a larger distance between the atoms. Thus, the slip takes place primarily on the basal plane. This is the case for example in zinc and cadmium. If the ratio of c/a is lower than the ideal value, e.g. in titanium, zirconium, and beryllium, the slip takes place on the prismatic and pyramidal slip planes. The ratio of c/a ratio of the pure Mg is very close to the ideal value and equals to 1.623.

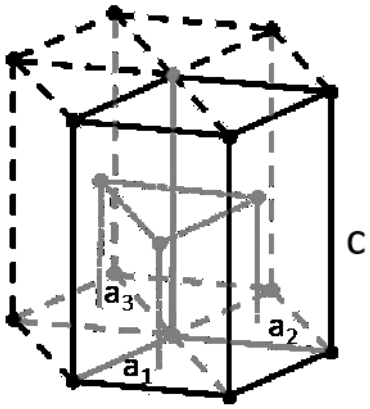

Fig. 1.1. Hexagonal closed packed lattice.

1.2. Plastic deformation of magnesium alloys

Plastic deformation occurs when the material undergoes non-reversible changes of shape in response to the applied force [21]. The basic mechanisms of plastic deformation in metals with *hcp* structure are dislocation slip and twinning. Slip is a shift of one part of a crystal relative to the other part, realized by moving a dislocation, whereby deformation twins are formed by highly coordinated individual atom displacement [22].

Two primary types of dislocations are present in crystalline materials: edge and screw dislocations, shown in Fig. 1.2. Their generation and interaction can significantly influence the deformation behavior of the material.

The two basic types of dislocation movements are glide and climb. Glide occurs when the dislocation moves on a plane defined by its line and Burger´s vector. It is the conservative motion of dislocations. The non-conservative motion of dislocations is the climb when the dislocation moves out of the glide surface.

Compared to single crystals, the plastic deformation of polycrystalline materials is strongly affected by (i) the grain boundaries, which behave like an obstacle for dislocation motion, and (ii) the orientation of grains, i.e. orientation of particular planes from grain to grain [23].

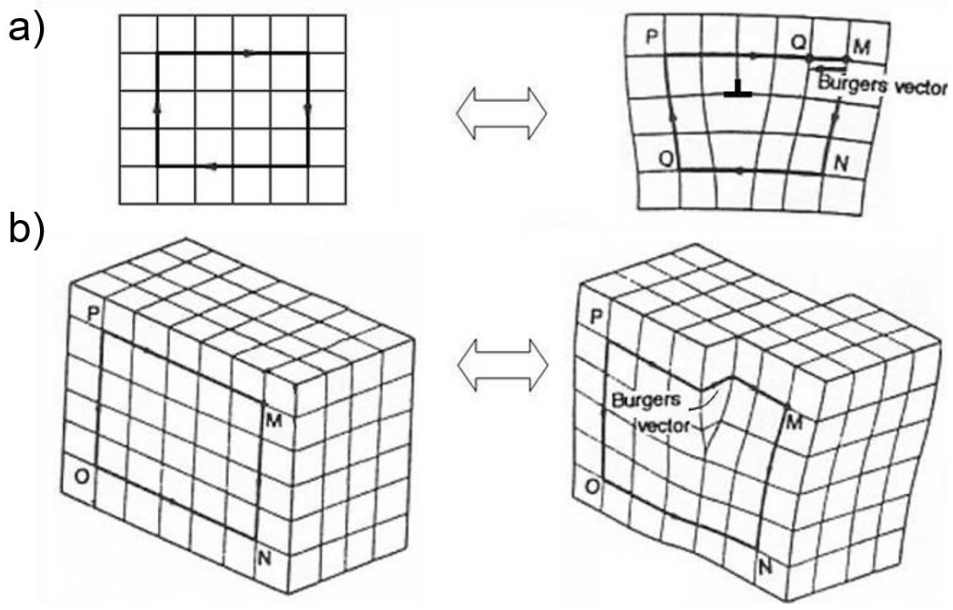

Fig. 1.2. a) Edge and b) screw dislocation type [24].

Ductility and strength of the material are two characteristic values of the plastic deformation. The first one measures the ability of the material to undergo significant deformation before fracture and the second one deals with the ability to bear the applied load without failure. The macroscopic plastic deformation starts when the material reaches its yield strength. In materials without upper and lower yielding behavior, the yield strength is defined as the stress corresponding to the strain of 0.2 %.

1.2.1. Dislocation slip

A slip occurs on certain preferred planes, which owe (i) the lowest critical resolved shear stress (CRSS) and (ii) the highest density of atoms; and proceeds in the direction in which the atoms are most closely spaced. The slip systems in *hcp* metals are listed in Table 1.1. and shown in Fig. 1.3.

Table 1.1. The main slip systems in Mg [20]

Plane	**Notation**	**Direction**	**Number of independent modes**
Basal	$(0002)\langle 11\bar{2}0\rangle$	<a>	2
Prismatic	$\{1\bar{1}00\}\langle 11\bar{2}0\rangle$	<a>	2
1st pyramidal	$\{1\bar{1}01\}\langle 11\bar{2}0\rangle$	<a>	4
2nd pyramidal	$\{11\bar{2}2\}\langle 11\bar{2}3\rangle$	<c+a>	5

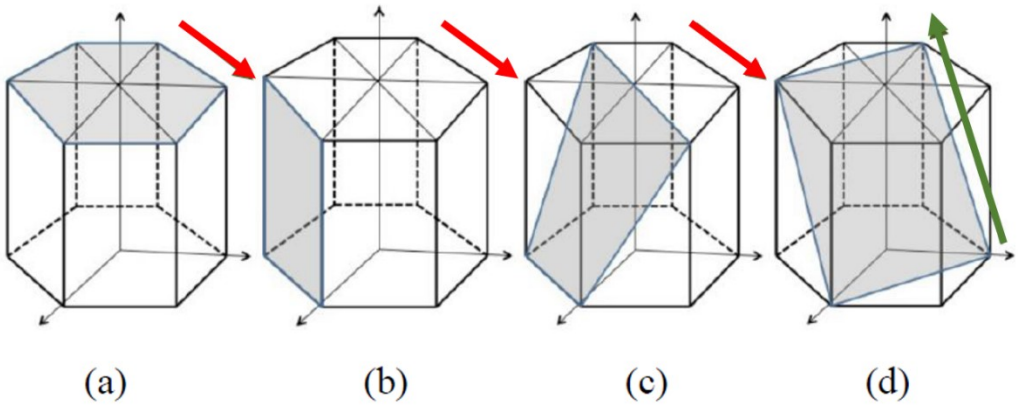

Fig. 1.3. Slip systems in Mg alloys: a) basal, b) prismatic, c) 1st order pyramidal, and d) 2nd order pyramidal. The red arrows indicate the <a> direction, the green arrow indicates the <c+a> direction [25].

In the case of Mg, with the *c*/*a* ratio very close to the ideal value, besides primary basal slip, additional prismatic and pyramidal slip can be activated [20]. Their activation strongly depends on the loading direction with respect to the slip plane and slip direction, on solute atoms and temperature.

The orientation dependence of the resolved shear stress was first characterized by Schmid [26]. For a single crystal with a cross section S_0, deformed by a force F applied parallel to the axis of the sample, the Schmid law states the CRSS (τ_{CRSS}) for the activation of a slip system as:

$$\tau_{CRSS} = \frac{F}{S_0} cos\varphi cos\lambda = \sigma cos\varphi cos\lambda, \tag{1.1.}$$

where σ is the applied stress, φ is the angle between the loading axis and the normal to the slip plane and λ is the angle between the loading axis and the glide direction, see Fig. 1.4. The Schmid factor (m) is then defined as the ratio of the shear to the applied stress:

$$m = \frac{\tau_{CRSS}}{\sigma} = cos\varphi cos\lambda. \tag{1.2.}$$

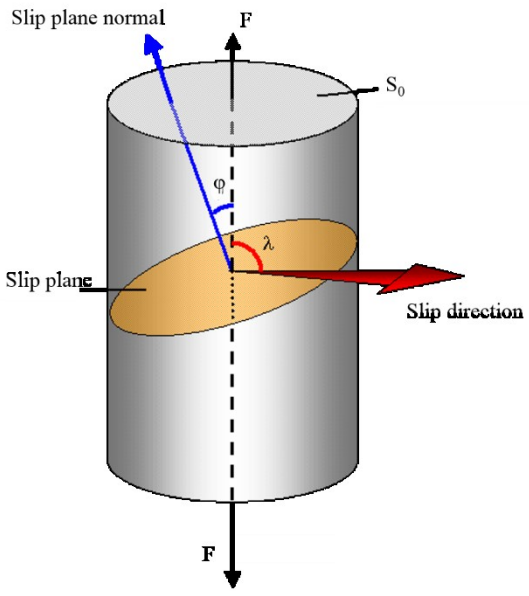

Fig. 1.4. Plastic deformation of a single crystal.

F – applied load, S_0 – cross-section, φ - the angle between the loading axis and the normal to the slip plane, λ - the angle between the loading axis and the glide direction.

The plastic deformation of a single crystal obviously starts at different applied stresses σ for the different orientation of the crystal but the shear stresses τ are the same for all orientations. Thus, the CRSS for each deformation slip system strongly depends on the orientation of the crystal [27, 28] and the Schmid factor has a moderation role. More details of the deformation of the Mg single crystal can be found in [29].

When the loading axis is perpendicular to the slip plane, the shear stress is zero and brittle fracture occurs in the crystal. When the loading axis just approaches to be perpendicular to the basal slip plane, geometric softening takes place. The tension component in the basal plane and slip direction is very small, thus high stresses are required to reach the CRSS. When the CRSS is reached, dislocation slip is activated and the slip plane is rotated into the loading direction. Hereafter, smaller stress is necessary to maintain plastic deformation and a decrease in the stress on the deformation curve is observed.

When the loading axis is nearly parallel to the basal slip plane, the Schmid factor is negligible and deformation can proceed by:

(i) twinning (see section 1.2.2.);
(ii) slip on non-basal planes, when CRSS required for the activation of the slip system is achieved.

According to von Mises [30], for the realization of homogeneous crack-free plastic deformation in polycrystalline materials, at least 5 independent slip systems are required. As it was mentioned above, in Mg alloys deformed at RT, four slip systems can be activated: basal, prismatic, 1st order and 2nd order pyramidal, listed in Table 1.1. [16, 31]. The first activated slip system in Mg and its alloys is the basal slip, which CRSS is significantly lower than that for the other slip systems, Table 1.2. [32–39]. Particularly, it was shown in [32] that the CRSS for the non-basal <a> slip is about 50-100 times higher than that for the basal <a> slip. The basal and prismatic slip together provide just 4 independent slip modes. The 1st order pyramidal slip system could be added, however, it is not independent because the combination of the basal and prismatic slip leads to the same deformation direction. Thus, all these slip systems enable deformation along the <a> direction only.

The CRSS of the slip in a <c+a> direction on the 2nd order pyramidal plane is much higher at RT than that of the <a> slip [40]. The difference can be explained by

the relatively large Burgers vector in comparison to the lattice parameters. Moreover, the activation of the <c+a> slip at RT was not observed and it was suggested that it takes place at temperatures above 200 °C. Therefore, to achieve plastic deformation along the <c> direction at RT an additional deformation mechanism, mechanical twinning, is required.

Table 1.2. CRSS values for activation of the slip systems in Mg alloys [33, 39, 41, 42]

Slip system	**CRSS [MPa]**
Basal <a>	0.52 – 1.2
Prismatic <a>	8 - 20
2^{nd} pyramidal <c+a>	40 - 100

1.2.2. Deformation twinning

In contrast to dislocation slip, the shear is evenly distributed over a three-dimensional region during deformation by twinning. During twinning, the original or parent lattice and the twinned or daughter lattice have the same structure but different orientation [43, 44]. They are separated by a twin plane, also known as twin boundary [43]. There are three types of twinning:

(i) growth twins form during crystal growth;
(ii) annealing twins form during heat treatment or recrystallization;
(iii) deformation twins form when the material is stressed.

During straining of the Mg alloys, deformation twins contribute to the work hardening, since twin boundaries, similarly to the grain boundaries, can block the free dislocation motion.

The deformation twins can be characterized by four invariants (κ_1, η_1, κ_2, η_2) shown in Fig. 1.5. The first two (κ_1, η_1) correspond to the invariant plane of shear κ_1 with a shear direction η_1, i.e. the plane of mirror symmetry or also known as the twinning plane. The second two are related to the undistorted plane, the conjugated plane κ_2 with the shear direction η_2. The shear plane S is perpendicular to both the κ_1 and κ_2 planes and contains the direction η_1. When the deformation occurs, the plane κ_2 is rotated to the plane κ'_2 which forms the same angle θ with κ_1 as that with the plane κ_2. The magnitude of the shear can be calculated as $g = 2cot\theta$ [43]. From the above

mentioned four invariants, only two of them are independent: the κ_1 and η_2 or the κ_2 and η_1. The twin and matrix are related by the reflection in plane κ_1 or by a rotation of 180° around axis η_1 [45, 46].

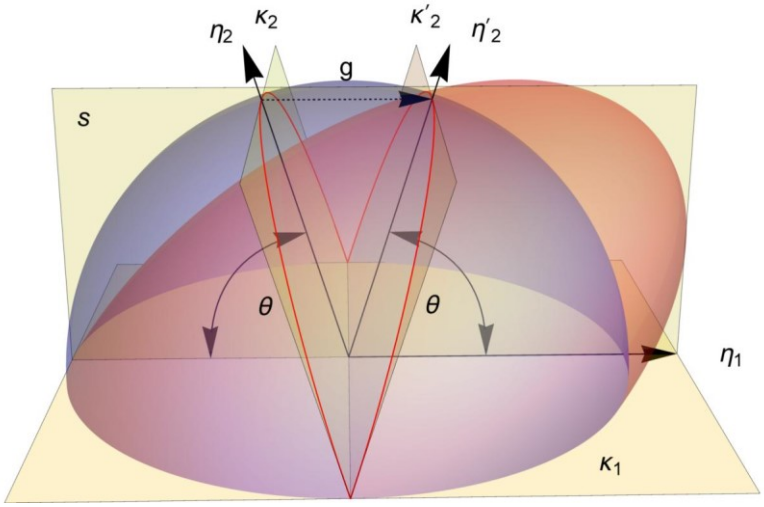

Fig. 1.5. Twinning invariants: κ_1 – twin plane, η_1 – shear direction, κ_2 – conjugate plane, η_2 – conjugate shear direction, g – magnitude of twinning and S – shear plane [47].

Contrary to dislocation slip, which magnitude is an integer multiple of the Burgers vector, during twinning, the atoms shift with different magnitudes and directions. Moreover, a sudden change in the orientation of the crystal lattice is caused by twinning while during dislocation slip, the changes in the lattice have a continuous character. Furthermore, the twinning has a strong polar nature resulting in the selective character of twins' activity in different grains during compressive or tensile loading.

The four main twinning modes reported in *hcp* metals are listed in Table 1.3. In Mg alloys, the most common twinning system is the $\{10\bar{1}2\}\langle 10\bar{1}\bar{1}\rangle$ system, frequently called as extension twins [48, 49]. It is usually activated when straining along the c-axis is needed, i.e. when tensile strain is applied parallel to the c-axis or a compression strain – perpendicular to the c-axis [49, 50]. Schematic illustration of its activation is presented in Fig. 1.6. Since the basal and prismatic <a>-slip cannot contribute to the straining along the *c*-axis and the activation of a <c+a> pyramidal slip requires high stress [51], extension twins are necessary to be activated. They reorient the crystal by 86° with respect to the original lattice [49] and by their activation a maximum strain of 6.4% can be accommodated [26].

Table 1.3. The most commonly observed twin modes in hcp metals [20]

κ_1	κ_2	η_1	η_2
$\{10\bar{1}2\}$	$\{10\bar{1}\bar{2}\}$	$\pm\langle 10\bar{1}\bar{1}\rangle$	$\pm\langle 10\bar{1}1\rangle$
$\{10\bar{1}1\}$	$\{10\bar{1}\bar{3}\}$	$\langle 10\bar{1}\bar{2}\rangle$	$\pm\langle 30\bar{3}2\rangle$
$\{11\bar{2}2\}$	$\{11\bar{2}\bar{4}\}$	$1/3\langle 11\bar{2}\bar{3}\rangle$	$1/3\langle 22\bar{4}3\rangle$
$\{11\bar{2}1\}$	(0002)	$1/3\langle\bar{1}\bar{1}26\rangle$	$1/3\langle 11\bar{2}0\rangle$

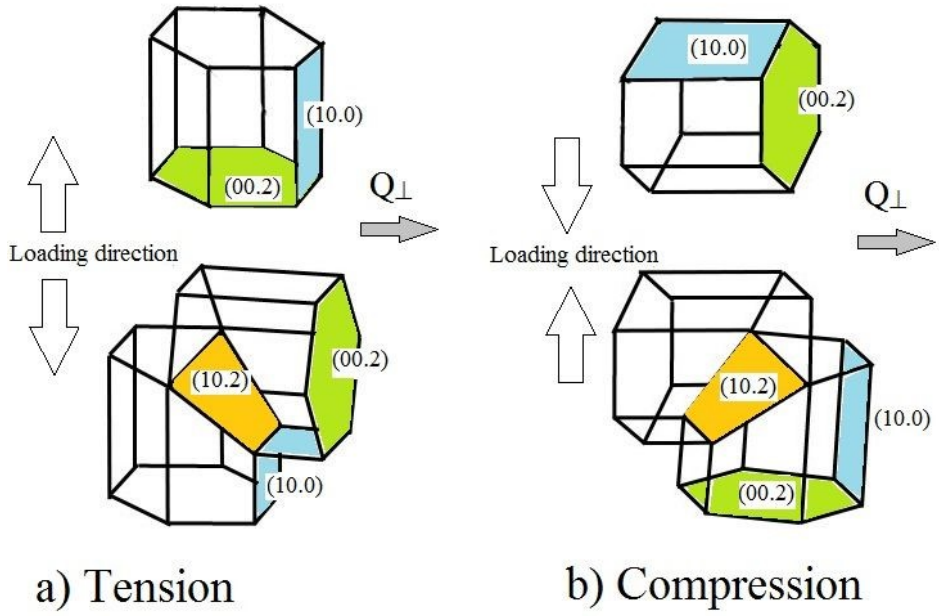

Fig. 1.6. Activation of the $\{10\bar{1}2\}\langle 10\bar{1}\bar{1}\rangle$ *twinning system in a) tension and b) compression* [18].

Twin modes which cause a contraction along the c-axis, also called compression twins, are the $\{10\bar{1}1\}\langle 10\bar{1}2\rangle$ or $\{10\bar{1}3\}\langle 30\bar{3}2\rangle$ twinning systems. They are activated when compressive strain is applied parallel to the c-axis and result in 57° reorientation of the crystal with respect to initial orientation [52, 53].

Twinning has a significant effect on the deformation behavior: the twin boundaries act as obstacles for dislocation movements, and the reorientation of the grain can help or hinder activation of additional dislocation mechanisms in the twin or in the parent grains.

The twinning process consists of three main parts: twin nucleation, twin growth or propagation, and twin thickening. The beginning of the twinning process, i.e. twin nucleation, is driven by the local stress states and the local atomic configurations at grain boundaries [54, 55]. Twin growth is realized by the motion of twin boundaries and is driven by long-range stress states across the grain. During propagation, the twin grows rapidly by gliding of twin dislocation on the twin plane along the twin direction. Contrary, twin thickening happens through the motion of twin boundaries in the normal direction to the twinning plane. The velocity of the thickening compared to that of the propagation is by several orders lower [56].

The stress state associated with twin nucleation and propagation was studied by deformation of single crystals or specially oriented polycrystals with a strong texture [33, 42]. It was found that the stress required for extension twinning is between the CRSS of the basal and prismatic slip. However, its activation is strongly dependent on the grain size [57, 58]. It was shown by Dobroň et al. [58] that twins first nucleate in bigger grains and with ongoing plastic deformation they are activated in the smaller ones. Detailed analysis of the correlation between grain size, grain orientation, and grain boundary misorientation and the nucleation and growth of $\{10\bar{1}2\}\langle 10\bar{1}\bar{1}\rangle$ deformation twins in Mg alloys by electron backscatter diffraction (EBSD) mapping was done by Beyerlein et al. [59]. They observed that not always the twin type with the highest Schmid factor is activated. Jonas et al. [60] have shown that the twin variant selection strongly depends on the accommodation of the deformation which requires prismatic glide in the neighboring grains. This statement was confirmed both experimentally [61] and theoretically [62].

1.3. The long-period stacking ordered (LPSO) phase

The long-period stacking ordered (LPSO) phase is a long-range stacking of basal planes with periodic enrichment of transition metals (Zn, Cu, Ni) and rare earth (RE) elements (Y, Nd, Gd) [10, 63, 64]. Depending on the ratio of the transition metals and RE elements, besides the LPSO phase, other types of phases can be formed in the Mg alloys: W-phase is formed when the ratio of Zn:RE is 3:2, quasicrystalic I-phase at Zn:RE of 6:1 an LPSO or X-phase at the ratio between 1:1 and 2:1 [65].

1.3.1. Formation and types of the LPSO phase

The LPSO phase is formed by diffusional transformation. Nishida et al. [66] showed that in the Mg-Y-Zn alloys, the LPSO phase nucleates at grain boundaries, where Zn and Y are segregated during the solidification of the material, and then it grows to the grain interior along the basal plane. The LPSO phase is not only stacking ordered but also chemically ordered structure [10], and therefore it seems that the stacking sequence is sensitive to the concentration of Zn and Y in the Mg matrix [67].

Kawamura et al. introduced in their paper [68] the criteria for a contribution of the RE element in the formation of the LPSO phase. They found the following requirements for the RE element:

(i) negative mixing enthalpy for Mg-RE and Zn-RE pairs;
(ii) *hcp* structure at RT;
(iii) solid solubility above ≈ 3.75 at.% in Mg;
(iv) atomic size larger than Mg by 8.4 to 11.9 %.

Based on their systematic study of alloying elements, they found that the LPSO phase is formed in $Mg_{97}Zn_1RE_2$ alloys with RE = Y, Gd, Dy, Ho, Er, Tb and Tm. Moreover, depending on which part of the processing the LPSO phase is formed, the alloys were separated into two groups. The first group (Type I.) contains Y, Dy, Er, Ho and Tm, and the LPSO phase is formed during solidification (the LPSO phase is already present in the cast alloys). The Mg-Zn-Gd and Mg-Zn-Tb alloys belong to the second group (Type II.), in which the LPSO precipitates with soaking (at 501 °C (775 K) for 10 hours) [68].

Using high precision high-angle annular dark-field imaging in scanning transmission electron microscopy (HAADF-STEM) it was discovered that polytypic structures with a different number of Mg layers exist. Up to now, four polytypes of the stacking sequences of the LPSO structures, schematically illustrated in Fig. 1.7., have been reported in Mg-Y-Zn alloys [67, 69]. In the early studies, a 6H structure with a monoclinic lattice (a = 0.56 nm, b = 0.32 nm, c = 1.56 nm and β = 88°) was reported [10, 70–72]. However, it was found that this structure was not fully correct and it was replaced by the 18R LPSO structure in the later studies [11, 67, 73, 74]. The unit cell of the 18R structure was suggested to be hexagonal (a = 0.321 nm, c= 4.86 nm) and with an ABCBCBCABABABCACACA stacking sequence of the closely packed

planes [11, 67, 73]. However, later it was shown that the unit cell of the 18R structure is made up of three building blocks, each having an ACBA-type stacking sequence of the closely packed planes, i.e. an AB**ABCA**CA**CABC**BC**BCAB**A stacking sequence. The bold characters represent the four-layer building blocks of the 18R structure. The three building blocks are arranged in the same shear direction respect to the Mg matrix. Therefore, a significant shear strain is generated in the Mg matrix during the formation of the 18R-type LPSO structure [64].

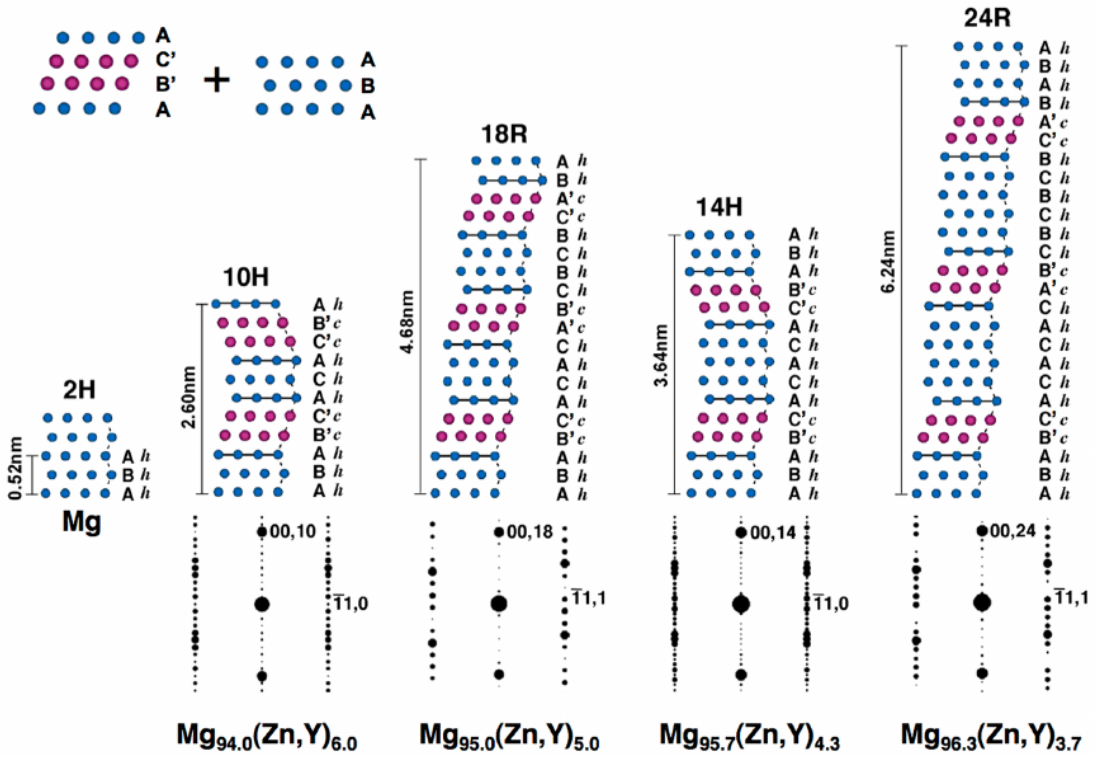

Fig. 1.7. Structure models of the Mg-Y-Zn LPSO polytype structures. The blue circles represent the Mg and the red circles the Zn/Y occupation site. [69].

The second most frequently observed LPSO structure in the Mg-Y-Zn alloys is the 14H structure, which gradually replaces the 18R structure during heat treatments in a temperature range of 350 - 500 °C [11, 63, 67, 74, 75]. The 14H structure has also a hexagonal unit cell with lattice parameters of $a = 1.11$ nm and $c = 3.65$ nm. It contains two twin-related building blocks with an ABCA-type stacking sequence of its closely packed planes: AB**ABCA**CAC**ACBA**BA. The twin-related building blocks have opposite shear and they generate zero shear relative to the Mg matrix [63].

1.3.2. Deformation behavior of the LPSO phase

The 18R type structure is the most commonly identified LPSO phase in the Mg-Y-Zn alloys [67, 73, 76] and its volume percent increase with the increasing content of Zn and Y [77]. Therefore, to study the deformation mechanisms of the LPSO phase, the $Mg_{85}Zn_6Y_9$ alloy with a volume fraction of the LPSO phase over 85% [5, 78–82] – or 18R type LPSO micro-pillars were used [83–85].

For example, Hagihara et al. [5] examined the compressive behavior of directionally solidified (DS) $Mg_{85}Zn_6Y_9$ alloy. It was shown that during the solidification a strong texture with the (0001) basal planes oriented parallel to the growth direction is formed. The DS alloy was deformed along the growth direction, i.e. parallel to the basal planes, and along the direction tilted by 45° from the growth direction in a wide temperature range from -196 to 400 °C. In the sample deformed along the direction tilted by 45° from the growth direction (i.e. from the basal planes), the Schmid factor of the basal slip is very high. Therefore, the basal slip dominated the deformation at all temperatures. No other slip traces were observed in this condition. Based on the strain rate sensitivity it was also confirmed that at RT and 200 °C the deformation is controlled by the mechanism accompanied by the large activation volume, similar to that in pure Mg and its solid solutions [37]. The CRSS for the $(0002)\langle 11\bar{2}0\rangle$ slip in the LPSO phase was evaluated as 10 to 30 MPa at RT, what is much higher than that for the pure Mg [37] (about 1 MPa), but not much higher than that of Mg-1 at.% Y solid solution [86]. Since the atomic arrangement of the basal plane of the 18R phase and that of the Mg phase is the same, it is not surprising that the controlling mechanism for the deformation by the basal slip in the LPSO phase is analogous to that in Mg [5, 37]. It was also shown in Ni-based LPSO crystals, that the CRSS of the basal slip at low temperature is irrespective of the stacking sequences [87–89].

When the alloy was compressed along the growth direction, i.e. parallel to the basal planes, the operation of the basal slip was significantly limited due to its small Schmid factor [5]. In this case, band-like structures were formed. As already mentioned, in materials with hexagonal structures, the operative deformation mode strongly depends on the *c/a* ratio. The formation of the $\{10\bar{1}2\}$ deformation twins in metals with *c*/*a* higher than 1.73 (the case of e.g. Zn, Cd, and the LPSO phase) is

suppressed. In these materials, when compressive loading along the $\langle 11\bar{2}0 \rangle$ is applied, the deformation kinks are formed [90–92]. The first model explaining the formation of the deformation kinks in *hcp* crystals was suggested by Hess and Barrett for Zn single crystal [91]. The deformation kinks were formed by an increasing rotation of the lattice due to the avalanche generation of pairs of dislocations on the basal plane [91, 93], as shown on the scheme in Fig. 1.8. Although, the activation of <c+a> dislocations would be the other possible deformation mode for accommodating the strain in this loading condition. However, they were hardly observed in the LPSO phase [5, 85]. It was proposed by Hagihara et al. [5] that the complicated atomic arrangement on the non-basal planes of the LPSO phase can prevent the activation of the <c+a> dislocations.

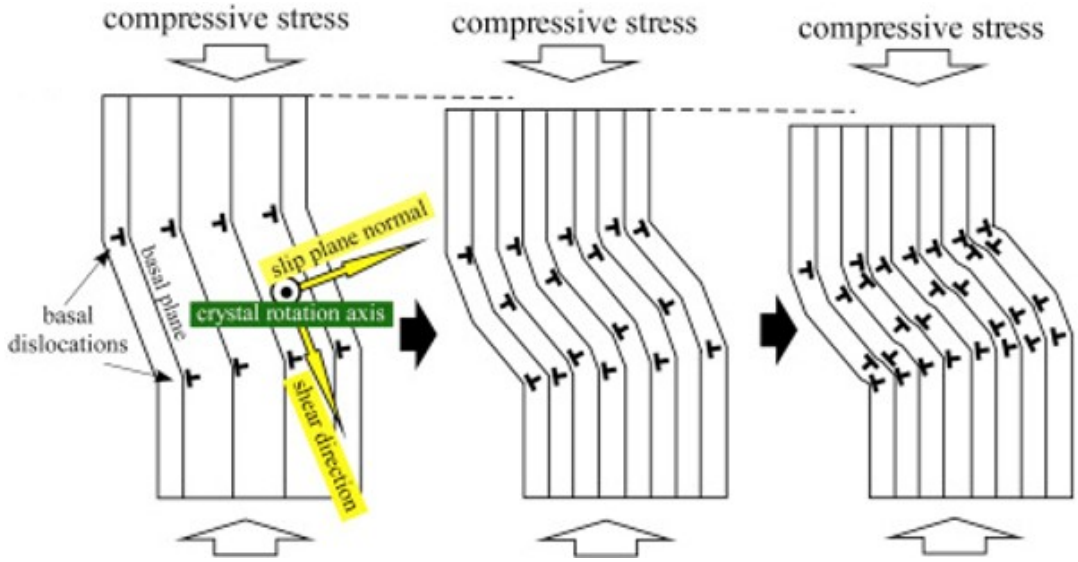

Fig. 1.8. Schematic illustration showing the formation of the deformation kink bands [94].

Hagihara et al. [78] studied *in-situ* the characteristic features of the deformation kinks formed in the Zn single crystal and in the LPSO phase. In the Zn single crystal, the operation of the $\{11\bar{2}2\}$ pyramidal slip generated slight crystal rotation and therefore, the operation of the basal slip was locally induced. During the ongoing deformation, deformation kink band boundary appeared with traces of basal slip. The increase of the rotation angle of the kink bands enabled the operation of the basal slip due to the increased Schmid factor for the basal slip. The traces of the basal slip were

largely bent what indicates the occurrence of large crystal rotations. The average migration speed of the kink band boundary was evaluated to be ≈ 1.6 μm/s along the direction perpendicular to the kink boundary. Similar to the Zn single crystal, in the LPSO phase around the kink bands, traces of basal slip were observed. Moreover, it was shown in [78] that if the misorientation around the *c*-axis of the LPSO phase is larger than 20-30° then the propagation of the deformation kink band beyond the grain boundary is strictly prohibited. However, if the misorientation around the *c*-axis is under 20-30°, the misorientation around the *a*-axis does not affect its propagation behavior. This behavior was related to the high randomness of the deformation kink band in which the crystal rotation axis varied on the ⟨0001⟩ zone axis due to the change of the kind of the basal dislocations that construct the deformation kink band boundary [95, 96]. In the LPSO phase, two types of kink formations were observed [78]. The first type nucleated very quickly and once their formation was completed their growth rarely proceeded again, whereas the second type nucleated much slower. Recently Matsumoto et al. [81, 97], based on computer analysis using atomistic simulation, suggested the possibility of the existence of different formation mechanisms of the deformation kink bands. One of the suggested mechanisms was the role of the local operation of pyramidal dislocation in the formation of basal dislocation pairs, which lead to the development of kink bands. In this case, the motion of "one" pyramidal dislocation governs the kink band formation. Thus, the formation speed is much higher than that of the kink formed by the so-called "Hess-Barnett mechanism" [91]. Hagihara et al. [78] showed that the migration speed of the „faster-type" deformation kink band is more than 10^5 times higher than that of the „slower-type" formation, although no significant differences in their appearance were observed.

Similar to that, during twinning, the kinked regions shows a distinct crystal orientation relationship with respect to the matrix [98–100]. Crocker et al. [101] tried to classify the kink bands observed in *hcp,* face-centered cubic *(fcc*) and body-centered cubic (*bcc*) materials using the conventional notation for twinning. However, unlike the case of twinning the shear during kinking is not restricted to a particular value, thus the interface of the kink continuously reorients in order to maintain its symmetrical character [96]. According to Yamasaki et al. [96], kinking rather occurs by progressive rotation of the lattice within a band than by sudden shear of the final orientation, as during deformation twinning. Therefore, they suggested a classification defined by the

Taylor axis of the kink band and concluded that all kink bands can be categorized into two types. The first type occurs through basal <a> slip with $\langle 1\bar{1}00\rangle$ and $\langle 0\bar{1}10\rangle$ Taylor axes, the second type around the $\langle 0001\rangle$ axis suggest that lattice rotation occurs through the prismatic <a> slip.

1.4. Strengthening mechanisms in metallic materials

Macroscopic plastic deformation is caused by the movement of a large number of dislocations. However, to increase the strength of the material, obstacles need to be introduced in the material in order to hinder the dislocation motion [102]. The basic strengthening mechanisms in metals are the grain boundary strengthening, solid solution strengthening, dispersion or precipitation strengthening and deformation strengthening (also called as work or strain hardening).

1.4.1. Grain boundary strengthening

Dislocations cannot overcome grain boundaries since the dislocations Burgers vector has to be a translation vector of the crystal, which is not fulfilled for the next neighbor grain, except for very special cases, due to its different orientation. Hence, in the neighboring grain, the slip directions are different and usually not parallel to each other. Therefore, the dislocations pile up at the grain boundaries and exert back stress, opposite to the applied shear stress, on subsequent dislocations.

The principle “the finer grains the harder metal” was known for a long time, but the first relation between the grain size and the mechanical properties of polycrystalline alloys was suggested by Hall and Petch [103, 104]:

$$\sigma_{0.2} = \sigma_0 + k\frac{1}{\sqrt{d}}, \tag{1.3}$$

where $\sigma_{0.2}$ is the yield stress, σ_0 is the friction stress, k is a material constant, and d is the grain size. The friction stress includes contributions from solutes and particles but not from dislocations, thus it is the flow stress of the undeformed single crystal oriented for multiple slip.

The Hall-Petch relation is one of the most important relations in physical metallurgy, mainly for materials in which the chemical composition cannot be changed, and therefore their strengthening is obtained by grain refinement. However, it is applicable only in a limited range of grain sizes: approximately from 20 nm to tens

of μm. In nanocrystalline materials with grain sizes around 10 to 30 nm, the strength does not change or even decreases with decreasing grain size [105]. This is known as inverse Hall-Petch behavior [106].

In the case when the value of the yield stress ($\sigma_{0.2}$) is higher than the contribution of the grain boundary strengthening ($\frac{k}{\sqrt{d}}$), further strengthening mechanisms must be involved.

1.4.2. Solid solution strengthening

The alloying elements, depending on their atom sizes, could form interstitial or substitutional point defects in the material. These point defects do not affect the crystal structure of the solid solution, only local stress fields are formed. The solid solution strengthening is caused by the interaction of the alloying elements with the dislocations which result in an increased glide resistance [107]. It was already shown that larger atoms can generate higher strengthening than the smaller ones, however, their low solubility limits the potential strengthening effect.

1.4.3. Dispersion or precipitation strengthening

The particles of different phases in the matrix serve as obstacles for dislocation motion. Therefore, their presence leads to precipitation strengthening (or hardening) [108]. Three types of particles can be present in the material: coherent, semi-coherent, and incoherent.

Dispersion hardening occurs when the dislocation cannot cut or penetrate an incoherent particle. In this case, the dislocation has to circumvent the particle, which leads to the creation of a dislocation loop. This process was described by Orowan and it is known as the Orowan mechanism [107, 109].

Precipitation hardening is caused by phases with coherent or semi-coherent phase boundaries. In this case, dislocations can move through the particles since all crystallographic planes and directions of the matrix continue into the precipitate with only slight distortion. Although the precipitate will utilize forces on dislocation, if the dislocation overcomes these forces it may cut the particles resulting in particle shear off. This mechanism is known as Friedel mechanism [107].

1.4.4. Deformation strengthening

Not only the grain boundaries and precipitates but also the immobile dislocations can influence the hardening process of alloys. Deformation (or dislocation) strengthening is caused by interacting dislocations which form stress fields in the lattice. The correlation between the dislocation density and yield stress can be expressed as:

$$\Delta\sigma_{0.2} = M\alpha Gb\sqrt{\rho_D}, \tag{1.4}$$

where $\Delta\sigma_{0.2}$ is the contribution of the dislocation strengthening to the yield stress, M is the Taylor factor, α is a constant (with values between 0.1 - 0.5), G is the shear modulus, b is the Burgers vector and ρ_D is the dislocation density.

1.5. Extrusion

Extrusion is one of the most common thermomechanical processes for manufacturing semi-finished or final products. During forward or direct extrusion, the material flows in the direction of the extruder, while during backward or indirect extrusion, the material flows against the working direction of the extruder, see Fig. 1.9. During the process, only compression and shear stresses are induced into the material, thus brittle materials could be processed by this method as well. The characteristics of the final product depend on process parameters such as temperature, the extrusion rate and the extrusion ratio (ER). The ER is defined as the ratio between the initial cross-section (S_1) and the final cross-section (S_2) of the extruded billet:

$$ER = \frac{S_1}{S_2}. \tag{1.5}$$

Depending on the extrusion temperature, the extrusion can be (i) cold – extruded at RT, (ii) warm – extruded at temperatures between RT and under the recrystallization temperature, and (iii) hot – extruded above recrystallization temperature where cold working no longer occurs. Mg alloys are usually extruded between 300 - 450 °C due to their low plasticity at RT.

The extrusion rate significantly depends on the extrusion temperature: higher temperatures allow higher extrusion rates [110, 111]. However, it needs to be determined experimentally and optimized for each alloy separately.

In extruded Mg alloys the final grain size is in a range of microns, but grains elongated along the extrusion direction (ED) often remain in the microstructure [112]. During the process, the grains are fragmented, extended parallel to the ED and reoriented with basal planes parallel to the ED [58, 112–116].

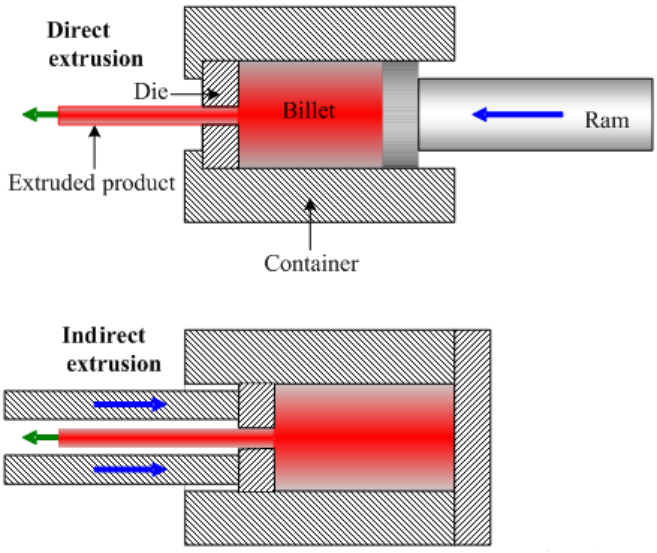

Fig. 1.9. The typical configuration of the direct and indirect extrusion process [117].

1.6. In-situ methods

1.6.1. Synchrotron diffraction

X-ray diffraction is a powerful technique that uses the interaction of the incident beam with the sample to study the structural and microstructural properties of materials. X-rays generated by a synchrotron facility are at least five orders of magnitude more intense than the best laboratory X-ray sources.

The synchrotron radiation is notable for its high level of polarization and high collimation (small angular divergence of the beam). The quality of an X-ray source is defined by its brilliance [118], which takes into account:

(i) number of photons produced per second;
(ii) the angular divergence of the photons;
(iii) the beam's cross-section
(iv) the photons falling within a bandwidth of 0.1% of the central wavelength of frequency.

The main advantage of X-rays is the easier availability compared to the neutron sources. Moreover, the intensity and the effective cross-section of the X-rays is higher than that of the neutrons with the most powerful sources. These facts lead to lower acquisition time during synchrotron diffraction measurements compared to neutron diffraction tests. However, there are some disadvantages. First, the scattering power of an atom decays with the scattering angle for X-rays but not for the neutrons. Second, the penetration depth of the thermal neutrons is much higher, compared to X-rays. Moreover, the neutrons can distinguish between the isotopes and are able to detect light atoms.

The basic principle of the X-ray diffraction can be interpreted as a reflection of the incident X-ray beam from periodically spaced lattice planes, fulfilling the Bragg´s law:

$$\lambda = 2d_{hkl}sin\theta_{hkl}, \tag{1.10}$$

where λ is the wavelength of the X-rays, d_{hkl} is the distance between neighbor atomic planes (lattice spacing) with *h, k, l* Miller indexes, and θ_{hkl} is the Bragg angle between the incident beam and the atomic plane on which the beam is diffracted. The schematic draw of diffraction is shown in Fig. 1.10. Diffraction provides information from the planes which are perpendicular to the diffraction vector since it is defined as the difference between the initial wave vector $\overrightarrow{k_0}$ and diffracted vector $\vec{k}$ as:

$$q = \overrightarrow{k_0} - \vec{k}. \tag{1.11.}$$

If the incident beam is monochromatic, according to the Bragg´s law, the d-spacing can be calculated from the position of the diffraction peaks. The changes in d_{hkl} cause a shift of the diffraction peak in the diffractogram. The lattice (elastic) strains ε_{hkl} can be calculated by the shift in the position of the diffraction peak, as:

$$\varepsilon_{hkl} = \frac{d_{hkl} - d_{0,hkl}}{d_{0,hkl}}, \tag{1.12}$$

where d_{hkl} and $d_{0,hkl}$ are the planar spacings of the *hkl* plane in deformed and stress-free (initial) crystal, respectively. To determinate the $d_{0,hkl}$ is generally problematic because in polycrystalline materials is hard to reach an ideal, stress-free state, since each grain is exposed to stresses from neighboring grains. Therefore, residual stress is always present in polycrystalline materials.

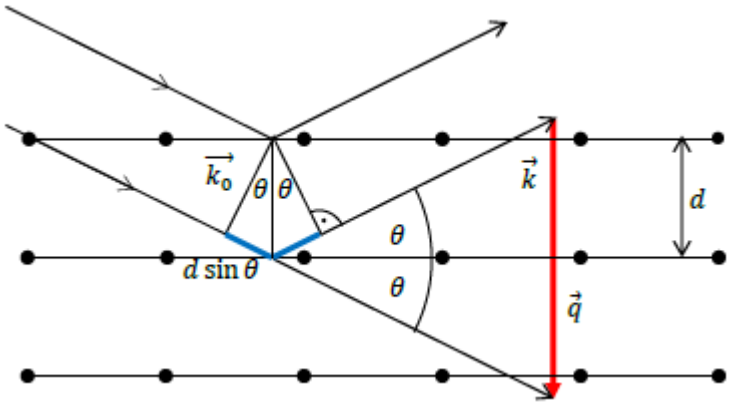

Fig. 1.10. Bragg diffraction on planes with lattice spacing equal to d [119].

The development of the lattice strains is very useful to study plastic deformation. In the elastic regime, the lattice strain evolution follows the Hooks law, i.e. it is a linear function of the applied stress. The plastic deformation begins when the lattice strain starts to deviate from the linear elastic response.

The influence of the compressive deformation on the diffraction pattern obtained by synchrotron diffraction is presented in Fig. 1.11.

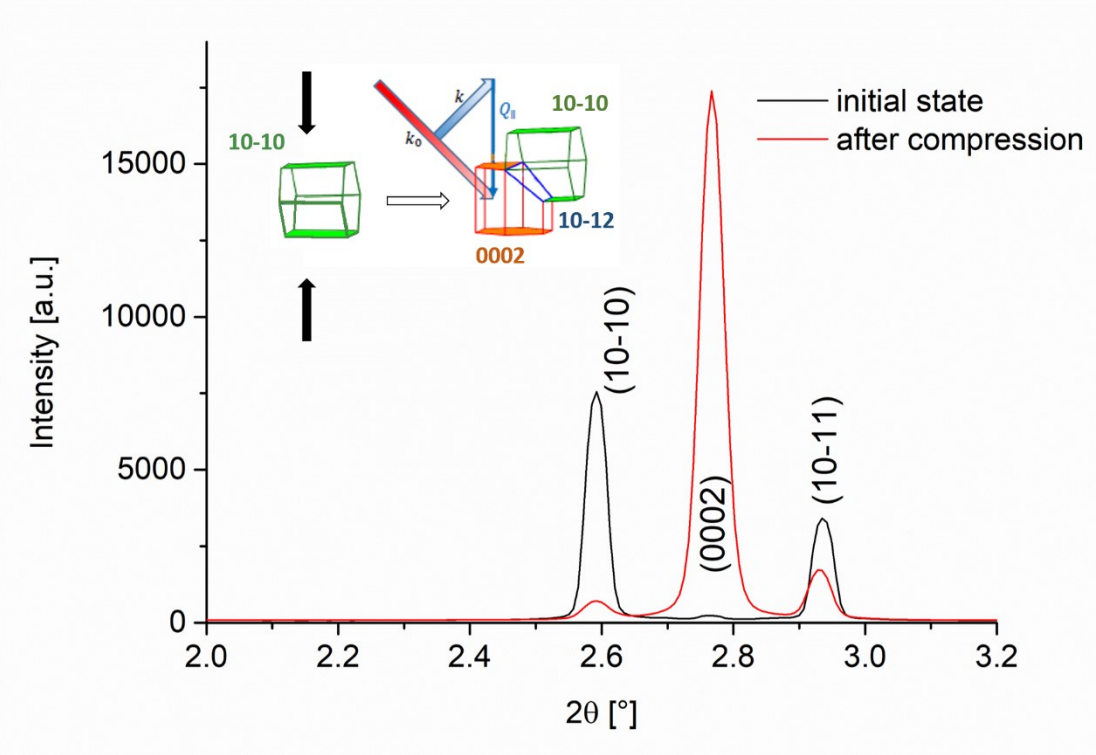

Fig. 1.11. Evolution of the diffraction pattern during twinning in compression

In the initial state (before deformation), the $\{10\bar{1}0\}$ prismatic planes are oriented perpendicular to the compression direction and the diffraction vector, and therefore the diffraction peak has a rather high intensity. The change of the intensities during deformation is influenced by the texture evolution due to the activation of the $\{10\bar{1}2\}\langle 10\overline{11}\rangle$ extension twinning. This causes a reorientation of the part of the grain and leads to the decrease of the $\{10\bar{1}0\}$ peak intensity. At the same time, the intensity of the (0002) diffraction peak increases due to the reorientation of 86° cause by extension twinning.

1.6.2. Acoustic emission (AE)

1.6.2.1. Definition and basic principles of AE

Acoustic emission (AE) is defined as transient elastic waves, which are generated by the rapid release of energy due to local dynamic changes in the material [120, 121]. AE is also a passive non-destructive method, which gives real-time (*in-situ*) and integral information from the entire volume of the material.

The local process which produces detectable AE signals (e.g. dislocation motion, twin nucleation, phase transformation, cracking, etc.) is called the source of AE. The elastic waves are propagated from the AE source through the material until they reach the surface of the sample. The wave's component which is perpendicular to the surface is detected by a piezoelectric sensor and it is transformed into an electrical signal. Therefore, the output of the detector is called the AE signal.

The AE equipment typically consists of the sensor, preamplifier, amplifier, A/D converter, signal analyzer and a computer. The standard arrangement for AE measurements is schematically shown in Fig. 1.12. Generally, two types of piezoelectric AE detectors can be used. The resonance type sensor is the most sensitive around the resonant frequency, while the broadband sensor has a flat response in a wide frequency range, although it is less sensitive compared to the resonant type. The typical working frequency of the AE sensors is between 50 kHz and 1 MHz. The sensitivity of the sensor is defined in a logarithmic scale as:

$$dB_{AE} = 20log\left(\frac{U}{U_r}\right), \tag{1.6}$$

where U_r is the reference voltage and it equals to 1μV.

The preamplifier is one of the most important items for the AE signal detection because it is used to keep a high ratio between the detected signal and the background noise. To avoid the deterioration of the measured signal it must be placed near to the sensor. The low-frequency noises of various natures (friction, vibration from the machine, etc.) are filtered from the AE signal.

The A/D converter transforms the analog to the digital signal. Thanks to the sampling frequency, which is usually in a range of 1-10 MHz, high time resolution can be achieved.

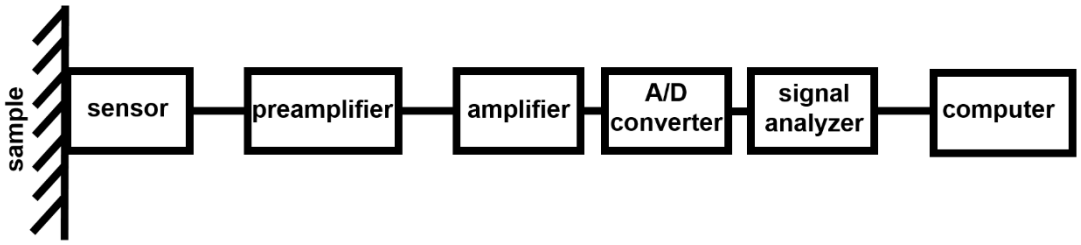

Fig. 1.12. Scheme of the detection of the AE signal [25].

The acquired AE signal can be parametrized, see Fig. 1.13. The AE parameters could be used for the explanation of the deformation mechanism. The basic parameters of AE are:

(i) AE count – the number of times the signal crosses the threshold level;
(ii) AE count rate – the count number per time unit;
(iii) AE event – part of the AE signal, which starts when the signal crosses the defined threshold level and ends when the signal remains below the threshold voltage for a period exceeding the hit definition time (HDT, also known as “dead time”);
(iv) AE amplitude – is the maximum voltage measured during an AE event.

Depending on the AE source, burst or continuous type of AE can be detected, as depicted in Fig. 1.14. Continuous emission is produced when the elastic waves are simultaneously generated by a large number of sources with low energy, and the signal does not fall below a certain threshold level after a short duration. Contrary, the burst emission has the characteristics of individual pulses, so they are well separated in time and they are avalanche-like generated. The magnitude of the released energy of the burst signal is usually by 10 to 15 orders higher than that for the continuous emission

– see the different scale of the amplitude in Fig. 1.14. [122]. During mechanical loading of Mg alloys, the AE response of the material usually consists of the mixture of continuous and bust emission, produced by dislocation movement and twin nucleation, respectively [120, 121]. Twin nucleation is accompanied by large, burst-type AE [120]. At the same time, the twin growth (i.e. increment in thickness) and twin shrinkage (i.e. reduction of thickness) do not cause detectable AE signal due to the slow motion of twin boundary emitting only low energy wave [123]. Fig. 1.15. schematically illustrates the different stages of the twinning process and whether they are accompanied by detectable AE signal.

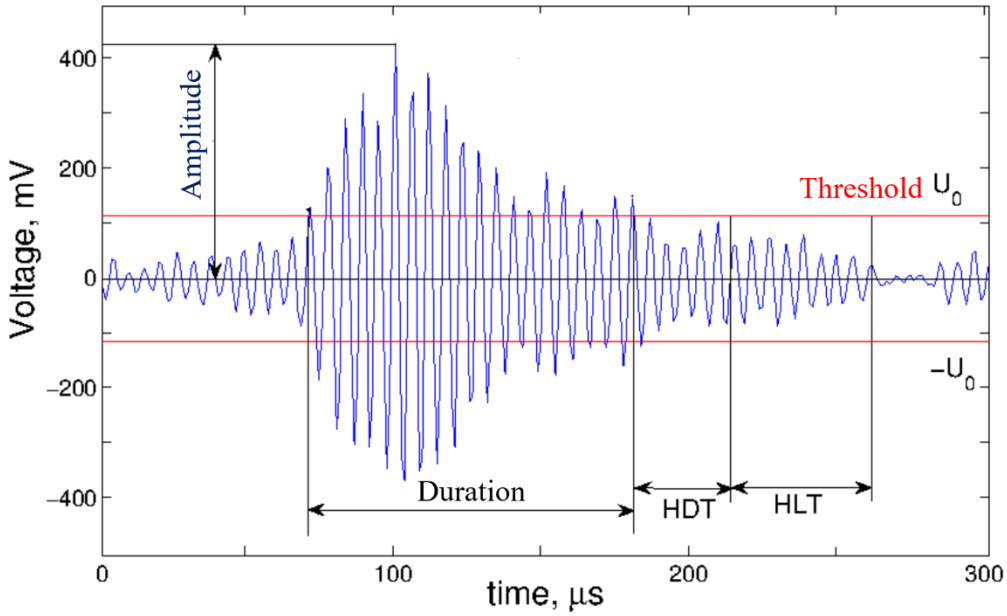

Fig. 1.13. Parametrization of the AE signal [124].

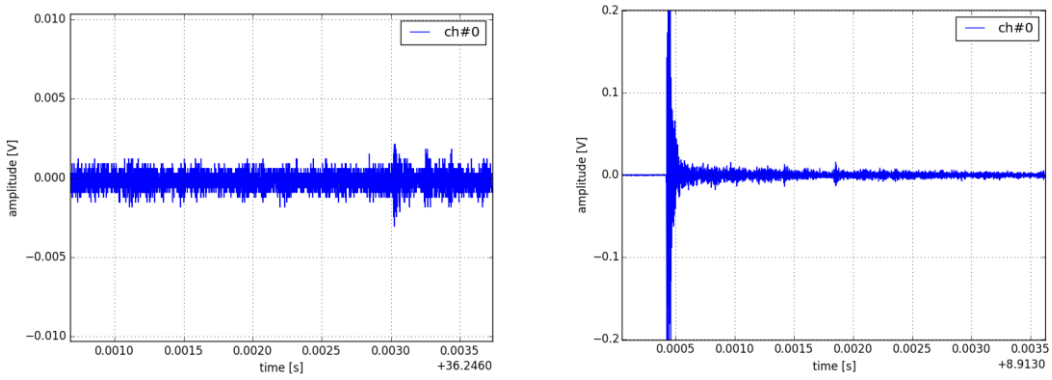

Fig. 1.14. Continuous (left) and burst (right) AE signal.

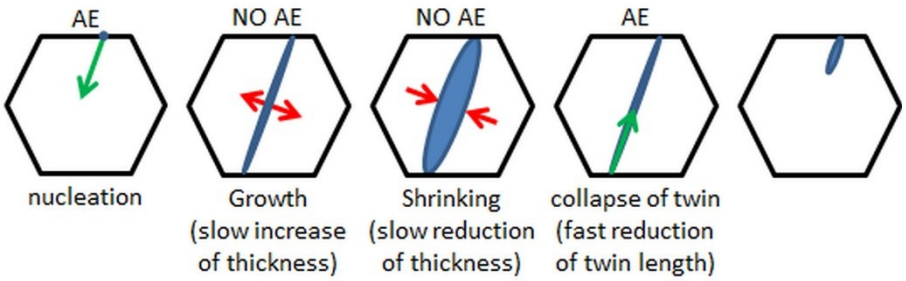

Fig. 1.15. Schematics of different stages of the twinning-detwinning process. Arrows indicate the direction of twin propagation: green color represents processes accompanied by detectable AE; red color corresponds to the processes which do not produce detectable AE [125].

1.6.2.2. Statistical analysis of the AE signal

The raw AE signal recorded during the deformation tests can be analyzed using an adaptive sequential k-means (ASK) procedure. This so-called clustering method was developed by Pomponi and Vinogradov [19]. The waveform streaming data are sectioned into consecutive time frames with a length in the order of ms. Afterward, the power spectral density (PSD) function $G(\omega)$ is calculated for each frame by Fast Fourier Transformation and using the Welch´s method [126]:

$$G(\omega) = \sum_{t=t_0}^{t_1} f_t e^{-2\pi i t\omega}, \tag{1.7}$$

where t_0 and t_1 are the time boundaries for the selected frame, f_t is the sampling frequency and ω is a frequency in a range from 0 to $\frac{f}{2}$.

The first cluster is defined according to the features of the PSD function of the first time frame. Afterward, the calculated PSD functions are analyzed one-by-one. If the statistical properties of the given PSD function are similar to that of the first cluster, this PSD function is assigned to this cluster. If not, a new cluster is established. The conditions for forming a new cluster are based on the k-means method [19]. The main advantage of the ASK clustering method is that it is not necessary to define the expected number of clusters, in other words, the number of active deformation mechanisms, in advance. Moreover, the process is non-iterative, i.e. the AE signals frames are associated with a certain cluster based on their arrival time.

Finally, the output of the ASK analysis is a set of statistically well-separated clusters. Further, particular AE source mechanisms need to be assigned to the clusters. The characteristics of the AE signal strongly depend on the sample shape, characteristics of the sensor, material, etc., and therefore, there is no general rule for this procedure. However, there are several hints on how to do the assignment:

1. Checking the time appearance of the events in a given cluster. Since AE data recording is always launched before the start of the deformation, the events in Cluster 1 naturally belong to the background noise.
2. Checking the characteristic features of the PSDs, as energy, frequency distribution, etc. The AE energy E and median frequency f_m are derived as follows:

$$E = \int_{\omega_{min}}^{\omega_{max}} G(\omega) d\omega \tag{1.8}$$

$$\int_0^{\omega_m} G(\omega) d\omega = \int_{\omega_m}^{\infty} G(\omega) d\omega \tag{1.9}$$

   Generally, the twin formation usually emits an AE signal with larger energy than that of dislocation slip [121, 127].

3. Verification of the results of the cluster analysis by other experimental methods, as texture measurements, microscopy or theoretical modeling.

The ASK analysis provides information about the dynamics of the system with a time resolution of μs. It is important to note that this method defines the dominant deformation mechanism, but it does not mean that other mechanisms are not active, they simply produce a less loud signal.

1.6.3. Application of in-situ methods

Some studies have shown the similarity of the plastic deformation between single crystals and polycrystals with a strong texture [42, 128]. However, these papers were dealing with the macroscopic response of the material and the evolution of the microstructure was not explored in detail. Nowadays, the combination of the deformation tests with *in-situ* methods and modeling is successfully used for a study of the slip systems in materials with a strong texture [129, 130]. The important role of non-basal <a> slip was confirmed, but there is no general agreement between the scientific groups on the type of the slip systems. According to Agnew et al. [130], the prismatic <a> slip is the dominant non-basal <a> slip, while Muránsky et al. [131]

suggested the activation of the pyramidal <a> slip or the cross slip between basal and prismatic plane.

The only possible direct method to study the dislocation structures is using transmission electron microscopy (TEM). Some authors [132, 133] studied the structure of the <c+a> dislocations by TEM and contrary to the single crystal measurements, they were observed already at RT. However, these results have very small statistical significance because only a small volume of the sample can be investigated. Moreover, there is a problem with the stability of the <c+a> dislocations: they tend to reduce their energy by dissociation [133]. At the same time, an indirect method to investigate the dislocation structure of the whole material by evaluation of the dislocation density from the X-ray diffraction pattern was developed by Ungár et al. [134, 135]. Máthis et al. [136] successfully used this method to reveal the temperature dependence of the activation of the <c+a> dislocation. It was shown that their fraction increases with increasing deformation temperature.

Recently Vinogradov et al. [56] successfully examined the nucleation and propagation of twins by the AE technique and high-speed video imaging. They have shown a direct correlation between the amplitude of the AE signal and the length of the nucleated twin. However, AE is still not able to detect twin growth due to its too slow motion [137].

The combination of the AE and neutron or synchrotron diffraction methods (see section 3.4.) have been successfully used to study twinning in the entire gauge volume [137, 138]. AE is sensitive to twin nucleation while the diffraction methods provide information about the overall twinned volume. Therefore, a complementary dataset helps to monitor the twinning activity in the deformed material.

2. Aims of the thesis

The main goal of this work is to reveal the active deformation mechanisms in novel high strength Mg alloys using advanced *in-situ* techniques. For this purpose, two alloys with different content of the LPSO phase were subjected to study by acoustic emission and synchrotron diffraction. The obtained results were supported by *in-situ* and *post-mortem* microstructure observation by SEM and TEM. The presence of the LPSO phase has a key importance, as it affects the deformation behavior of the Mg-LPSO alloys and brings the desired strengthening for the Mg alloys.

The present thesis particularly focuses on the following tasks:

- Characterize the initial microstructure (including volume fraction and identifying the LPSO phase) and texture of the extruded materials with respect to the alloying content.
- Reveal the deformation behavior of the extruded bars in compression and tension by *in-situ* acoustic emission and *post-mortem* SEM. Analyze the tension-compression yield asymmetry with respect to the presence of the LPSO phase. Clarify the role of the amount of the LPSO phase as well as the twinning in α-Mg during the room temperature deformation.
- To examine the compression behavior by *in-situ* synchrotron diffraction and *post-mortem* SEM in a temperature range between RT and 350 °C. Explain the role of the LPSO phase, dynamic recrystallization and kinking during compressive loading at elevated temperatures.

3. Experimental materials and methods

3.1. Experimental material

To study the effect of the amount of the LPSO phase on the microstructure and mechanical properties, two wrought Mg-Zn-Y magnesium alloys with a different amount of alloying elements were chosen. Both Mg alloys with an addition of 0.5 wt.% of CaO[1] were cast in KITECH (Korea). The extrusion at 350 °C with an extrusion speed of 0.5 mms^{-1} and an extrusion ratio of 18:1 was conducted in Centro Nacional de Investigaciones Metalurgicas (CENIM) Madrid. The nominal compositions of the prepared alloys are listed in Table 3.1.

Table 3.1. Composition of the investigated alloys

Designation	Composition (wt.%) [Mg +]	Composition (at.%) [Mg +]
WZ42	3.5 % Y + 1.6 % Zn	1.0 % Y + 0.5 % Zn
WZ104	10.0 % Y + 3.7 % Zn	3.0 % Y + 1.5 % Zn

3.2. Scanning electron microscopy (SEM)

The microstructure of the Mg alloys with the LPSO phase was investigated by SEM FEI Quanta™ FX200 and ZEISS Auriga, both equipped with field emission gun (FEG), EDAX Energy Dispersive X-ray (EDX) detector and EDAX EBSD detector.

The high quality of the sample's surface is essential to get reliable information from the microstructural observations. Samples for the microscopic studies were cut from the middle of the extruded bars as the longitudinal section using an Accutom-50 machine from Struers®. The specimens were ground with TegraPol-15 polishing machine from Struers® on SiC grinding papers from P1200 to P4000. In addition, they were polished by a diamond paste with a particle size of 3, 1 and 0.25 μm. For the

[1] CaO has been used as a replacement of the SF_6 gas, known as a greenhouse gas, usually used for preventing the ignition of the Mg alloys during the casting [139–142]. Moreover, in some papers it has been shown that the addition of CaO has a beneficial effect on the corrosion resistance and mechanical properties of the Mg alloys [139, 143, 144].

EBSD measurements, the last step of specimen surface preparation was the Ar ion polishing using a Leica EM RES102 system.

The EBSD mapping in present work was carried out with a step size of 0.4 μm at a working distance of 13 mm (in FEI Quanta) and 7 mm (in ZEISS Auriga) and at an acceleration voltage of 15 kV. The data acquisition software program TSL-OIM Analysis 7.0 was used to process acquired EBSD data.

Backscattered electrons (BSE) are sensitive to the atomic number of the nuclei they scatter from. Heavy elements (with bigger atoms) scatter electron more likely than lighter elements, thus, in the BSE images, they have brighter contrast. In the present work, BSE images are presented because they give essential information about the distribution of the LPSO phase in the investigated alloys: the LPSO phase, containing Zn and Y having heavier atoms than Mg, is represented in bright contrast in the BSE images.

The EBSD technique is a great tool for determination of the crystallographic orientation, texture, grains size, distribution, the misorientation and shape of individual grains, types of grain boundaries and other microstructural features. For EBSD observations, the well-polished sample is tilted by 70° from a horizontal position towards the EBSD camera to increase the contrast in the resultant electron backscatter diffraction pattern. When an incident beam is interacting with the sample, the electrons are backscattered on lattice planes, satisfying the Bragg´s condition for many different planes. As a result, Kikuchi pattern (i.e. a set of Kikuchi bands) are formed. Each Kikuchi pattern corresponds to a specific crystallographic orientation and using Hough transformation the Miller indices can be determined. According to the orientation triangle, a specific color is linked to defined crystallographic orientation and an orientation image map (OIM), showing the crystallographic orientation of each measured pixel, can be created.

Further, based on EBSD data, evaluation of the misorientation parameters within each grain is useful for revealing the metallurgical state of the grains [145–147]. One of these parameters used in the thesis is the grain orientation spread (GOS). The characteristic calculation is based on the values of the misorientation angles between pixels for the specific grain. For the grain *i*, the GOS is calculated as:

$$GOS(i) = \frac{1}{J(i)} \sum_j \omega_{ij}, \tag{3.1.}$$

where *J(i)* is the number of pixels in the grain *i,* and ω_{ij} is the misorientation angle between the orientation of pixel *j* and the mean orientation of grain *i* [148]. Since the deformation of the material leads to a grain distortion, i.e. results in a high GOS value [148], this approach is useful for separate the deformation-free recrystallized grains with low GOS value from non-recrystallized grains having high values of GOS.

3.3 Transmission electron microscopy (TEM)

The structure of the LPSO phase and the precipitates formed in the alloys were studied by TEM JEOL 2000FX equipped with Bruker EDX detector, operating at 200 kV.

The samples were mechanically polished symmetrically from both sides on P1200 SiC paper until the thickness of 150 μm. Subsequently, they were polished on P4000 SiC paper down to a thickness of 100 μm. Afterward, discs with a diameter of 3 mm were cut from the polished samples and a dimple of the thickness of 50 μm was ground in the center of each disc. Dimples were created by the Gatan DIMPLE GRINDER MODEL 565. Finally, the specimens were ion-polished using a Leica EM RES102 system at accelerating voltage of 6-4 keV.

In TEM, the image is formed by the interaction of the electron beam with the sample when the beam is transmitted through the sample´s foil. Using the lenses, the electron beam is focused to the desired size and location. Coupling the deflections caused by magnetic and electrostatic fields in opposing directions allows the formation of a shift in a beam path, allowing for the beam shifting in TEM, which is the basis of the scanning transmission electron microscopy (STEM).

Fig. 3.1. shows an illustration of the basic operating modes of the TEM: imaging mode on the left side and diffraction mode on the right side. In the imaging mode, a bright field image is obtained by selecting the central beam, while in the case of selecting signal from the diffracted beam a dark field image is received. The diffraction mode is useful for determination of crystallographic structure and its orientation.

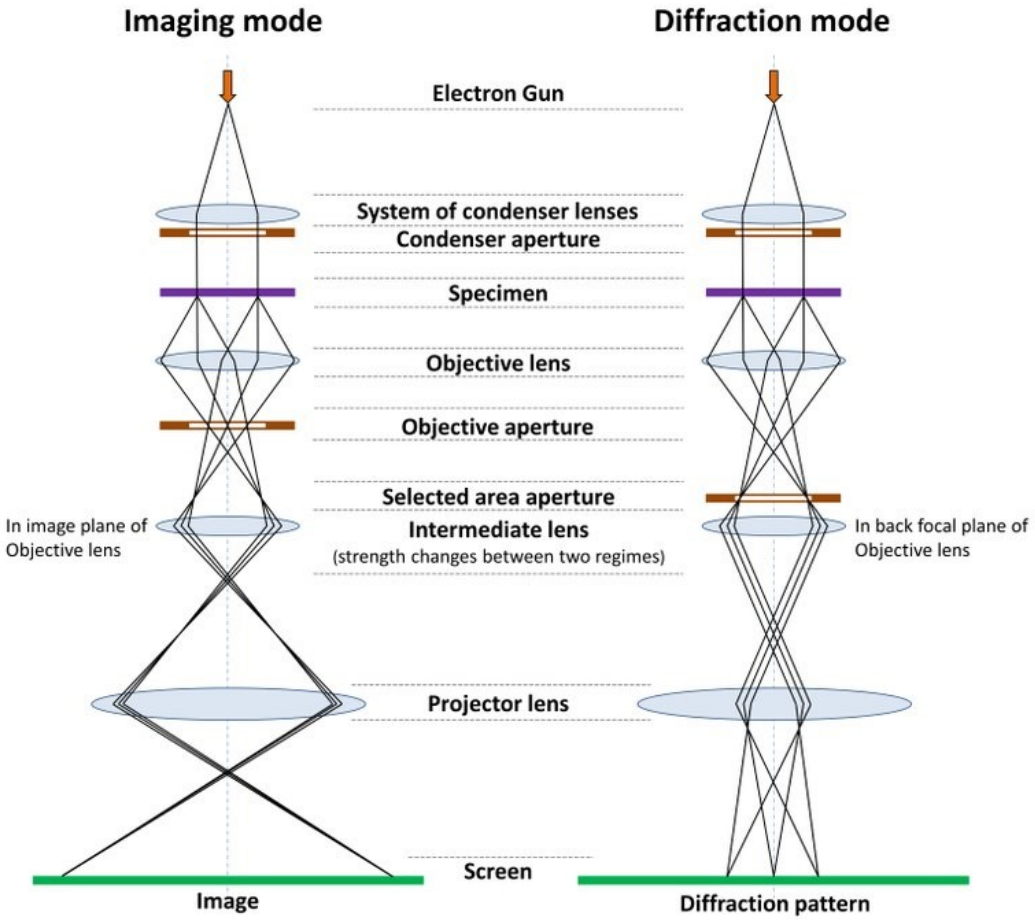

Fig. 3.1. Schematic view of imaging and diffraction modes in TEM [149].

3.4. Deformation tests

The deformation tests at RT with the concurrent AE measurements were performed in a universal testing machine INSTRON® 5882 at a constant strain rate of 10^{-3} s^{-1}. For compression tests, cylindrical specimens with a diameter of 5 mm and length of 10 mm were used. For tension tests, samples with a gauge length of 12 mm and a diameter of 5 mm with screw heads on both ends were machined from the extruded bars along the ED. All mechanical data were processed by program Origin® from the company OriginLab®.

The deformation tests with the concurrent synchrotron diffraction measurement were carried out on the P07 – HEMS (High Energy Materials Science) beamline of Petra III at DESY (Deutsches Elektronen-Synchrotron), Hamburg, Germany [150]. The compression specimens were placed in the chamber of a dilatometer DIL 805A/D (TA Instruments) combined with a modified heating

induction coil in order to enable the beam passing only through the sample [151]. The specimens were compressed at RT, at 200 °C, 300 °C, and at 350 °C with a strain rate of 10^{-3} s^{-1}. To control the temperature of the samples a thermocouple was attached to the sample. For the tests at elevated temperatures, the specimens were heated to the test temperature at a rate of 30 °C/s and held for 180 s before the compression start to ensure even temperature distribution. The tests were terminated at an engineering strain of 30%.

3.5. In-situ synchrotron diffraction

The *in-situ* synchrotron diffraction experiments were carried out on the P07 – HEMS beamline of Petra III at DESY, as it was mentioned above. The experimental setup is shown in Fig. 3.3. A monochromatic beam with the energy of 98.5 keV (λ = 0.01258 nm) and with a cross section of 1 x 1 mm^2 was used. The diffraction patterns were recorded using an acquisition time of 1 s by a Perkin-Elmer XRD 1622 flat panel detector with an array of 2048^2 pixels, and with an effective pixel size of 200×200 μm^2. LaB_6 was used as a reference to calibrate the acquired diffraction spectra. The detector-to-sample distance was set as 1 621 mm. Conventional 2θ diffraction profiles were obtained by azimuthal integration of the Debye-Scherrer rings in the axial and radial direction using the software Fit2D (Fig. 3.2.) [152]. Afterward, to determine the peak position and its intensity the acquired data were fitted using the Gaussian function and Wolfram Mathematica software.

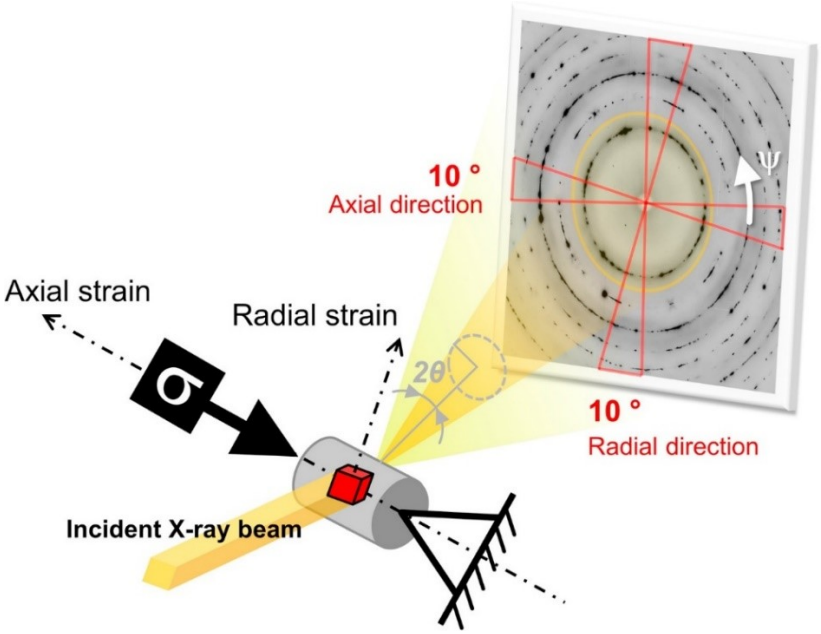

Fig. 3.2. The experimental setup for the in-situ synchrotron diffraction measurements and the principle of the data evaluation for the axial and radial directions [153]. *Ψ is the azimuthal angle.*

3.6. Acoustic emission

The AE response was collected concurrently with the room temperature deformation tests by a computer-controlled MICRO-II system developed by Physical Acoustics Corporation (PAC) which allows continuous storage of the AE signals. A piezoelectric PICO SIN 7549 (PAC) sensor with a diameter of 3 mm and a relatively flat response in a frequency band from 200 to 750 kHz was used. A sampling frequency was set as 2 MHz. To ensure the high AE signal to noise ratio a 60 dB preamplifier was employed. The sensor was attached to the sample with the help of a clamp, and silicone grease was applied to improve the contact between the sample and the sensor. The threshold level was set as 26 dB, just above the background noise.

The recorded data was processed by the NOESIS^{TM} software, developed for advanced data analysis pattern recognition. The AE count rate, i.e. the number of AE counts per second, was evaluated to reveal the AE activity at a particular stage of the deformation. In order to find a correlation between the AE signal and the deformation mechanisms, the ASK analysis was performed (section 1.6.2.2.). For the calculation of the PSD functions during the ASK analysis, a time window of 2 048 μs was set.

4. Results and discussion

4.1 Characterization of the initial microstructure

4.1.1. Experimental results: SEM characterization of the as-extruded microstructure

The initial microstructure of the investigated materials, presented in Figs. 4.1. - 4.3., is studied by SEM, including BSE imaging and EBSD mapping. The microstructure of both studied Mg alloys consists of the α–Mg matrix having dark contrast in BSE images and the LPSO phase elongated along ED with gray-white contrast in BSE images, see Fig. 4.1. Besides the LPSO phase, some cubic shaped precipitates, marked by red arrows in Fig. 4.1., are observed in both alloys. The detailed analysis of the precipitates is provided by TEM and EDAX (chapter 4.1.2.).

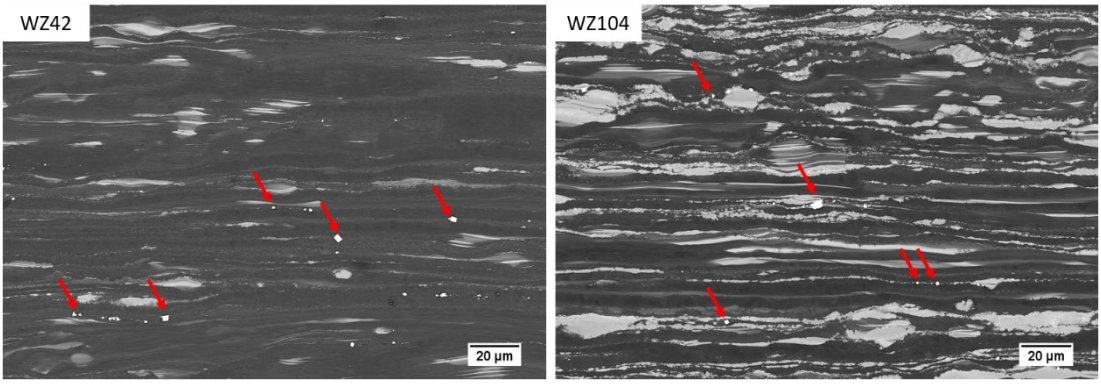

Fig. 4.1. BSE images of the microstructures of the as-extruded WZ42 and WZ104 alloys (ED→). Red arrows indicate cubic shaped precipitates.

To get information about the crystallographic orientation of the Mg matrix, the EBSD technique was employed. The orientation image maps (OIMs) are presented in Figs. 4.2. and 4.3 for the WZ42 and WZ104 alloys, respectively. For the EBSD data, a confidence index (CI) is used to indicate the degree of confidence that the orientation calculation is correct [154]. The black regions in the OIMs correspond to the regions with CI < 0.1, i.e. the system cannot analyze the Kikuchi-diffraction patterns. By comparing the results obtained by the EBSD technique with those of SEM, it is confirmed that the black regions correspond to the LPSO phase.

By the OIMs it has been revealed that the Mg matrix consists of dynamically-recrystallized (DRX) grains and non-recrystallized (non-DRX) grains elongated along ED. To distinguish recrystallized grain from non-recrystallized grains, the criterion of recrystallized grains having GOS smaller than 1° is applied. The volume fractions of individual phases and the size of the recrystallized grains are summarized in Table 4.1. The volume fraction of the LPSO phase increases with the increasing amount of alloying elements – Y and Zn. At the same time, the volume fraction of the elongated grains decreases with the increasing amount of the alloying elements.

The texture of the Mg alloys was calculated from the EBSD data and it is presented in a form of inverse pole figures (IPFs) in Figs. 4.2 and 4.3. for the WZ42 and WZ104 alloys, respectively. Both alloys exhibit a strong $(10\bar{1}0)$ fiber texture with basal planes mainly oriented parallel to ED. To analyze the texture of the recrystallized and elongated grains separately, the grains are divided into groups based on the above mentioned GOS condition. As seen in Figs. 4.2. and 4.3., the recrystallized grains have a nearly random orientation with a maximum texture intensity of 1.612 and 1.352 m.r.d. (multiple of random density) for the WZ42 and WZ104 alloys, respectively. The non-recrystallized grains have a very strong texture with an intensity peak of 17.934 and 24.040 m.r.d. at $(10\bar{1}0)$ pole for the WZ42 and WZ104 alloys, respectively. Thus, these grains have a strong texture and have their basal planes oriented parallel to ED.

Table 4.1. The volume fraction of the LPSO phase, elongated (non-DRX) and recrystallized (DRX) grains, and the grain size of the DRX grains.

Mg alloy		**WZ42**	**WZ104**
Volume fraction	LPSO [%]	10 ± 2	32 ± 4
	Non-DRX grains [%]	31 ± 3	20 ± 3
	DRX grains [%]	59 ± 3	48 ± 3
Size of the DRX grains [μm]		2.04 ± 0.09	2.02 ± 0.07

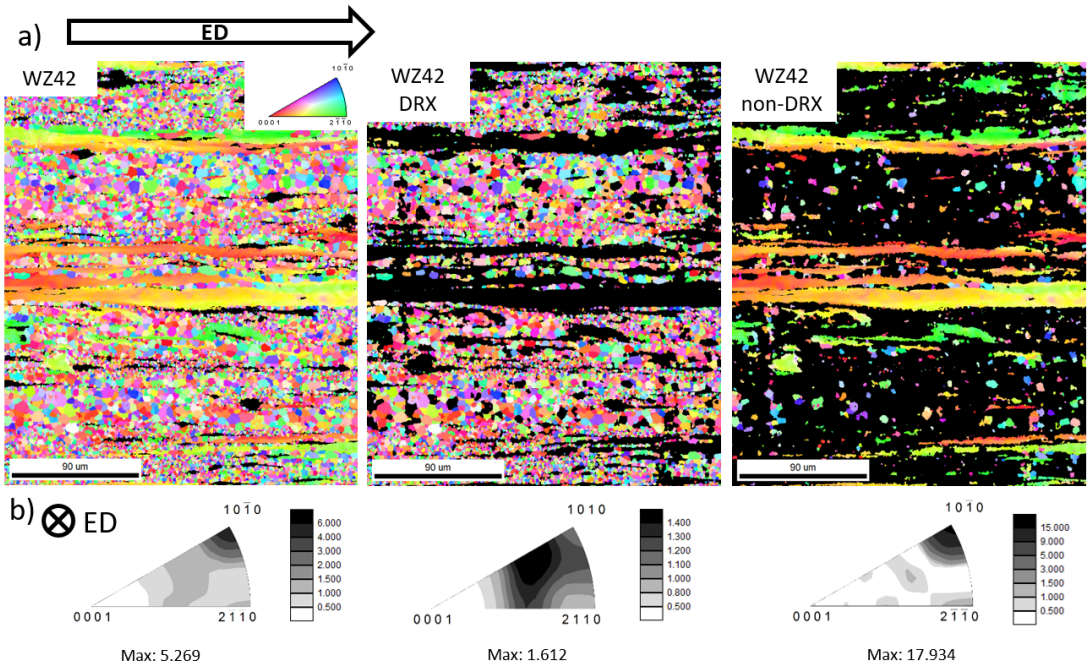

Fig. 4.2. a) The OIM of the longitudinal section of the WZ42 alloy with the orientation triangle. In addition, the OIM of the DRX and elongated (non-DRX) grains are shown. b) The IPFs calculated from the EBSD data for the complete map, the DRX, and non-DRX grains. The scale of the texture intensities is presented as the multiples of a random distribution (m.r.d.).

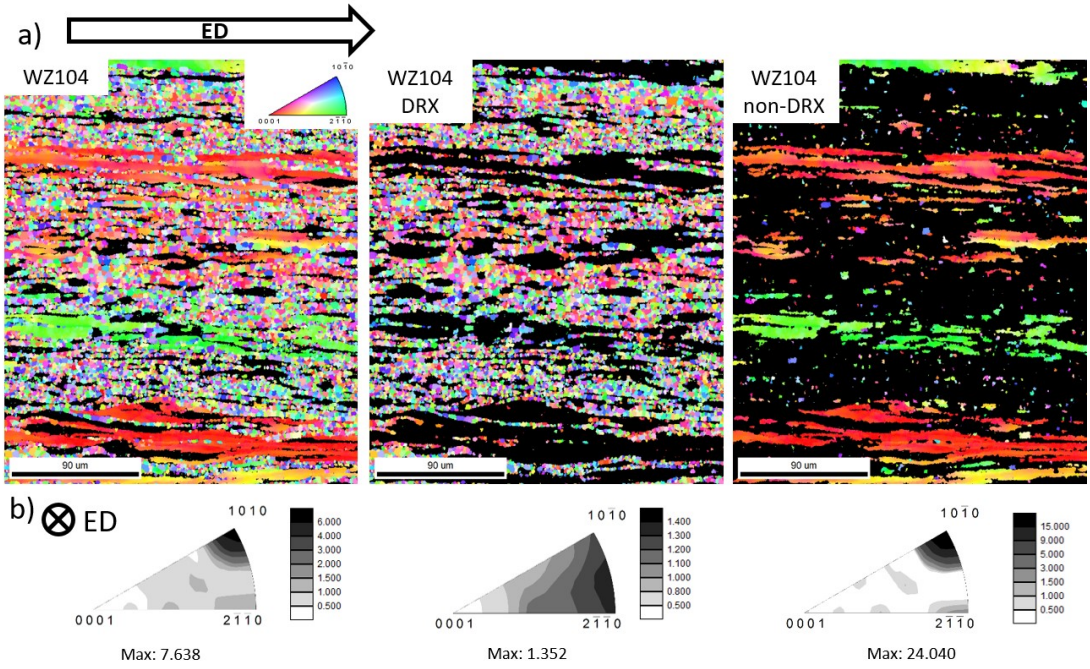

Fig. 4.3. a) The OIM of the longitudinal section of the WZ104 alloy with the orientation triangle. In addition, the OIM of the DRX and elongated (non-DRX) grains are shown. b) The IPFs calculated from the EBSD data for the complete map, the DRX, and non-DRX grains. The scale of the texture intensities is presented as the multiples of a random distribution (m.r.d.).

4.1.2. Experimental results: TEM characterization of the precipitates and the LPSO phase

Besides the LPSO phase, three different types of precipitates are found in both investigated alloys. Results of EDAX and selected area electron diffraction (SAED) analysis of the WZ104 alloy are presented in Figs. 4.4. - 4.6.

The addition of CaO during the casting led to a formation of Mg_2Ca particles throughout the microstructure of both alloys (Fig. 4.4.). The size of these precipitates was estimated to be around 100 – 200 nm. They have a hexagonal (not closed packed) structure with $a = 6.2$ *Å* and the ratio of *c/a* about 1.6. The Mg element is homogeneously distributed in the investigated area, while a significant amount of Y and Zn can be seen in the upper left corner indicating the presence of the LPSO phase.

Secondary phases located preferentially at grain boundaries have been identified by SAED patterns and EDAX analysis as W-phase ($Mg_3Y_2Zn_3$), Fig. 4.5. The lattice parameter of the *fcc* structure ($Fm\bar{3}m$) of the W-phase was determined as $a = 6.9$ *Å*. Their average size is between 150 and 300 nm. The double diffraction in Fig. 4.5.c is caused by Mg-matrix on the background.

The particles already seen in the BSE images (Fig. 4.1.) with a size around 1 μm were identified as Y-rich particles with *fcc* structure and with a lattice parameter $a = 5.2$ *Å*, see Fig. 4.6.

In all of the Figs. 4.4. - 4.6., grains enriched with Zn and Y, corresponding to grains with the LPSO phase were found and marked by red arrows. To analyze the structure of the LPSO phase, TEM and STEM were employed. The obtained results are shown in Fig. 4.7.

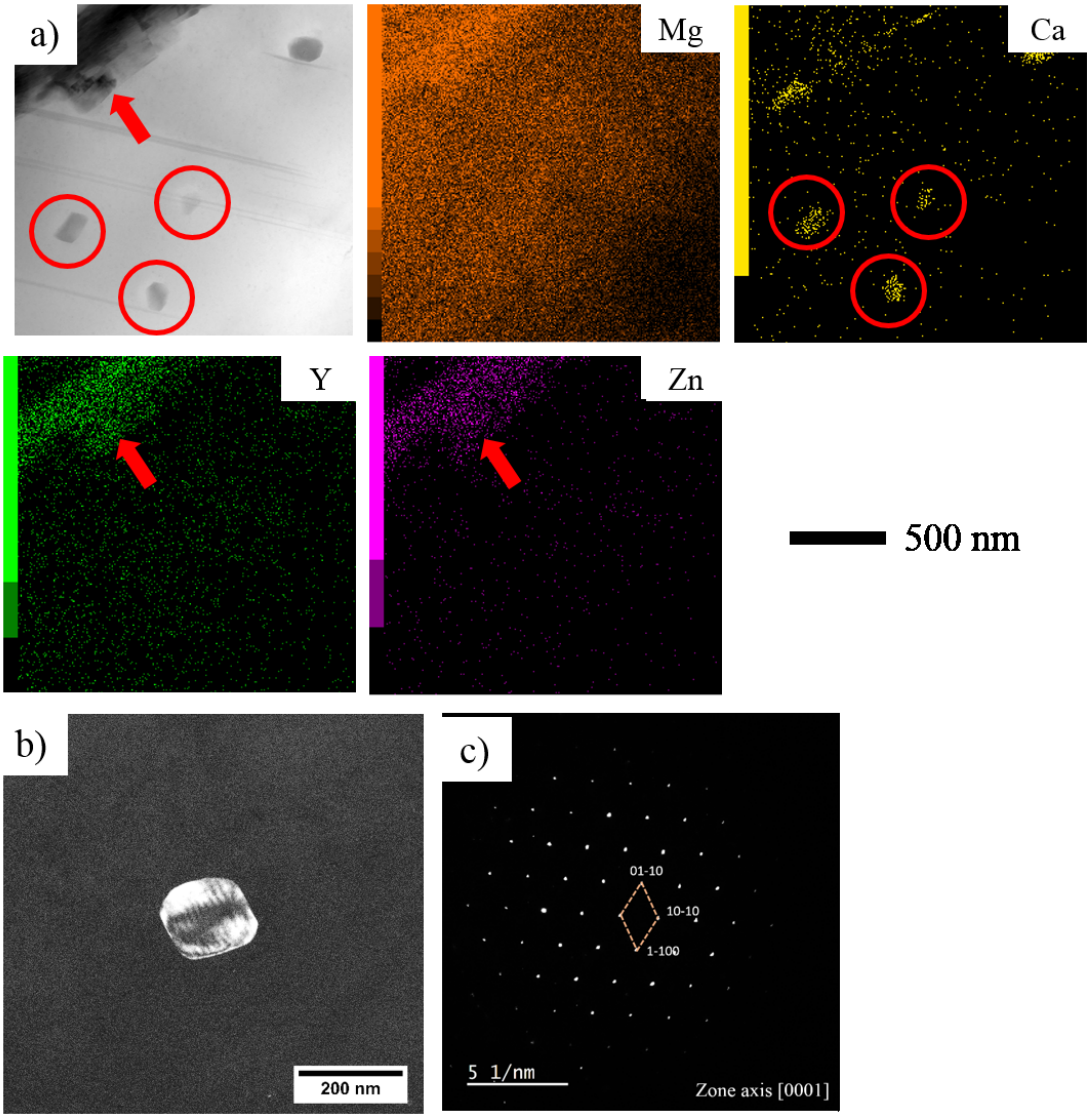

Fig. 4.4. a) EDAX analysis, b) dark field image and c) SAED diffraction pattern of Mg_2Ca particles. The grain containing the LPSO phase is marked by the red arrow.

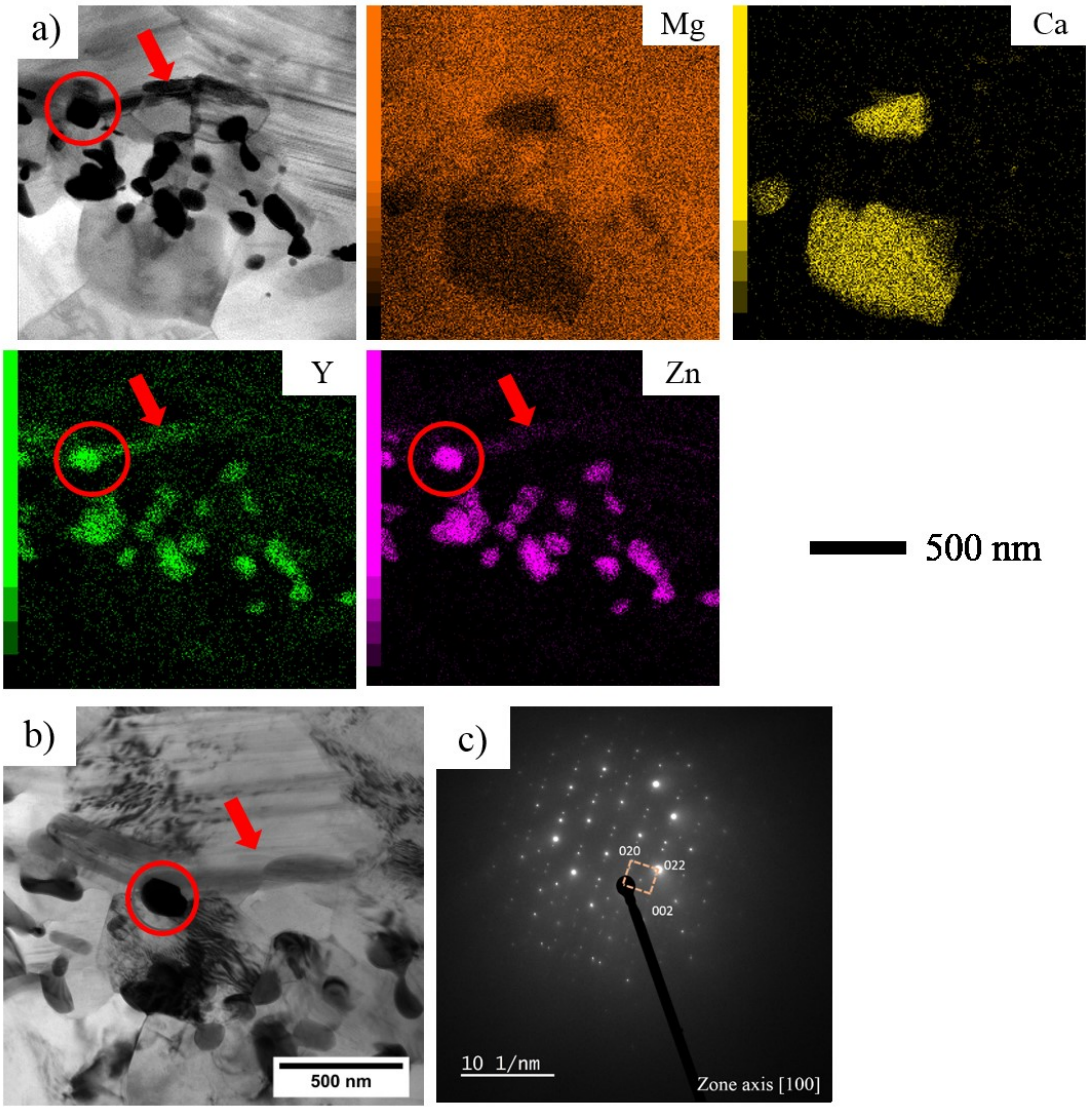

Fig. 4.5. a) EDAX analysis, b) bright field image and c) SAED diffraction pattern of the W-phase ($Mg_3Y_2Zn_3$) particle - marked by the red circle. The grain containing the LPSO phase is marked by the red arrow.

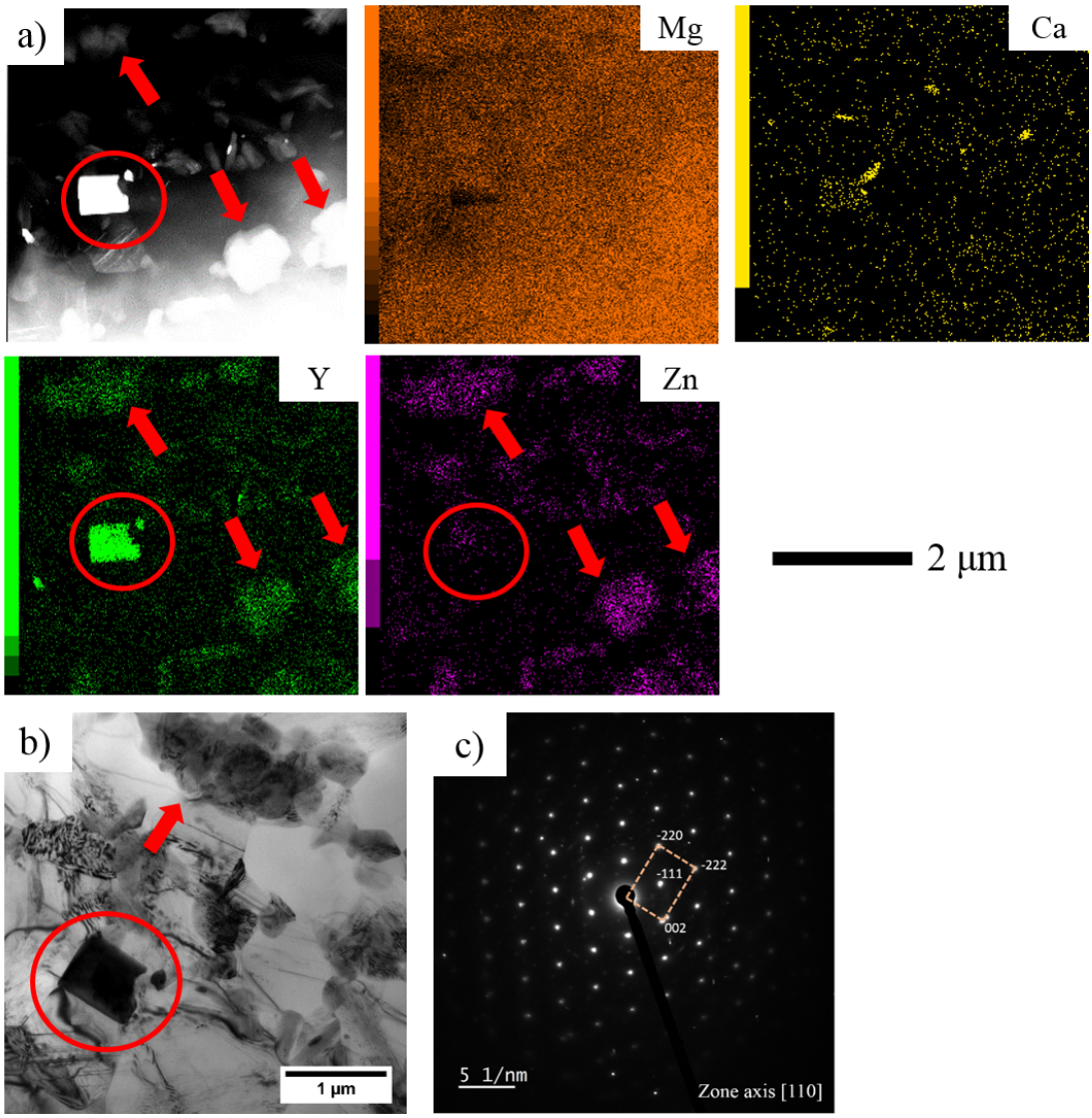

Fig. 4.6. a) EDAX analysis, b) bright field image and c) SAED diffraction pattern of the Y-rich particle – marked by the red circle. The grains containing the LPSO phase are marked by red arrows.

The grain, highlighted in the red circle in Fig. 4.7.a, has a dark contrast because it contains Zn and Y atoms, which form the LPSO phase and it is in diffraction contrast. The SAED pattern from the grain is presented in Fig. 4.7.b. From the diffraction peak appearances along the c^* direction, the stacking structure of 18R is identified [155]. Fig 4.7. c and d show the Z-contrast STEM images of the WZ104 alloy. The distribution of the Zn/Y on the atomic planes and the relevant stacking structure was revealed by STEM. The structure of two closed-packed layers enriched by Zn/Y (red

lines) followed by four layers of the Mg structure (black lines), shown in Fig. 4.7.d, corresponds also to the 18R-type LPSO phase (see Fig. 1.7.).

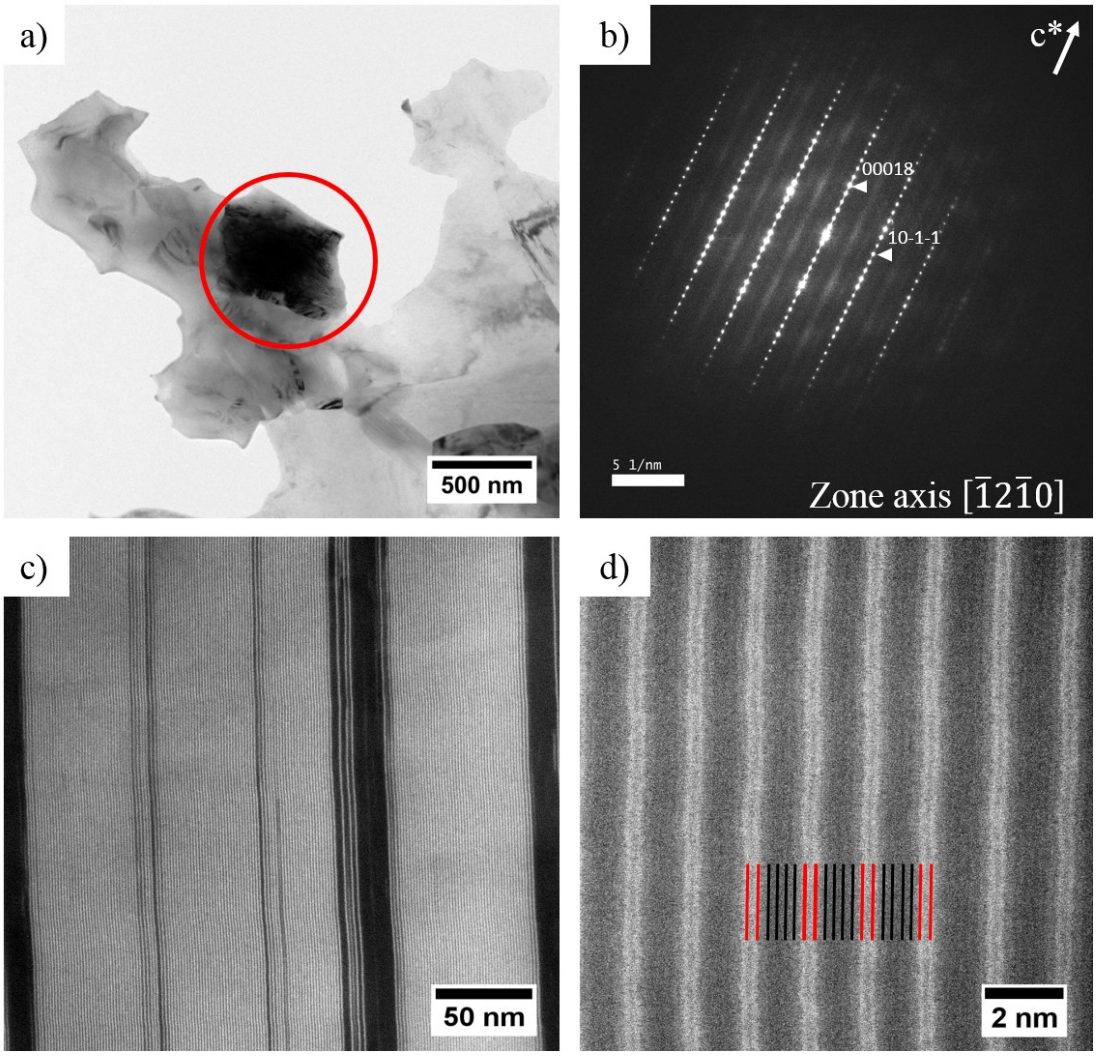

Fig. 4.7. a) Bright field image of the WZ104 alloy; b) the SAED pattern of the LPSO grain marked by the red circle and its STEM images at different magnifications (c-d).

4.1.3. Experimental results: synchrotron diffraction from the as-extruded materials

The synchrotron diffraction measurement provides more details on the structure of the LPSO phase and texture of the material. The Debye-Scherrer rings, recorded by the flat-panel 2D detector, of the as-extruded materials are shown in Fig. 4.8. The diffraction patterns as a function of 2θ angle (Fig. 4.8.b) were obtained by the integration of the Debye-Scherrer rings using Fit2D software [152]. Axial and

radial diffraction patterns are thus obtained by azimuthal integration of the Debye-Scherrer rings between ±10° about the axial and radial directions (see Fig. 3.2.), respectively.

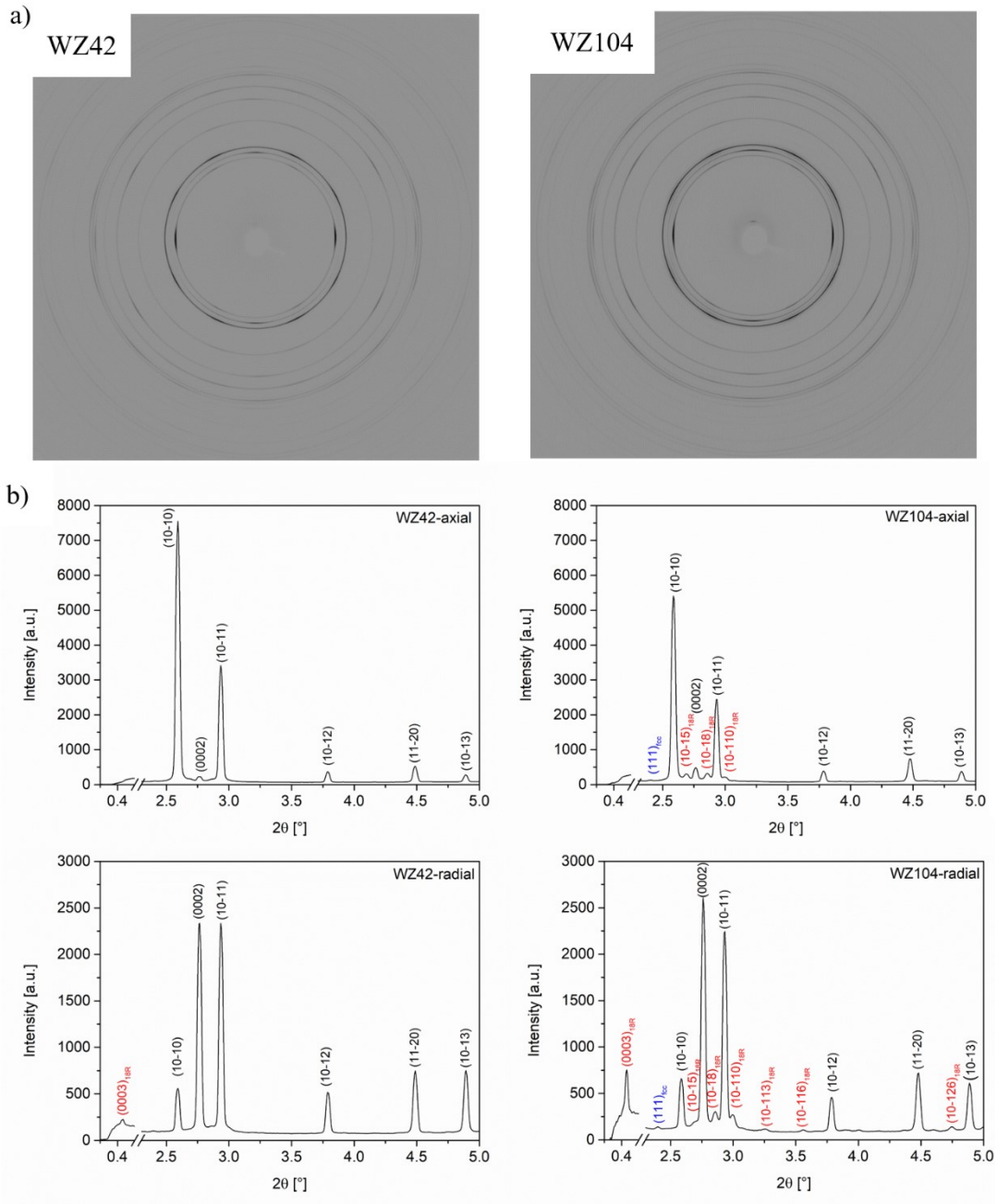

Fig. 4.8. a) Synchrotron radiation diffraction pattern of the as-extruded WZ42 and WZ104 alloys recorded on the 2D flat-panel detector. b) axial and radial diffraction patterns as a function of 2θ obtained by integration of the data in (a).

Please note that the axial diffraction pattern is obtained from the planes close to perpendicular to ED and the radial diffraction pattern is obtained from planes parallel to ED. The diffraction peaks related to the Mg matrix are indexed in black, LPSO phase – in red, and the *fcc* phase related to the Y-rich precipitates – in blue. The LPSO phase is confirmed to be an 18R phase with $P3_212$ crystal structure with the lattice parameters $a = 0.323$ and $c = 4.697$ nm in the hexagonal convention. In the WZ42 alloy, the LPSO phase gives only one diffraction peak with a very low intensity owing to its low volume fraction in this alloy. Whereas, several reflections of the 18R structure were detected in the WZ104 alloy. For both alloys, the $\{10\bar{1}0\}$ planes show a strong diffraction peak in the axial direction in contrast to the radial direction, where the (0002) diffraction peak is the most intense. The LPSO phase has an intense (0003) diffraction peak of the 18R structure located at $2\theta = 0.45°$ in the radial diffraction pattern of the WZ104 alloy. Other well-separated LPSO diffraction peaks are: $\{10\bar{1}5\}$ and $\{10\bar{1}8\}$ in the axial diffraction pattern and $\{10\bar{1}10\}$, $\{10\bar{1}13\}$, $\{10\bar{1}16\}$, and $\{10\bar{1}26\}$ in the radial diffraction pattern.

4.1.4. Discussion: effect of the amount of the LPSO phase on the microstructure

The bimodal microstructure observed in both investigated Mg alloys is a result of the extrusion process. Both investigated alloys exhibit a characteristic microstructure, which is similar to that previously shown in Mg–Y–Zn alloys, extruded at 350 °C with an extrusion ratio of 4:1, containing a different amount of the LPSO phase [14, 113, 156]. It has been reported by Bohlen et al. [112] that bimodal microstructure, consisting of non-recrystallized grains elongated along ED and small recrystallized grains, is formed in Mg alloys when low extrusion speed is applied. In Table 4.1. it is clearly shown that the volume fraction of the elongated and recrystallized Mg grains decreases with the increasing volume fraction of the LPSO phase, which strongly depends on the amount of alloying elements. Similar results were presented by Oñorbe et al. [9], where it has been shown that a particle-stimulated nucleation (PSN) process can control the recrystallization process in Mg-LPSO alloys.

Both alloys exhibit a strong $(10\bar{1}0)$ fiber texture with basal planes oriented parallel to ED caused mainly by non-recrystallized elongated grains. Similar texture has been observed in other extruded Mg alloys and the dominant contribution of the non-recrystallized grains, having their basal planes oriented parallel to ED, to the

initial texture has been shown in [4, 12, 58, 112–116]. These works are in good agreement with the presented results. It is confirmed in Figs. 4.2. and 4.3. that the elongated grains have their basal planes oriented strictly parallel to ED, forming a very intensive texture while the recrystallized ones are nearly randomly oriented with a maximum texture intensity around 1.5 m.r.d.

The strong fiber texture results in high contrast in intensities of the $\{10\bar{1}0\}$ and (0002) diffraction peaks in the axial and radial direction (Fig. 4.8.). The LPSO phase also has a basal texture quite similar to that of the Mg matrix. Similar textures have been reported previously in Mg-LPSO alloys containing 85% volume fraction of the LPSO phase [5, 157, 158].

In addition to the LPSO phase, precipitates of Mg_2Ca, W-phase and Y-rich phase were found in the alloys by TEM analysis. The Y-rich phase, which is visible in the SEM images (Fig. 4.1.) was also identified by synchrotron diffraction. The other precipitates were not found in the diffraction patterns, which indicates that their volume faction in these alloys is much lower compared to the Y-rich particles. These particles are most likely YH_2 particles, with *fcc* structure and a lattice parameter of a = 0.52 nm. They are common for thin films [159–161], however, their existence in bulk samples has been reported as well [162].

An addition of CaO in the Mg alloys containing the LPSO phase has a beneficial effect on the corrosion resistance and mechanical properties [139, 143, 144]. This led to the formation of the Mg_2Ca intermetallic compound.

Besides the LPSO phase, the W-phase is another ternary phase commonly observed in Mg-Zn-Y alloys [163, 164]. It has been already shown that despite the higher elastic modulus and hardness of W-phase compared to the Mg matrix, it has no strengthening effect in Mg-Zn-Y alloys [165, 166]. Moreover, in the alloys with Zn and Y exceeding 6 wt.%, the W-phase is distributed along the grain boundaries and forms a coarse network structure resulting in the deterioration of the mechanical properties of the material [167].

4.2. Deformation behavior of the Mg-LPSO alloys at room temperature

4.2.1. Yield strength asymmetry

The true stress-true strain deformation curves measured in compression and in tension along ED at RT for the WZ42 and WZ104 alloys are shown in Fig. 4.9. The tensile curve of both alloys has a convex shape. The WZ104 alloy shows higher tensile yield strength (TYS) and ultimate tensile strength (UTS), but lower ductility compared to the WZ42 alloy. The compression curve of the WZ42 alloy has a concave (S-shaped) character, typically observed for Mg alloys with basal texture, which have been compressed along ED. The stress plateau after the yield point is followed by significant work hardening. The hardening effect is less pronounced for the WZ104 alloy compared to the WZ42 alloy. The compressive yield strength (CYS), the ultimate compressive strength (UCS) and the elongation to failure are higher for the WZ104 alloy than that for the WZ42 alloy. The obtained mechanical properties are summarized in Table 4.2.

The difference in the tension-compression yield strength asymmetry is worth to be discussed in these alloys. The WZ42 alloy has higher yield strength in tension than in compression, typically observed in wrought Mg alloys [112, 168–170]. Contrary, the WZ104 alloy shows a reversed yield strength asymmetry.

The active deformation mechanisms leading to the observed deformation behavior and mechanical properties were studied in detail by *in-situ* methods of AE and synchrotron diffraction, and *post-mortem* SEM observations, including BSE imaging and EBSD technique. Results for the RT deformation are particularly discussed in the following section.

Table 4.2. Mechanical properties measured along ED of the WZ42 and WZ104 alloys

	TYS [MPa]	UTS [MPa]	Elongation [%]	CYS [MPa]	UCS [MPa]
WZ42	265 ± 2	365 ± 1	20.3 ± 0.1	248 ± 2	410 ± 3
WZ104	298 ± 3	441 ± 1	16.5 ± 0.3	332 ± 3	494 ± 4

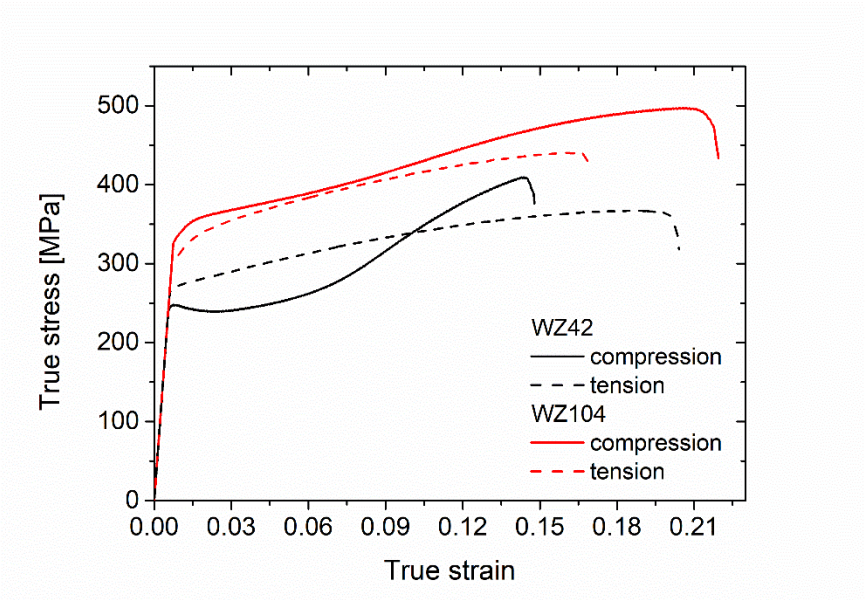

Fig. 4.9. The true stress-true strain deformation curves for the WZ42 and WZ104 alloys deformed in compression and tension along ED at RT.

4.2.2. Experimental results: compressive deformation at room temperature

4.2.2.1. Acoustic emission

The time and engineering strain dependence of the applied compressive stress and the concurrent AE activity in the terms of the AE count rate and the amplitude of the raw AE signal for the WZ42 and WZ104 alloys are presented in Fig. 4.10. In both alloys, the AE signal is already produced during the elastic part of the deformation. The maximum of both the AE count rate and amplitude are observed shortly before the macroscopic yield point with a significant decrease after reaching the yield strength. The AE count rate shows nearly a two order of magnitude difference between the two alloys, with a higher count rate and amplitude for the WZ42 alloy compared to the WZ104 alloy. Please note the different scale of the AE amplitude for the alloys in Fig. 4.10. In both alloys, a high AE activity persists until the end of the deformation process with some high amplitude events appearing spontaneously during the entire loading. They are easier to be noticed in the WZ104 alloy because of the different scale for the AE amplitude.

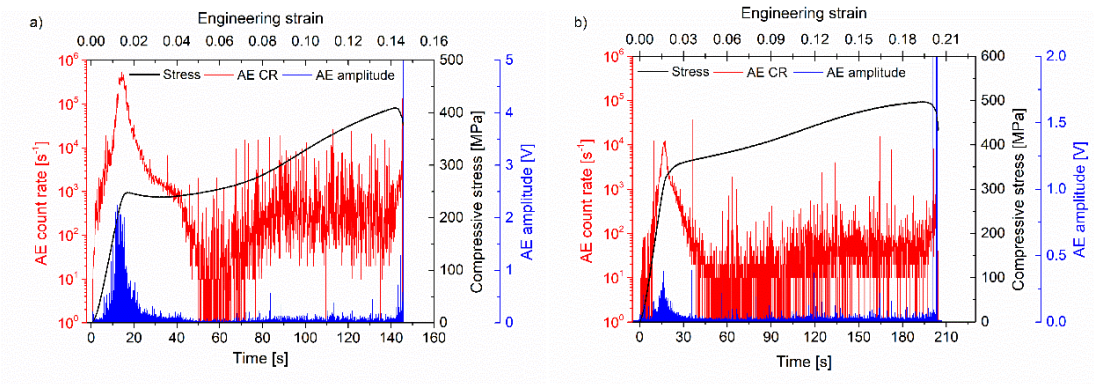

Fig. 4.10. Time and engineering strain dependence of the compressive stress and the corresponding AE response (AE count rate and AE amplitude of the raw signal) of the a) WZ42, and b) WZ104 alloy. Please note the different scale for the AE amplitude in the graphs.

As the result of the statistical analysis of the AE signal (ASK analysis), the time evolution of the cumulative number of events and the cumulative energy of the AE signal during compression of the WZ42 and WZ104 alloy along ED are shown in Figs. 4.11.a-b and 4.12.a-b, respectively. In Figs. 4.11.c and 4.12.c the energy – median frequency cross-plots are presented. Thus, the plots in a) sum up the number of events as they occur in the clusters and the plots b) sum up their respective energies with respect to time. The overlapping of the clusters in the plots c) are given by the 2D projection of a multidimensional space. Nevertheless, from the statistical point of view, the clusters are well separated.

The assignment of the clusters to the deformation mechanisms is not straightforward. The significant difference between the time evolution of different clusters helps to link deformation mechanisms to the clusters. Cluster 1 (noise) naturally occurs first in both experiments as the number of events, as well as cumulative energy, start to increase even before the start of the test. During the test, when the signals of other source mechanisms dominate the AE signal, the number of events and cumulative energy of the noise cluster remains constant. The number of events in Cluster 1 (noise) starts to slightly increase again at the later stage of deformation, where the AE amplitudes, in general, become low and AE originated from deformation processes are hardly distinguished from the background noise. This underlines that the signal of the particular mechanism dominates the assignment to a

specific cluster. Vice versa, it does not mean that the mechanism that does not dominate the AE signal is not active, they are just less “loud”. For example, mechanisms like uncorrelated dislocation motion or twin growth can be active at this point, but they simply do not produce detectable AE signal. The split of the Cluster 1, observed in Figs. 4.11.c and 4.12.c can be explained by the fact that in the later stage of deformation other noise mechanisms, e.g. friction, can contribute to this cluster.

At the onset of the deformation, the Cluster 2 dominates the AE signal for both alloys. Cluster 2 (red), associated with the basal slip, is found at medium energies in a wide range of median frequencies. The basal dislocation-type of the AE events usually exhibit a continuous character [127, 171], which is a convolution of small burst signals originated from dislocation avalanches [120].

Further, the evolution of the clusters is different for the two alloys. In the WZ42 alloy, slightly before the macroscopic yield point, the Cluster 3 (blue) gets the dominance of the AE signal. This cluster refers to events with high energy in a narrow median frequency range and therefore is associated with twin nucleation [8, 121, 137]. It is worth to keep in mind that twin growth will not cause AE and therefore it is not visible in AE signal as well as in the corresponding cluster identified here. Thus, AE events collected in the cluster are associated with twinning originated by twin nucleation. It is interesting to note that twinning events collected before the macroscopic yield point contribute with high energy to the cumulative energy of the cluster, while those detected after the yield point add a relatively low contribution to the overall energy. When the cluster of twinning grows to its maximum value, the cluster of the basal slips becomes the dominant one again. Cluster 4 initiates after the plateau on the deformation curve and continues to increase till the end of deformation in both: the events and energy. The average energy level of the events in Cluster 4 (green, Fig. 4.11.) is lower compared to that for the cluster of the basal slip, thus this cluster is related to the non-basal slip. So far, the ASK algorithm cannot make a difference between particular non-basal slip types (prismatic or pyramidal <a>-slip, <c+a>-slip).

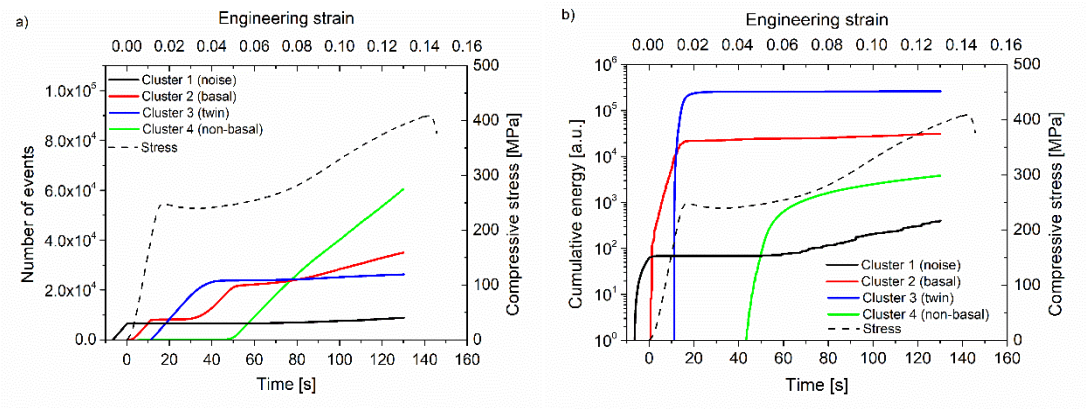

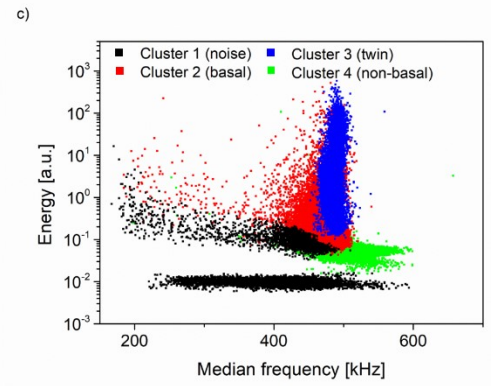

Fig. 4.11. a) The number of events representing the cumulative number of time frames assigned to each cluster and b) the cumulative energy with respect to time; c) the dependence of energy on the median frequency for the WZ42 alloy compressed along ED.

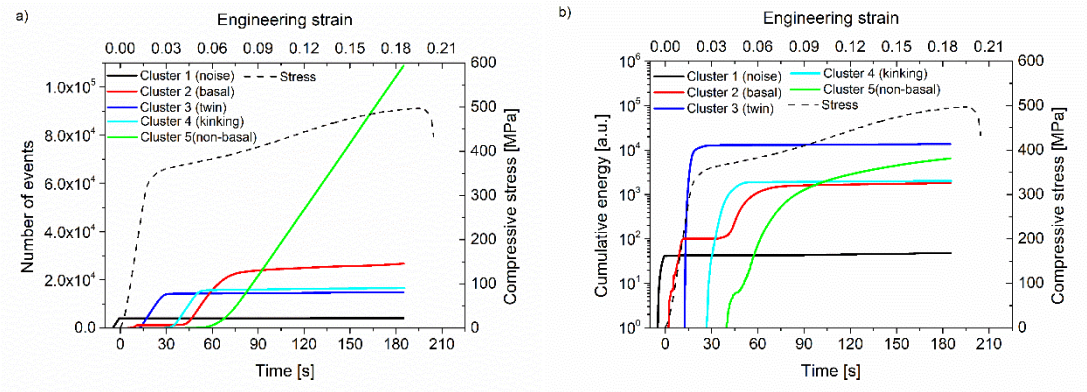

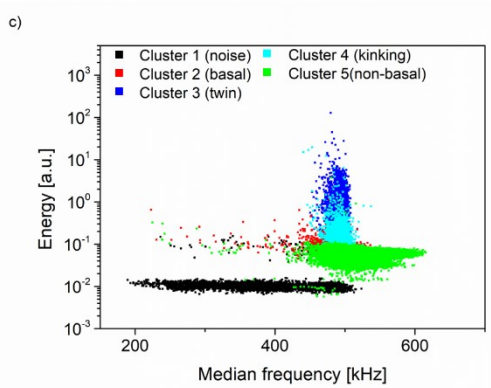

Fig. 4.12. a) The number of events representing the cumulative number of time frames assigned to each cluster and b) the cumulative energy with respect to time; c) the dependence of energy on the median frequency for the WZ104 alloy compressed along ED.

In the WZ104 alloy, similarly to the WZ42 alloy, the cluster of twinning controls the AE signal at the macroscopic yield point. However, the number of events and their energy is much lower, compared to that in the WZ42 alloy. Slightly above the macroscopic yield point, Cluster 4 (cyan, Fig. 4.12.) with relatively high energies starts to grow. The events of this cluster have a similar character to that of twinning. However, its energy is lower. This cluster is rather linked to kinking, the characteristic deformation mode of the LPSO phase. When it comes to its maximum values, the cluster of the basal slip becomes dominant again. It loses its dominance towards Cluster 5, which has similar characteristics of that of Cluster 4 for the WZ42 alloy, thus, associated with the non-basal slip. The non-basal slip dominates the further deformation of the WZ104 alloy.

4.2.2.2. Synchrotron diffraction

The compressive deformation curves, the stress dependence of the lattice strains and change in the intensities for the (0002) and $\{10\bar{1}0\}$ diffraction peaks in the axial direction as a function of the applied stress are shown in Fig. 4.13.a-b for the WZ42 and WZ104 alloys, respectively. Due to the diffraction geometry, each {hk.l} reflection in the diffraction pattern is associated with a distinct family of polycrystalline grains having their normal to the plane {hk.l} oriented in the direction of the diffraction vector. Therefore, the grains with their plane-normal oriented along the loading direction contribute to the data in the axial direction (see Fig. 3.2.). In other words, grains with the same crystallographic direction – aligned with the loading axis – contribute to the spectrum in the axial direction. However, the grains contributing to the given diffraction peak in the radial direction could be oriented at any rotational angle with respect to the loading axis [172]. Therefore, the information obtained from the axial direction can be in reasonable approximation analyzed and discussed without micromechanics modeling. On the other hand, it is almost impossible to do that without modeling for the radial diffraction peaks. This is the main reason why the experimental data obtained from the axial direction is preferentially used for discussion in the present work.

Hereafter, the changes in the lattice strains will be studied in the means of their absolute values.

In the elastic regime, the evolution of lattice strains on the Mg planes is linear with the applied stresses with identical slopes for both alloys. In the vicinity of the macroscopic yield point of the WZ42 alloy (Fig. 4.13.a), the grains with their $\{10\bar{1}1\}$- and $\{10\bar{1}2\}$ planes oriented parallel to the loading direction lose their elastic linearity.

The evolution of the (0002) lattice strain can be also seen in the middle plot in Fig. 4.13.a. The lattice strain on the (0002) plane loses its elastic linearity below the macroscopic yield point, around 209 MPa. During the micro-yielding, it decreases, while after the macroscopic yield point a linear increase with a slope lower than that in the elastic regime is observed. At the same time, the intensity of the (0002) peak increases slightly in the micro-yielding region (till 250 MPa) followed by a large increment after the macroscopic yield point (right plot).

Contrary to the WZ42 alloy, no micro-yielding is observed in the WZ104 alloy (Fig. 4.13.b). At stresses between 320 and 335 MPa, the $\{10\bar{1}1\}$- and $\{10\bar{1}2\}$ diffraction peaks lose their elastic linearity first. Similar to the WZ42 alloy, these grains are oriented parallel to the loading direction. At 335 MPa, i.e. at the macroscopic yield point, the (0002) lattice strain starts to decrease and it only starts to increase again at 365 MPa. The intensity of the (0002) diffraction peak starts to increase at the macroscopic yield point and it intensively rises up to 425 MPa. After this, its intensity is more or less constant. Correspondingly, the intensity of the $\{10\bar{1}1\}$ diffraction peak decreases. For the WZ104 alloy, it is possible to evaluate the lattice strain development on the $\{10\bar{1}8\}$ plane of the LPSO phase. Due to the positions and the intensities of the LPSO diffraction peaks in the axial direction, this is the only diffraction peak that could be reliably fitted during compression (Fig. 4.8.). It seems that the LPSO phase – based on the $\{10\bar{1}8\}$ diffraction peak - behaves elastically up to slightly higher stresses than that for the Mg matrix. The lattice strain on the $\{10\bar{1}8\}$ plane starts to rapidly increase after the macroscopic yield point. However, its evolution after 400 MPa is challenging. At these stresses the $\{10\bar{1}8\}$ diffraction peak is significantly overlapping with the (0002) Mg diffraction peak due to its intensive increase caused by twinning during the compression, see in Fig. 4.14.a.

The evolution of the $\{11\bar{2}0\}$ lattice strain is similar in both alloys. First, it increases intensively after reaching the macroscopic yield point. With the start of the

strain hardening of the alloys, lattice strain continues to increase with a slope slightly higher than that during the elastic regime.

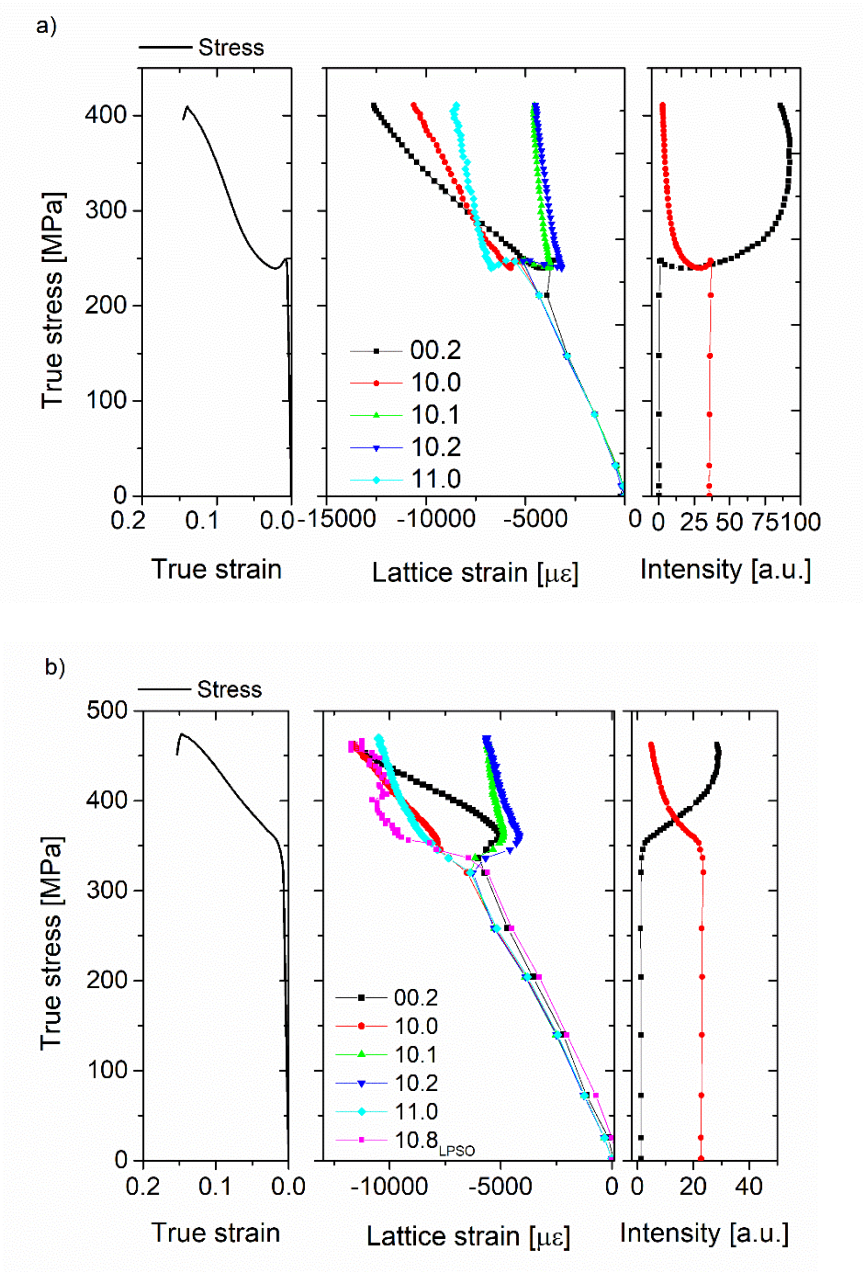

Fig. 4.13. Macroscopic stress-strain curves, the axial lattice strains as a function of the applied stress and evolution of the intensity of the major diffracted peaks of the Mg matrix during an in-situ compression test of the a) WZ42 and b) WZ104 alloy.

The axial distribution function of the (0002) diffraction peak before the deformation (in the as-extruded state) and at 12% of deformation of the WZ42 and WZ104 alloys is presented in Fig. 4.14.a. The axial distribution function is a cut

through the pole figure at a line from the center to the perimeter, thus the “angle” on the x-axis means the tilt from the loading direction (0° is along ED, 90° is perpendicular to ED). In the initial state of both alloys, the intensity of the (0002) peak is concentrated at 90°. With the ongoing deformation, the intensity at 90° decreases and a strong increase at 5° (in the loading direction) is observed in both alloys. This change is more significant for the WZ42 alloy than for the WZ104 alloy.

The twin volume fraction (TVF) is calculated by integrating the area under the axial distribution function of the (0002) diffraction peak till the cross-over point, see Fig. 4.14.b. Please note that the crossover point is always texture specific. The details of the TVF calculations are described in [16, 138, 173]. The calculated TVFs at RT as a function of the applied strain are plotted in Fig. 4.14.c. The TVF of the Mg matrix after the deformation to 12% of true strain is 53% and 31% for the WZ42 and WZ104 alloy, respectively.

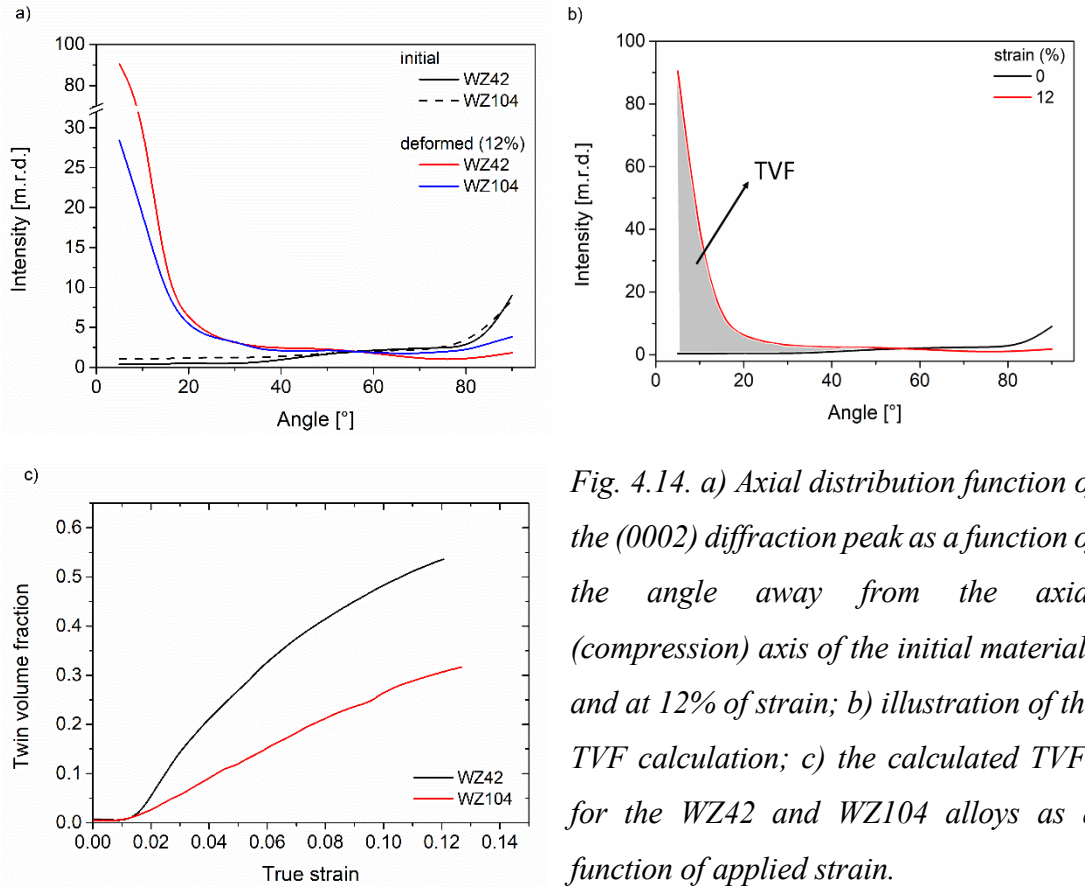

Fig. 4.14. a) Axial distribution function of the (0002) diffraction peak as a function of the angle away from the axial (compression) axis of the initial materials and at 12% of strain; b) illustration of the TVF calculation; c) the calculated TVFs for the WZ42 and WZ104 alloys as a function of applied strain.

4.2.2.3. Microscopy

In order to provide information about the deformed microstructure, EBSD measurements and BSE imaging were performed.

The microstructure of the WZ42 alloy deformed at RT up to 2% of plastic strain and till fracture is presented in Fig. 4.15.a and b, respectively. In the sample deformed up to 2% of strain, a lot of narrow twins can be observed not only in the elongated grains but also in the recrystallized grains well oriented for the activation of extension twins. The high angle grain boundaries are marked by black color, while the boundaries of the $\{10\bar{1}2\}\langle 10\bar{1}1\rangle$ extension twins are marked by red color in Fig. 4.15.a. The extension twin system reorients the basal planes by 86.3° towards the loading direction. Therefore, the activity of this twin system is also visible in the calculated IPF (lower right corner of Fig. 4.15.a), where an intensity at the (0001) pole is formed during loading. With the further deformation, the twins proceed to develop and after the fracture, the whole elongated grains are reoriented by nearly 90° resulting in the strong texture component at the (0001) pole, Fig. 4.15.b. No other twin type was observed in the alloy. It can be assumed from the GOS map (Fig. 4.15.b) that the deformation is homogeneously distributed in the recrystallized grains, but the elongated grains store a relative high deformation.

Contrary to the WZ42 alloy, at 2% of plastic deformation of the WZ104 alloy, presented in Fig. 4.16.a, only a few narrow twins are observed in the elongated grains and their presence is not seen in the IPF map (no intensity in the (0001) pole). However, in the microstructure obtained after the fracture (Fig. 4.16.b), the majority of the elongated grains are reoriented with their basal planes perpendicular to the loading direction resulting in intensive texture maximum at the (0001) pole.

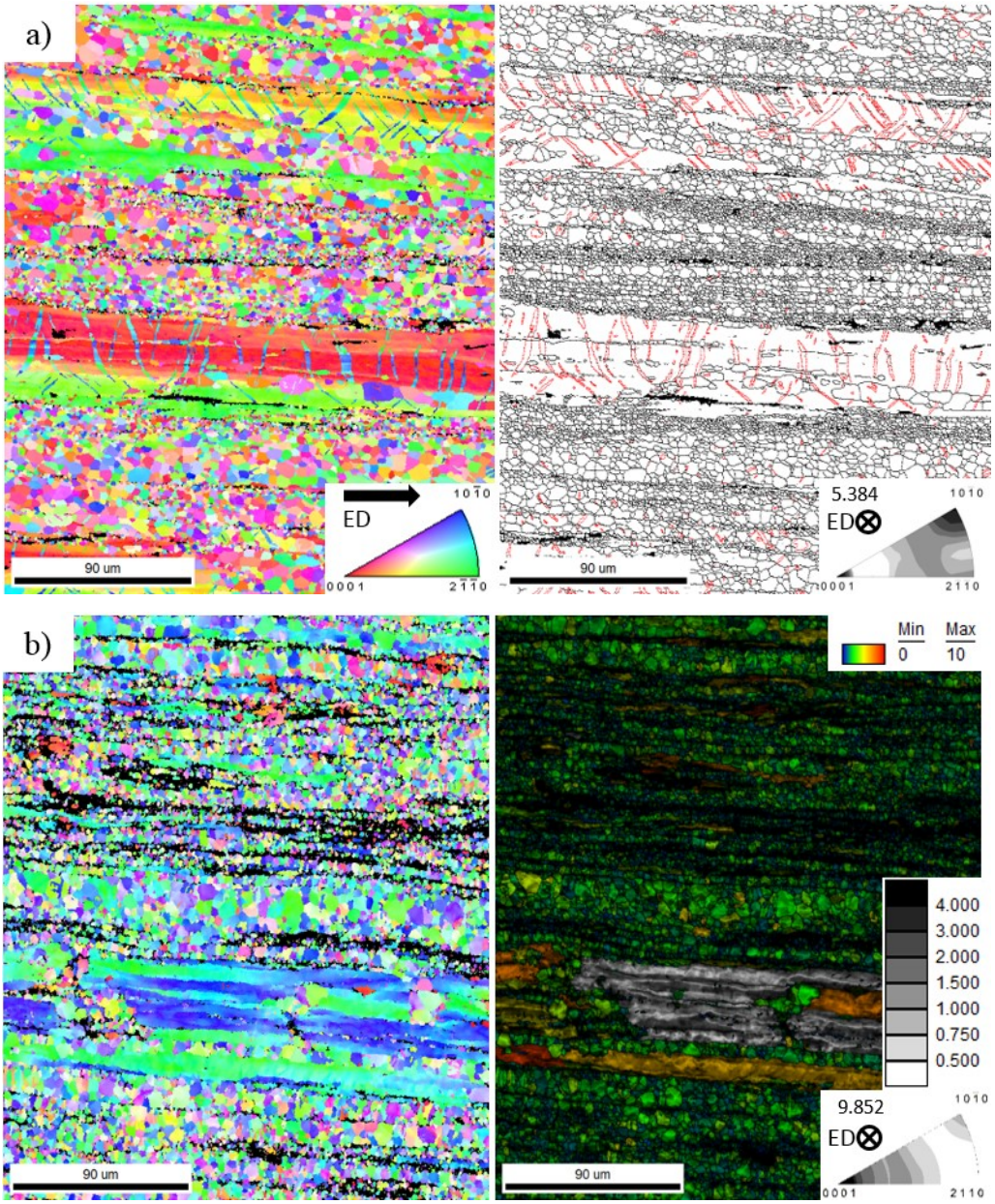

Fig. 4.15. Microstructure of the WZ42 alloy deformed up to a) 2% of strain -the OIM and the corresponding map of grain boundaries (black) and extension twin boundaries (red) together with calculated texture (IPF); b) till fracture - the OIM and the corresponding GOS map with calculated texture (IPF). Color-coded scale for the GOS map is depicted in the upper right corner. The numbers in the IPFs mark the maximum texture intensity as the multiple of random density (m.r.d.).

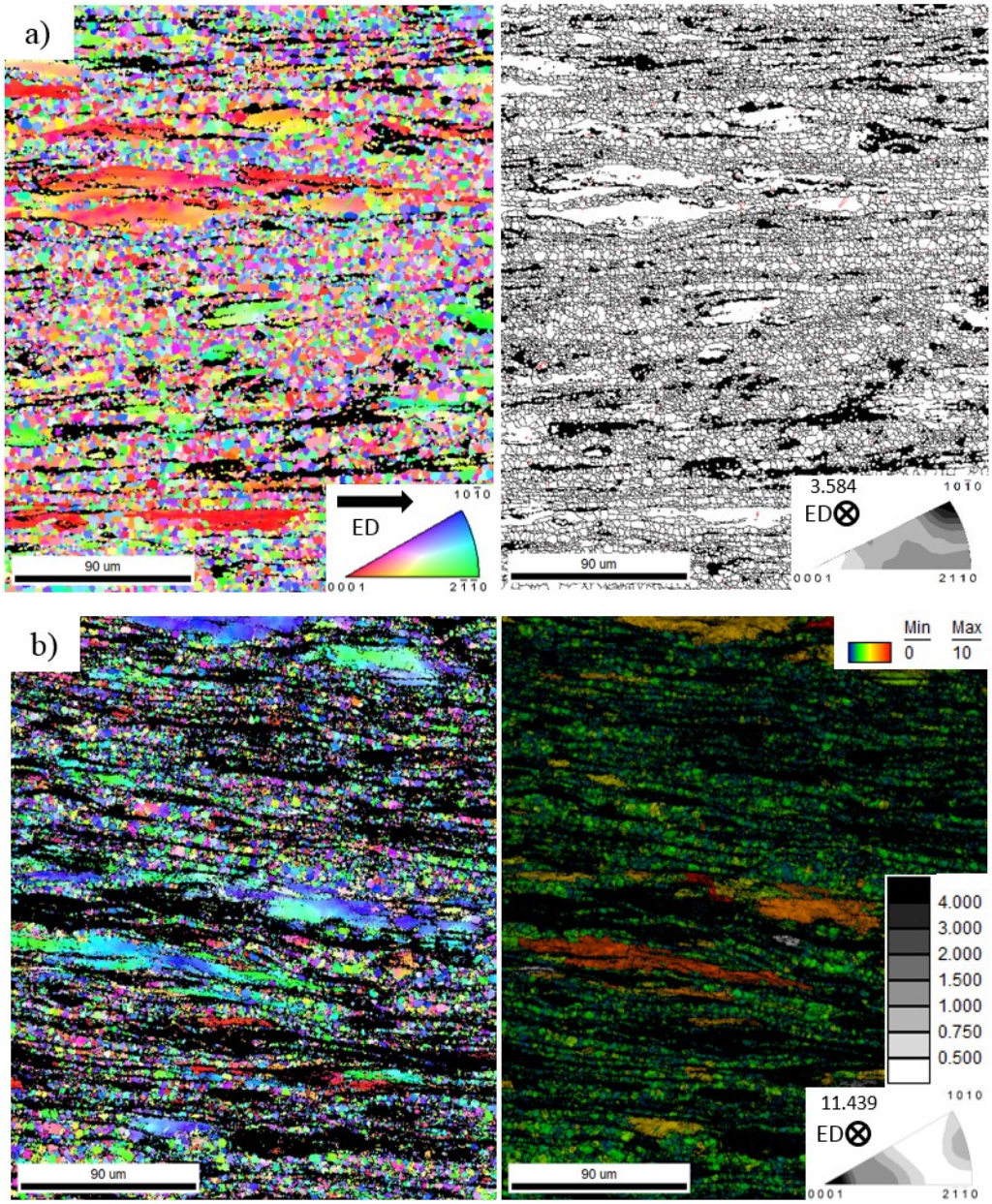

Fig. 4.16. Microstructure of the WZ104 alloy deformed up to a) 2% of strain -the OIM and the corresponding map of grain boundaries (black) and extension twin boundaries (red) together with calculated texture (IPF); b) till fracture - the OIM and the corresponding GOS map with calculated texture (IPF). Color-coded scale for the GOS map is depicted in the upper right corner. The numbers in the IPFs mark the maximum texture intensity as the multiple of random density (m.r.d.).

The EBSD technique cannot provide information about the LPSO phase due to its challenging diffraction. Therefore, the BSE images of the samples deformed until fracture were analyzed to obtain information about the deformation of the LPSO phase,

see Fig. 4.17. No kinks are found in the WZ42 alloy deformed up to fracture. On the other hand, the LPSO phase in the WZ104 alloy is found to be deformed by deformation kinking (highlighted by the red circle).

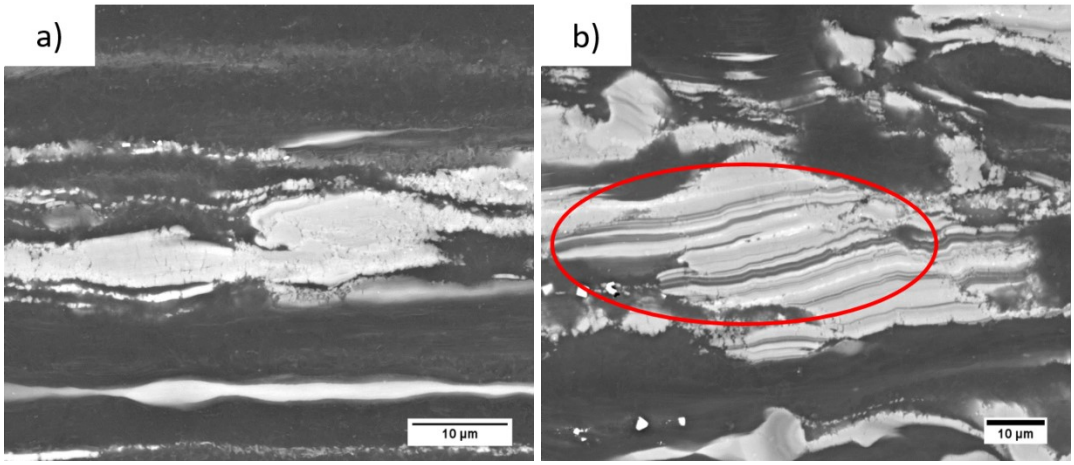

Fig. 4.17. BSE images of the microstructure deformed at RT: a) WZ42, b) WZ104 alloy. The red circle marks the deformation kinks (ED→).

4.2.3. Experimental results: tensile deformation at room temperature

4.2.3.1. Acoustic emission

The time and engineering strain dependences of the applied tensile stress and the concurrent AE activity in the terms of the AE count rate and the amplitude of the raw AE signal for the WZ42 and WZ104 alloys are presented in Fig. 4.18. Both alloys have a characteristic, convex tensile deformation curve. The AE maximum is observed slightly below the macroscopic yield point. After the yielding, both the AE count rate and the AE amplitude are strongly decreased and only a little activity is measured during plastic deformation.

In Fig. 4.19., the time evolution of a) the cumulative number of events and b) the cumulative energy of the WZ42 alloy during tensile testing along ED is presented. In Fig. 4.19.c, two parameters, energy and median frequency, as a result of the ASK, are plotted. The results of the ASK analysis of the tensile deformation of the WZ104 alloy are shown in Fig. 4.20.

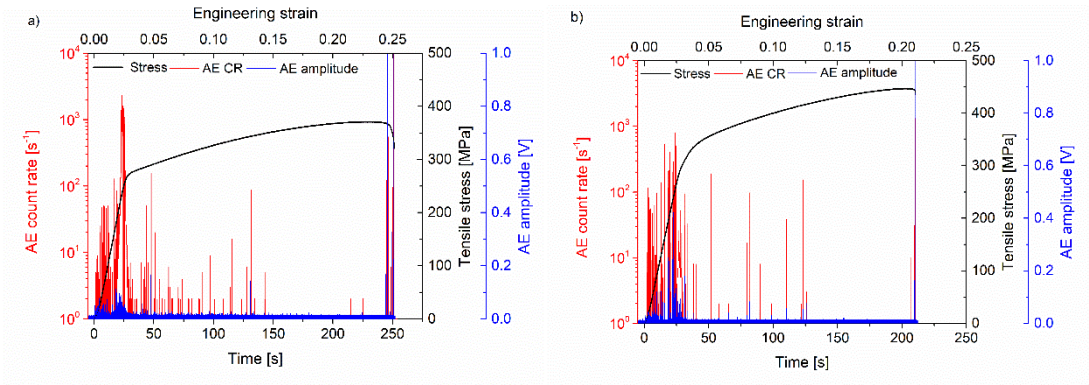

Fig. 4.18. Time and engineering strain dependence of the tensile stress and the corresponding AE response (AE count rate and AE amplitude of the raw signal) of the a) WZ42, and b) WZ104 alloy.

Similar to the assignment performed for AE measured during compression, the first cluster is attributed to the background noise. At the onset of straining, Cluster 2 and Cluster 3 start to increase simultaneously in both alloys. With relative low energies at wide frequency range, Cluster 2 (green) is linked to non-basal slip, while Cluster 3 (red) with slightly higher energy and narrower frequency range is related to basal slip. Shortly before the macroscopic yield point, Cluster 4, associated with twin nucleation, starts to dominate the AE signal. Both, the number of events and their energy of twinning events are lower than that for compressive loading along ED.

In the WZ42 alloy, when twin nucleation is exhausted, the cluster of basal slip starts to increase – both in events and energy. With proceeding plastic deformation, after the number of events of the cluster of basal slip saturates, the cluster of non-basal slip become dominant during the further deformation.

In the WZ104 alloy, the cluster of twinning is also exhausted at the macroscopic yield point, and the beginning of the plastic deformation is controlled by basal and non-basal slip. At higher deformations, a new cluster appears. Even though the relatively small number of events, Cluster 5 (cyan) has quite high cumulative energy. Therefore, because kinking is hard to activate in tension, this cluster is rather connected to the crack initiations.

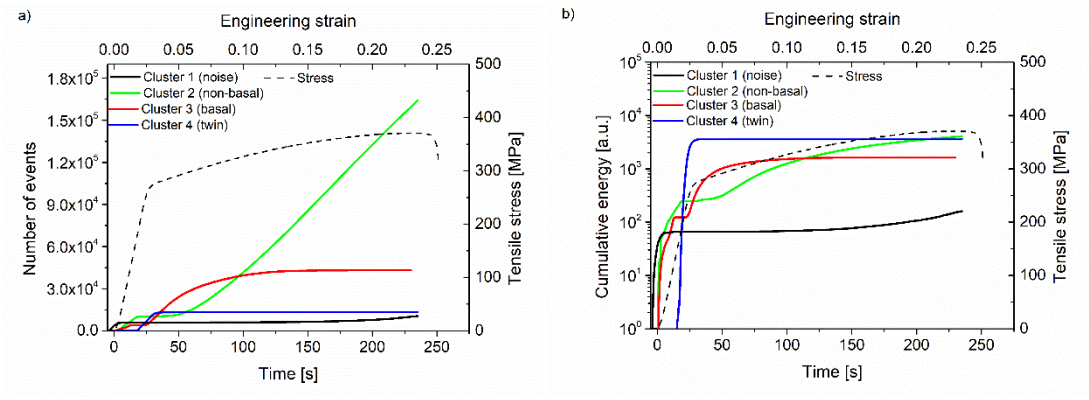

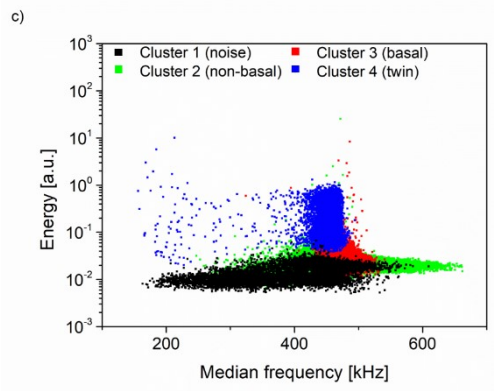

Fig. 4.19. a) The number of events (i.e. the cumulative number of time frames assigned to each cluster) vs. time, b) the cumulative energy vs. time and c) the dependence of energy on the median frequency for the WZ42 alloy during tensile loading along ED.

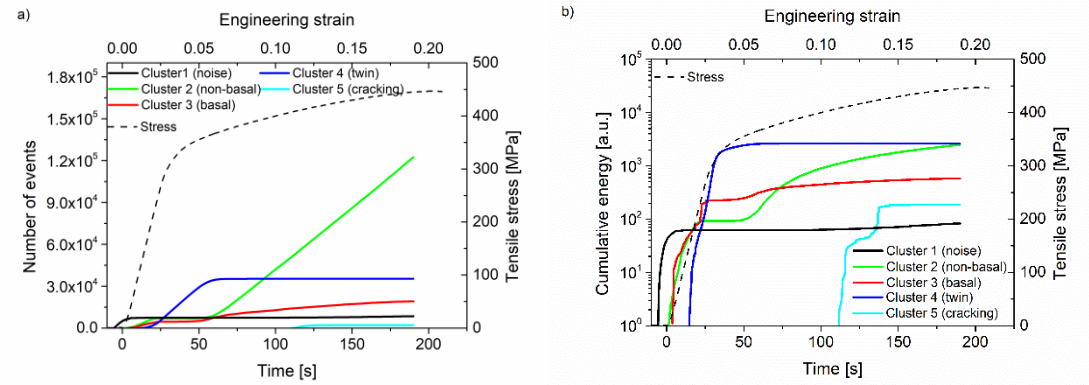

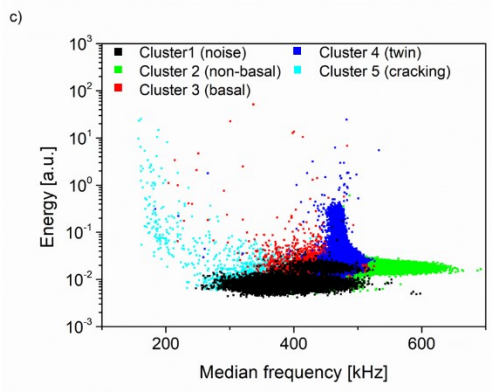

Fig. 4.20. a) The number of events (i.e. the cumulative number of time frames assigned to each cluster) vs. time, b) the cumulative energy vs. time and c) the dependence of energy on the median frequency for the WZ104 alloy during tensile loading along ED.

4.2.3.2. Microscopy

The BSE images taken from the same area prior to and after tensile deformation of the WZ42 and WZ104 alloys are presented in Figs. 4.21. and 4.22., correspondingly. In the deformed WZ42 alloy, some minor cracks, marked by red arrows, are observed in both the Mg matrix and in the LPSO phase. Some slip traces, marked by green arrows, are also present in both the matrix and the LPSO phase. Moreover, grain boundary sliding or rotation is observed in the Mg matrix. Contrary, in the WZ104 alloy, larger cracks are present mainly at the interface of the LPSO phase and the Mg matrix than in the WZ42 alloy. Cracking of the Y-rich particle is also observed in the WZ104 alloy. Although, slip traces are found in both matrix and the LPSO phase, no kinking is detected in either of the tested alloys.

The OIMs, the high angle grain- and twin boundary maps, and texture calculated from the EBSD measurement after the fracture of the WZ42 and WZ104 sample are shown in Figs. 4.23. and 4.24., respectively. In both alloys, narrow $\{10\bar{1}2\}\langle 10\bar{1}1\rangle$ extension twins, reoriented from the mother grain by ≈ 86°, are observed in the recrystallized grains. Moreover, in the WZ42 alloy, the $\{10\bar{1}1\}\langle 10\bar{1}\bar{2}\rangle$ contraction twins reoriented from the mother grain by ≈ 56° are present after the tensile deformation. Some examples of the mother-twin pairs are also shown in Figs. 4.23. and 4.24. Although there are some twins in the microstructure, the texture of the alloys, with basal planes oriented preferentially parallel to ED, is similar to that prior to deformation.

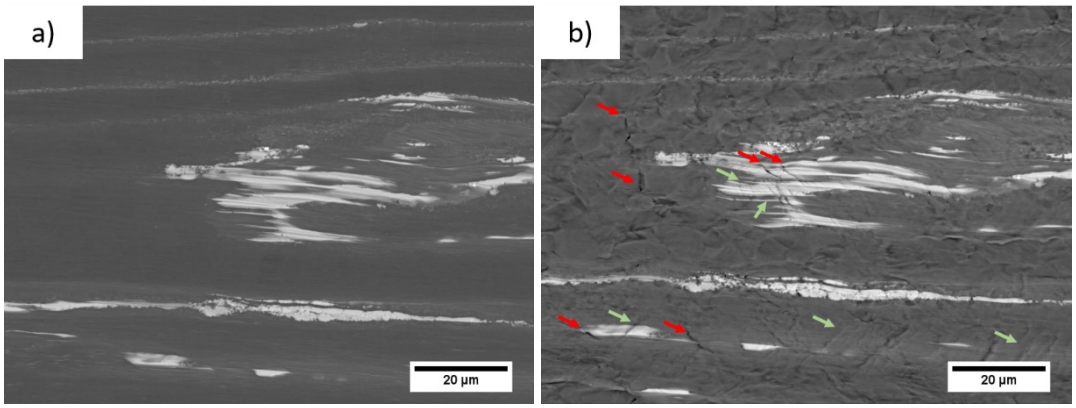

Fig. 4.21. In-situ BSE images of the microstructure of the WZ42 alloy taken a) prior to the deformation and b) after tensile deformation up to fracture (ED→).

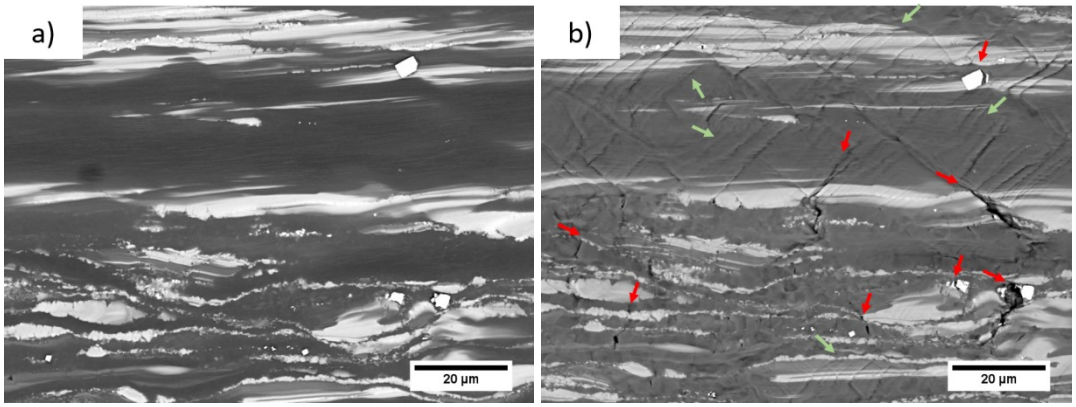

Fig. 4.22. In-situ BSE images of the microstructure of the WZ104 alloy taken a) prior to the deformation and b) after tensile deformation up to fracture (ED→).

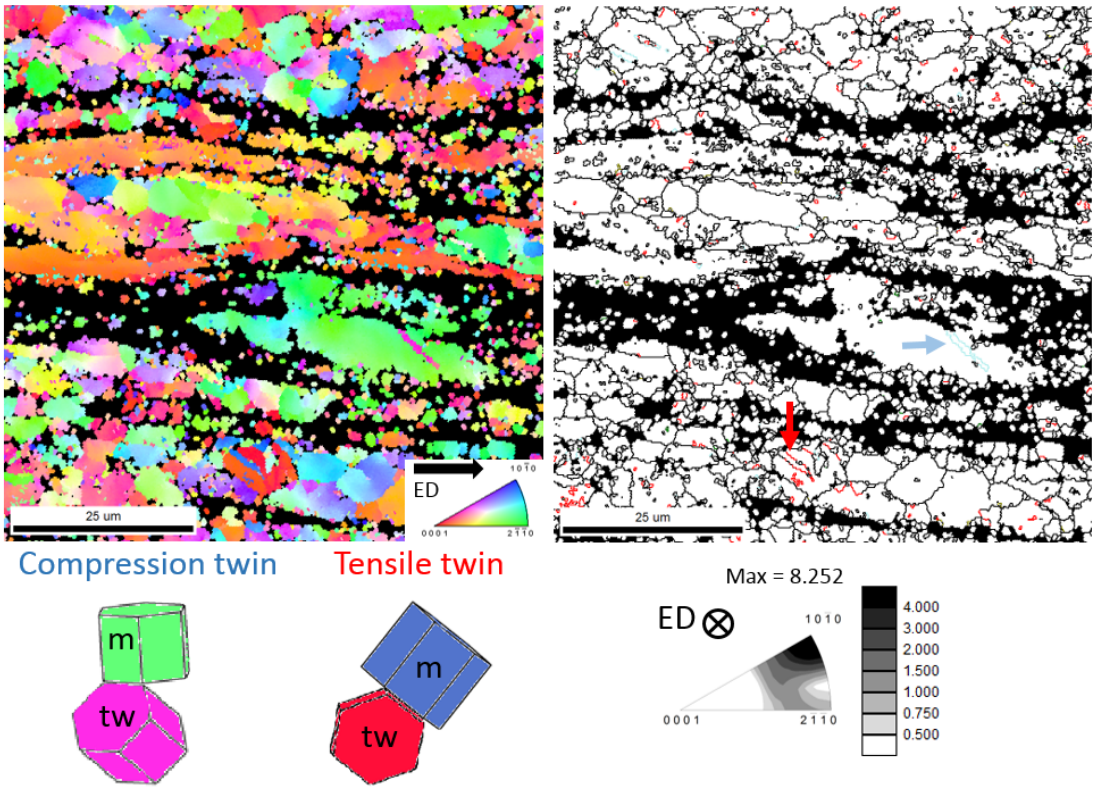

Fig. 4.23. The OIM, the high angle grain- and twin boundaries maps, and calculated texture from the OIM of the WZ42 alloy after tensile deformation up to fracture. The red arrow indicates a tensile twin, while the blue arrow indicates a compression twin.

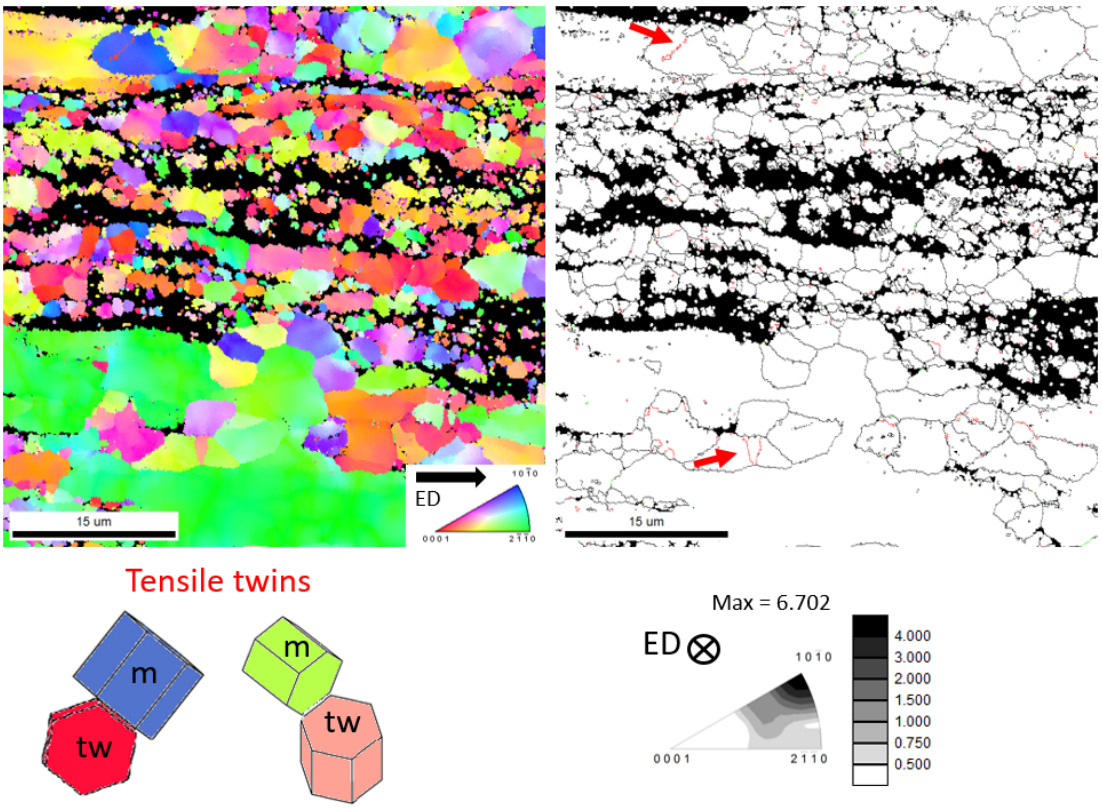

Fig. 4.24. The OIM, the high angle grain- and twin boundaries maps, and calculated texture from the OIM of the WZ104 alloy after tensile deformation up to fracture. Red arrows indicate tensile twins.

4.2.4. Discussion: room temperature deformation and tension-compression yield asymmetry of the Mg-LPSO alloys

Compression

The S-shape of the compression curve, in the case of the WZ42 alloy, is a typical sign of the twin dominated deformation [156, 174–176]. It is well documented that the higher twinning activity results in lower yield strength [169, 177, 178], explaining partly the lower compressive yield strength measured in the WZ42 alloy than that in the WZ104 alloy. Furthermore, it has been reported that the presence of the LPSO phase can inhibit or delay twin formation in the Mg matrix due to the high density of stacking faults enriched with Zn and Y in the basal planes [113, 179–181]. Therefore, the suppressed twinning activity in the WZ104 alloy results in a convex shape of the compressive deformation curve. Moreover, the LPSO phase is known to strengthen the material [5, 13, 179]. Thus, the WZ104 alloy containing a high volume

fraction of the LPSO phase is more likely to obtain higher yield strength comparing to the WZ42 alloy with only 10 % volume fraction of the LPSO phase.

Twin nucleation is an excellent source of AE, generating high amplitude AE signal [120, 127]. From the raw AE signal, presented in Fig. 4.10., it can be assumed that twinning controls the compressive yielding in the WZ42 alloy. On the other hand, twin growth, contrary to their nucleation, is a slow process emitting only low energy wave [121, 123, 182]. Moreover, the newly formed twins are obstacles for moving dislocations as they are reducing the mean free path of their movement and thus the AE signal [58]. These effects may result in significantly lower AE response during the plastic deformation than that observed around the macroscopic yield point.

In the following sections, the results of the ASK analysis are discussed. In both alloys, the deformation starts with the activation of the basal slip, already before the macroscopic yield point, thanks to its low CRSS [33]. Its activation during the elastic regime has been already shown by various authors [8, 33, 183]. In both cases, the cluster of the basal slip contains relatively high energy events in the initial stage of the straining, originated in densely populated dislocation avalanches. With the proceeding deformation, the mean free path for dislocation movement decreases due to the increasing dislocation density. This also causes a decrease in energy and a shift in the median frequency towards higher values.

The cluster of twin nucleation comes up slightly before the macroscopic yield point in both alloys (Figs. 4.11. and 4.12.). The majority of the elements in this cluster have high energy and lie in a narrow frequency range. The nucleation of $\{10\bar{1}2\}\langle 10\bar{1}1\rangle$ extension twins can be assigned to this cluster as they have been found to be active at the beginning of deformation [137, 183] thanks to their low activation stress [33]. Due to the fact that AE is sensitive to the twin nucleation but not to their growth, the combination of AE and diffraction measurements are used to get complimentary dataset about the twinning activity: twin nucleation (AE) and twin growth (diffraction). It has been found by Muránsky et al. [17] that the sudden (0002) peak intensity change correlates with the appearance of burst high energy AE signal. Additionally, they observed that despite the continuous increment of the (0002) peak intensity, the AE RMS voltage (the average power of the AE waveform) decreases above the macroscopic yield point. It has been shown that only weak AE activity is detected during unloading part of cyclic deformation tests when the shrinkage of the

twins is observed in the microstructure, proving the “quietness” of the twin boundary movement [174, 184].

In the WZ42 alloy, the first events in the cluster of twinning are accompanied by high energies. It can be assumed that the twinning takes place in the elongated grains, which are well oriented for the activation of $\{10\bar{1}2\}\langle 10\bar{1}1\rangle$ extension twins. After the yielding, the cluster of twinning continues to grow but the energy of these events is much lower than that before the macroscopic yield point. Moreover, the cluster of basal slip is growing simultaneously. Previously, the grain size dependence of twinning has been documented: twins first occur in larger grains and with increasing stress, they can be activated in the smaller grains [58, 174, 185]. Therefore, the events assigned to the twinning cluster at the later stage of the deformation are very probably those produced by twins in the well oriented recrystallized grains. Because these grains are smaller, compared to the elongated ones, the AE signal generated by nucleation of such tiny twins will be also lower than that in the elongated grains. It has been shown by Vinogradov et al. [56] that the amplitude of the AE signal and the length of the nucleated twin is directly correlated. Therefore, the signal produced by twinning at higher deformations is less pronounced and competition between the cluster related to twinning and other mechanisms (in our case cluster of basal slip) is observed. Extension twinning causes a crystal lattice reorientation by 86.3° around the $\{10\bar{1}2\}$ plane and further plastic deformation can be easily realized by dislocation slip in the reoriented basal planes [186]. This fact can also explain the simultaneous development of clusters related to twinning and basal slip.

Although the re-orientation of basal planes continues, during further loading the basal slip and twinning are not enough to accommodate the strain anymore. Therefore, a new deformation mechanism, the non-basal slip systems are activated. As already mentioned, the ASK algorithm itself cannot distinguish between particular non-basal slip systems. However, based on previous experimental and theoretical calculation [137], the prismatic and pyramidal <a>-slip is likely to contribute to this cluster. The activation of the non-basal slip at higher deformations is also consistent with the fact that CRSS for non-basal slip systems is much higher than that for basal slip [28]. The lower energy of these events can be related to the reduced mean free path for the dislocation movement since they need to overcome dislocation-type obstacles [137].

In the WZ104 alloy, similarly to that in the WZ42 alloy, the cluster of twinning dominates the AE signal before the macroscopic yield point. However, the number of events and their energy is much lower than that in the WZ42 alloy thanks to the increased amount of the LPSO phase present in this material [113, 179–181]. Moreover, if the Mg-LPSO alloy behaves as metal-matrix composite (MMC), the LPSO phase can bear some additional load transferred from Mg matrix [187, 188], which can also reduce the importance of twinning mechanism.

Shortly after the macroscopic yield point, above 360 MPa, the cluster of kinking became dominant. Deformation kinks form when large stress acts parallel to the basal slip planes – which is the case during compression along ED of a material having basal texture. The elastic buckling of the planes is caused by the avalanche-like motion of (0001) basal dislocations [91, 94]. During the ongoing loading, basal dislocations with opposite sign nucleate and they start to move against the dislocations from the first "wave". This results in kink formation. Therefore, the high energy and burst character of kink formation are reasonable, since the highly correlated motion of a large number of dislocation is needed for the process. Its appearance at higher stress levels is in good agreement with the higher Young´s modulus of the LPSO phase, compared to the Mg matrix [70, 189].

Further, the cluster of kinking loses its dominance towards the cluster of the non-basal slip system, which persists up to fracture. The number of events in this cluster for the WZ104 alloy is slightly higher than that for the WZ42 alloy.

The results of the ASK analysis are in a good agreement with the synchrotron diffraction results, Fig. 4.13. Please remember, that the axial diffraction data were analyzed, i.e. the planes perpendicular to the loading axis – ED and the absolute values of the lattice strains are discussed.

In the WZ42 alloy, the lattice strain on the $\{10\bar{1}1\}$ and $\{10\bar{1}2\}$ planes, oriented parallel to the loading direction and having a high Schmid factor for the basal slip [190], lose elastic linearity at the macroscopic yield point, Fig. 4.13. Therefore, it is likely that the macroscopic yielding occurs by the operation of basal <a> dislocation slip. At the same time, the contribution of the prismatic <a> slip cannot be excluded owing to a Schmid factor of 0.34. However, the lattice strain in the (0002) plane loses its elastic linearity already below the macroscopic yield point. Since the Schmid factor for the basal slip is zero for these grains, the deformation is supposed to proceed by

the activation of a non-basal slip or extension twinning. In general, during extension twinning, the reorientation of the lattice by 86.3° leads to an increase in the intensity of the (0002) diffraction peak and the concurrent decrease of the $\{10\bar{1}0\}$ diffraction peak in the axial direction [191]. Therefore, the heavily increased intensity of the (0002) peak indicates a significant role of extension twinning in strain accommodation.

During the plateau regime, major changes are occurring in the lattice strains on all planes thanks to the extension twinning: on the (0002) and $\{10\bar{1}0\}$ planes due to their growth, on the $\{10\bar{1}1\}$, $\{10\bar{1}2\}$ and $\{11\bar{2}0\}$ planes due to the accommodation of the lattice strain generated by twinning [173, 190]. This accommodation leads to the decrease of the $\{10\bar{1}1\}$ and $\{10\bar{1}2\}$ lattice strains and the increase of the $\{11\bar{2}0\}$ lattice strain (Fig. 4.13.a – middle plot).

After the plateau, the lattice strain on the $\{10\bar{1}1\}$ and $\{10\bar{1}2\}$ planes remain almost constant. These grains, i.e. grains which have their $\{10\bar{1}1\}$ and $\{10\bar{1}2\}$ planes perpendicular to ED, are well oriented for the basal <a>-slip. In contrast, the lattice strain on the (0002), $\{10\bar{1}0\}$, and $\{11\bar{2}0\}$ planes increase steadily as the applied stress increases. This behavior of the (0002) planes can be linked to the difficulty of the plastic slip or re-twinning of the already twinned material. The remaining $\{10\bar{1}0\}$ oriented grains have to accumulate a larger portion of strain because the twinning process reorients them out from the position favorable for both basal slip and extension twinning [16, 190]. The grains contributing to $\{11\bar{2}0\}$ diffraction peak has zero Schmid factor for the basal slip. In these grains, the non-basal prismatic slip system can be activated, as it was shown by Agnew et al. [192].

At the later stage of deformation, around 350 MPa, the intensity of the (0002) peak slightly decreases, while the absolute value of the lattice strain continues to increase. This behavior is most likely linked to the rotation of these grains and is caused by the operation of <c+a> slip system [137].

The microscopic observations, Fig. 4.15., support the diffraction and AE results very well. At 2% of plastic strain, extension twins are found not only in the elongated grains but also in the small recrystallized ones, which indicates that twinning plays a key role in the strain accommodation. Although the elongated grains begin to deform before the recrystallized ones, their volume fraction is lower compared to the

recrystallized ones and thus, the macroscopic yielding of the sample is controlled by the basal slip in the recrystallized grains. As it can be seen from the GOS map in Fig. 4.15.b, the elongated grains, i.e. with a high number of twins, store higher deformation than the recrystallized ones.

Contrary to the WZ42 alloy, no micro-yielding is seen in the diffraction data collected for the WZ104 alloy. At the macroscopic yield point, the grains with their $\{10\bar{1}1\}$ and $\{10\bar{1}2\}$ planes oriented parallel to the ED start to deform by basal slip, similarly to those in the WZ42 alloy. At the same time, the (0002) - $\{10\bar{1}0\}$ conjugated planes also start to deviate from the elastic response due to the activation of the extension twin system, as in the WZ42 alloy. However, the change in the intensity of the (0002) peak is much lower than that in the WZ42 alloy. During the strain hardening regime of the alloy, the lattice strain on the $\{10\bar{1}1\}$ plane is nearly constant, comparable to that in the WZ42 alloy. In this part of the deformation, as the result of the extension twinning, in the (0002) - and $\{10\bar{1}0\}$ planes the further twinning and the slip deformation is rather difficult, and therefore their lattice strains increase till the end of the deformation. Alike the $\{11\bar{2}0\}$ planes, which lattice strain increases with a slope higher than in the WZ42 alloy, indicating on the activity of non-basal slip systems. Analogous information is presented from the ASK clustering, indicating a higher number of non-basal events in the WZ104 alloy than in the WZ42 alloy.

At the end of the deformation, the elongated grains are re-oriented by 86° compared to the initial orientation due to extension twinning (Fig. 4.16.b). However, in WZ104 alloys, some initially oriented big grains (color-coded as red) even after the fracture of the alloy can be found, while in the WZ42 alloy, all the elongated grains are reoriented by twinning (Fig. 4.15.b). Thus, it clearly shows that the twinning is suppressed in the WZ104 alloy. It is also in a good agreement with the results obtained from the *in-situ* methods: the lower number of events in the cluster of twinning and the lower change of the intensity of the (0002) diffraction peak is observed in the WZ104 alloy comparing to the WZ42 alloy.

Since the intensity of the LSPO diffraction peak in the WZ42 alloy is too weak for fitting, no information about their deformation from the diffraction data can be evaluated. It is shown by the post-mortem BSE images that in the WZ42 alloy the kinking is not activated. Contrary, in the WZ104 alloy, the higher volume fraction of

the LPSO phase allowed to fit the $\{10\bar{1}8\}$ diffraction peak for the LPSO phase. The heavy increase of the lattice strain on the $\{10\bar{1}8\}$ plain of the LPSO phase after the macroscopic yield strength suggests that it bears a higher load compared to the Mg matrix. However, its evolution after 400 MPa is not reliable since the (0002) Mg diffraction peak is very intensive due to the twinning and it overlaps with the LPSO peak. Similar results have been reported elsewhere [8, 12, 193].

The microstructure of the WZ104 alloy is intensively kinked at the end of the compressive deformation. Therefore, it seems that the higher volume fraction of the LPSO phase increases the amount of load transferred from the Mg matrix to the LPSO phase and increases the plasticity of the LPSO phase.

Tension

Both studied alloys have a convex shaped tensile deformation curve, typical for the polycrystalline materials. The WZ104 alloy is characterized by higher tensile yield strength (TYS) and lower elongation to failure compared to the WZ42 alloy. It has been suggested by Yamasaki et al. [4] that the fine recrystallized Mg grains highly contribute to the ductility, while the LPSO phase contributes to the yield strength of the Mg-LPSO alloys. On the other hand, it is shown in [113] that the interface between the LPSO fibers and the Mg matrix concentrates stresses and enhances the formation of cracks. The WZ104 alloy, with a high volume fraction of the LPSO phase, is expected to generate a larger number of cracks (what is in agreement with observations in Fig. 4.22.), and, consequently, results in a lower tensile elongation to failure.

Oñorbe et al. [193] have shown using synchrotron diffraction measurements that during tensile tests, the Mg grains are transferring part of their load to the LPSO phase, especially between 250 and 350 MPa. They related this effect to the higher Young´s modulus of the LPSO phase (75 GPa) than that of the Mg matrix (48 GPa). They also concluded that the load transfer capacity of the LPSO phase decreases above 350 MPa. These findings support our results obtained by BSE imaging of samples deformed to higher stresses, where more cracks perpendicular to the loading direction are observed in the WZ104 alloy than that in the WZ42 alloy (Fig. 4.21. and 4.22.).

During tensile tests, the maximum of the AE response around the macroscopic yield point is usually explained by the massive multiplication of dislocations, whereby

various slip systems can be activated [120]. Generally, in Mg alloys at RT deformation, the basal slip, owing to the lowest CRSS in comparison with other slip systems, is the easiest activated slip system [194]. However, in the elongated grains, with basal planes oriented parallel to the loading directions, the Schmidt factor for the basal slip is zero. Therefore, the simultaneous activation of basal and non-basal slip systems revealed by the ASK analysis is reasonable (Fig. 4.19. and 4.20.). Shortly before the macroscopic yield point, the cluster of twinning dominates the signal in both alloys. Some papers suggested that extension twins can be nucleated during tensile tests in the grains with their basal planes oriented perpendicular to the loading axis [170, 178, 195, 196]. However, their number is limited due to the presence of the initial texture in investigated alloys. The existence of twins in the samples deformed in tension is confirmed by OIM maps in Figs. 4.23. and 4.24. for the WZ42 and WZ104 alloys, respectively. In both alloys, relatively narrow twins are observed in the microstructure at the end of the deformation. Moreover, in the WZ42 alloy, some $\{10\bar{1}1\}\langle 11\bar{2}0\rangle$ contraction twins, reorienting the crystal lattice by 56° are formed [197, 198]. This type of contraction twins is expected to nucleate when tension is applied perpendicular to the c-axis of the grain. Although more grains are favorably oriented for nucleation of contraction twins, their appearance is very limited. It can be explained by the higher stress required for their nucleation, which could reach 76 – 153 MPa [199], compared to that of the extension twinning about 2-12 MPa [33, 42, 57]. Furthermore, contraction twins do not expand over the grain, contrary to the extension twins [198].

As a result of the contraction twinning, the basal planes are rotated by 56° what is favorable for the activation of the basal slip owing to high Schmid factor [198]. However, there is only limited accessibility for the basal slip, therefore the non-basal slip dominates the AE signal till the end of the deformation in both of the alloys (Figs. 4.19. and 4.20.).

In the WZ104 alloy, at the later stage of the plastic deformation, a new cluster with relatively high energy is formed (Fig. 4.20.). Due to the strong basal texture of the LPSO phase in this extruded alloy, the formation of deformation kinks is restricted during tensile loading [91]. Therefore, this cluster has been rather linked to the crack initiation in the sample. As it is written above, the interface between the LPSO fibers and the Mg matrix concentrates stresses and enhances the formation of cracks [113]. It is in good agreement with the microscopic result: the WZ104 alloy presents a

significantly larger amount of cracks compared to the WZ42 alloy, as can be seen in Figs. 4.21. and 4.22.

Tension-compression yield asymmetry

The tension-compression yield asymmetry is one of the key problems in the wrought Mg alloy. This phenomenon is related to the activation of different deformation mechanism in tension than in compression due to the orientation of the *hcp* lattice and a strong texture formed during the extrusion process. Particularly the polar nature of twinning, i.e. its easy activation during compressive loading perpendicular to the *c*-axis, causes a higher yield strength in tension than in compression, commonly observed in extruded Mg alloy. However, the investigated Mg-LPSO alloys exhibit a different yield asymmetry behavior. The WZ42 alloy behaves like the "typical" extruded Mg alloys, having higher yield strength in tension than that in compression. Contrary, WZ104 shows reverse yield asymmetry, i.e. it has a higher yield stress in compression than in tension. It should be noted that the Mg alloy with a volume fraction of the LPSO phase around 85% has higher yield strength in compression than that in tension [113].

There are several theories proposed for explaining the inverse tension-compression asymmetry of Mg-LPSO alloys:

(i) These alloys can be interpreted as MMCs reinforced by ceramic particles. The yield asymmetry of the MMCs is related to the residual stresses developed in the material during processing [200]. Thanks to the differences in the thermal expansion coefficients between the metal and ceramic, which can be as high as one order of magnitude, during the cooling steps tensile residual stress is induced into the metal matrix and compressive residual stress is induced into the ceramic phase. The presence of the residual stresses has been found experimentally in an extruded MMC [187]. Similarly, the Mg-LPSO alloys could be understood as „*in-situ*" composites and the yield strength asymmetry could be explained by the residual stresses as well. However, it has been confirmed that the thermal expansion coefficient of the LPSO phase is similar to that of the Mg matrix [201]. Therefore, residual stresses formed in the LPSO phase and Mg matrix should not be of polar difference (i.e. compression/tension component). Thus, processes

happened in MMCs cannot completely explain the tension-compression yield asymmetry of the Mg-LPSO alloys.

(ii) Since tension-compression yield asymmetry is related to the twinning activity, suppression of twinning affects the yielding behavior. It has been shown by Matsuda et al. [180] that deformation twins are deflected or arrested in the region next to the LPSO phase. Thus, a sufficiently large volume fraction of the LPSO phase is expected to prevent twinning. However, as seen from the results presented in this work, although the amount of twins is less in the WZ104 alloy than in the WZ42 alloy, they still play a significant role during compression. As deformation twinning, i.e. the type of the deformation mechanism itself cannot explain the reversed yield asymmetry, a third possibility should be considered.

(iii) Due to the rather complex microstructure, the reverse asymmetry may be related to the changes in the contribution to the overall yield strength by each individual microstructural parameter, i.e. the contribution of the LPSO phase, recrystallized and elongated non-recrystallized Mg grains. As discussed by Garcés et al. [202], the yield strength ($\sigma_{0.2}$) of an Mg-LPSO alloy, considered as a composite material, can be estimated as:

$$\sigma_{0.2} = f_{LPSO}\sigma_{LPSO} + f_{DRX}\sigma_{DRX} + f_{non-DRX}\sigma_{non-DRX}, \qquad (4.1)$$

where f is the volume fraction, and the σ is the stress carried by each microstructure component. The volume fractions are summarized in Table 4.1. The tension and compression yield strength of the 18R type LPSO phase (σ_{LPSO}) was determined from Fig. 4 in [113] as 417 and 481 MPa, respectively. The relationship between the yield strength contribution of the recrystallized grains (σ_{DRX}) and the intrinsic stress (σ_0) of the Mg matrix can be described using the Hall-Petch equation, related to the size of the recrystallized grains as:

$$\sigma_{DRX} = \sigma_0 + k_{HP}\frac{1}{\sqrt{d_{DRX}}}, \qquad (4.2)$$

where k_{HP} is the strenghtening coefficient and d_{DRX} is the grain size of the recrystallized grains, see Table 4.2. Values of $\sigma_0 = 49\,MPa$ and $k_{HP} = 188 MPa\mu m^{-1/2}$ have been determined by Hagihara et al. [13] in an extruded $MgZn_1Y_2$ alloy. The contribution of the recrystallized grains is independent of the sense of the stress - tension or compression – due to the small grain size, and it increases with the decrease of the grain size.

The term $\sigma_{non-DRX}$ also contains two main contributors: the intrinsic stress σ_0 of the Mg matrix and σ_T related to the strong texture of the elongated grains. Then equation (4.1.) can be rewritten as:

$$\sigma_{0.2} = f_{LPSO}\sigma_{LPSO} + f_{DRX}\left(\sigma_0 + k_{HP}\frac{1}{\sqrt{d_{DRX}}}\right) + f_{non-DRX}(\sigma_0 + \sigma_T). \quad (4.3)$$

The contribution of the elongated non-recrystallized grains is obtained by subtracting the contributions of the LPSO phase and the recrystallized grains from the experimental yield strength (Table 4.2.), as:

$$f_{non-DRX}(\sigma_0 + \sigma_T) = \sigma_{0.2} - f_{LPSO}\sigma_{LPSO} - f_{DRX}\left(\sigma_0 + k_{HP}\frac{1}{\sqrt{d_{DRX}}}\right). \quad (4.4)$$

The calculated contributions to the yield strength during tension and compression in MPa and percentages are summarized in Table 4.3. and shown in Fig. 4.25., respectively.

Table 4.3. Strengthening contributions to the yield strength from the LPSO phase, recrystallized and elongated Mg grains

[MPa]	**LPSO phase**		**Elongated grains**		**Recrystallized grains**
	Tension	Compression	Tension	Compression	
WZ42	42	48	117	94	106
WZ104	133	154	78	91	87

The yield strength contribution of the LPSO phase is higher in compression than in tension and it increases linearly with its volume fraction. The contribution of the recrystallized grains to the yield strength is independent on the loading mode and depends mainly on the grains size. Although there is no big difference in the size of the recrystallized grains in the two alloys, their volume fraction is higher in the WZ42 alloy than that in the WZ104 alloy. This results in the higher yield strength contribution of the recrystallized grains in the WZ42 alloy than in the WZ104 alloy.

In the WZ42 alloy, with the lower volume fraction (10%) of the LPSO phase, the yield strength contribution of the elongated worked grains (depicted as non-DRX in Fig. 4.25) is lower in compression than in tension. It can be explained as these grains are favorably oriented for extension twinning in compression but not in tension. It is in good agreement with the AE and diffraction results, which show that during compression, extension twinning is already activated before the macroscopic yield

point. Therefore, the contribution of these grains to the yield strength is lower than that of the recrystallized ones.

Contrary, in the WZ104 alloy, containing 32% volume fraction of the LPSO phase, the contribution of the worked grains to the yield strength is slightly higher in compression than in tension, what is in contrast to the yield behavior of the WZ42 alloy. Furthermore, no micro-yielding caused by the activation of the extension twins is observed, and therefore the macroscopic yielding is controlled by the activation of the basal slip in the recrystallized grains. Consequently, the yield strength contribution of the recrystallized grains is higher in tension and only slightly smaller in compression compared to that of the elongated, non-recrystallized grains.

It appears that the yield strength is very sensitive to the volume fraction of the recrystallized and elongated worked grains. In a material with the very high volume fraction of the recrystallized grains, in which the yielding is mainly controlled by the basal slip in both compression and tension, the respective yield strength should be equal. However, the strong anisotropy of the LPSO phase can invert the yield strength asymmetry what leads to higher stresses in compression than in tension. It has been reported by Garcés et al. [113] that reverse yield strength asymmetry can be achieved in alloys with at least 15 % volume fraction of the LPSO phase.

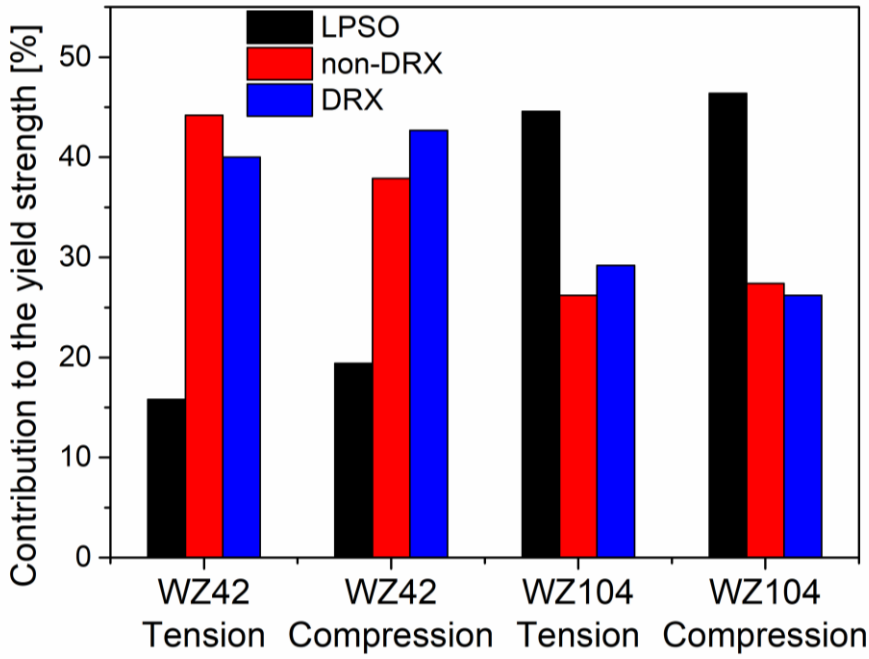

Fig. 4.25. The strengthening contributions to the yield strength from different microstructural parameters.

4.3. Deformation behavior of the Mg-LPSO alloys at elevated temperatures

In extruded Mg alloys, the preferential activation of twinning during compression along ED causes inferior mechanical properties in compression comparing to those in tension. Therefore, the compressive deformation behavior at elevated temperatures of both Mg-LPSO alloys is studied in detail, particularly with respect to the twinning activity.

4.3.1. Experimental results: compressive deformation at elevated temperatures

The true stress *vs*. true strain deformation curves measured during compression along ED at RT, 200 °C, 300 °C, and 350 °C for the WZ42 and WZ104 alloys are shown in Fig. 4.26. The values of obtained yield strengths are summarized in Table 4.4. With increasing deformation temperature, the yield strengths decrease and the shapes of the deformation curves are changed.

At 200 °C, the WZ42 alloy undergoes significant strain hardening resulting in a concave, so-called S-shaped, deformation curve, similar to that measured at RT. The sample deformed at 300 °C shows some hardening up to 15 % of strain, but it is less significant than that at 200 °C. At 350 °C, after reaching the yield point, a dynamic softening is observed.

In the case of the WZ104 alloy, the compression curve at 200 °C has a convex shape, different from the one observed at RT. The drop in the yield strength between RT and 200 °C is much less than that observed between 200 °C and 300 °C. During deformation at 300 °C and 350 °C, significant softening occurs after reaching the yield point.

Comparing the two investigated alloys, the yield strength of the WZ104 alloy is significantly higher at RT and 200 °C than that for the WZ42 alloy. However, the difference in the yield strengths at 300 °C is negligible. At 350 °C, the WZ42 alloy has slightly higher compressive yield strength than that in the WZ104 alloy.

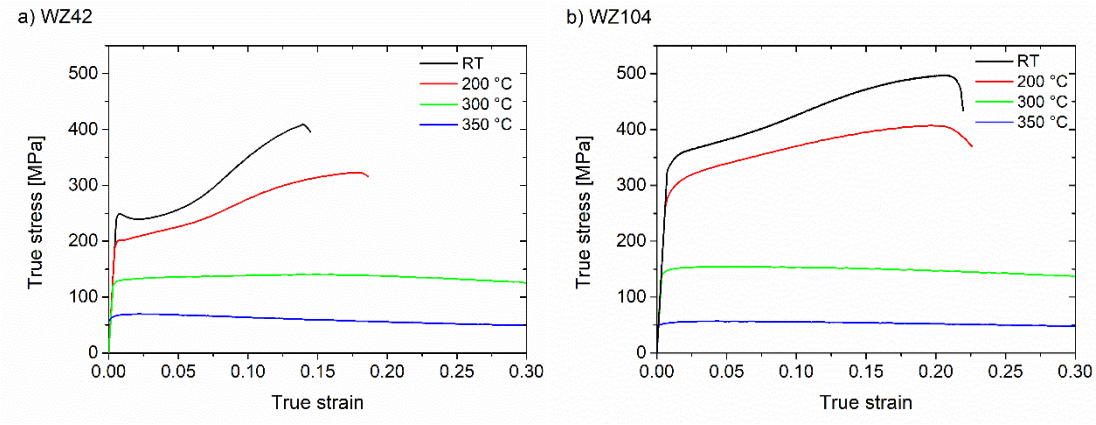

Fig. 4.26. True strain vs. true stress compression curves of the a) WZ42 and b) WZ104 alloy deformed at RT, 200 °C, 300 °C, and 350 °C along the ED.

Table 4.4. The yield strengths measured at RT, 200 °C, 300 °C, and 350 °C in compression along ED of the WZ42 and WZ104 alloys

	Yield strength [MPa]			
	RT	200 °C	300 °C	350 °C
WZ42	248 ± 2	196 ± 2	130 ± 2	69 ± 2
WZ104	332 ± 3	285 ± 3	139 ± 3	49 ± 3

4.3.1.1. Synchrotron diffraction

The results of the compression tests of the WZ42 alloy at 200 °C, 300 °C, and 350 °C with the concurrent synchrotron diffraction measurements are shown in Fig. 4.27. Particularly, the compressive deformation curves, the stress dependence of the lattice strains and change in the intensities for the (0002) and $\{10\bar{1}0\}$ diffraction peaks in the axial direction as a function of the applied stress are presented.

During the compression of the WZ42 alloy at 200 °C, the lattice strain on the $\{10\bar{1}1\}$- and $\{10\bar{1}2\}$ planes lose their elastic linearity between 175 and 200 MPa. In the case of the (0002) peak, no deviation from the linearity is observed up to stresses slightly lower than the yield strength. During plastic deformation, its intensity significantly increases. Further, at the later stage of deformation, above 275 MPa, the intensity of the (0002) peak slightly decreases. In general, the behavior of the (0002) peak is different from that observed at RT, Fig. 4.13, discussed in Section 4.24.

At 300 °C, the lattice strain on the $\{10\bar{1}0\}$-(0002) conjugated planes deviate from the ideal elastic response virtually in the macroscopically elastic deformation range. The absolute value of the (0002) lattice strain increases until the strain of 15%. Until this point, a pronounced strain hardening of the alloy is observed. Afterward, softening takes place and the lattice strain on the (0002) plain starts to slightly decrease. The intensity of the (0002) diffraction peak starts to increase after the yield point and continues with this behavior until the hardening of the alloy persists. Similarly to the lattice strain, during the softening, the intensity of the (0002) peak decreases. The lattice strains on the $\{10\bar{1}1\}$, $\{10\bar{1}2\}$, and $\{11\bar{2}0\}$ planes are nearly constant during the plastic deformation.

At 350 °C, after reaching the yield point, the alloy undergoes significant softening and the value of the $\{10\bar{1}0\}$ lattice strain decreases. Only the (0002) and $\{11\bar{2}0\}$ lattice strains show a slight increase. The intensity of the (0002) diffraction peak is nearly constant during the entire deformation test, while the intensity of the $\{10\bar{1}0\}$ diffraction peak decreases after reaching the yield point.

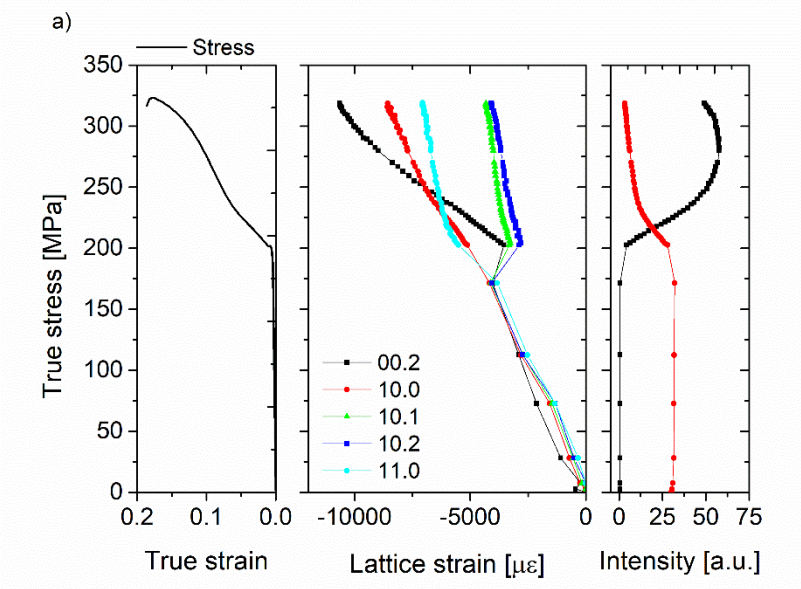

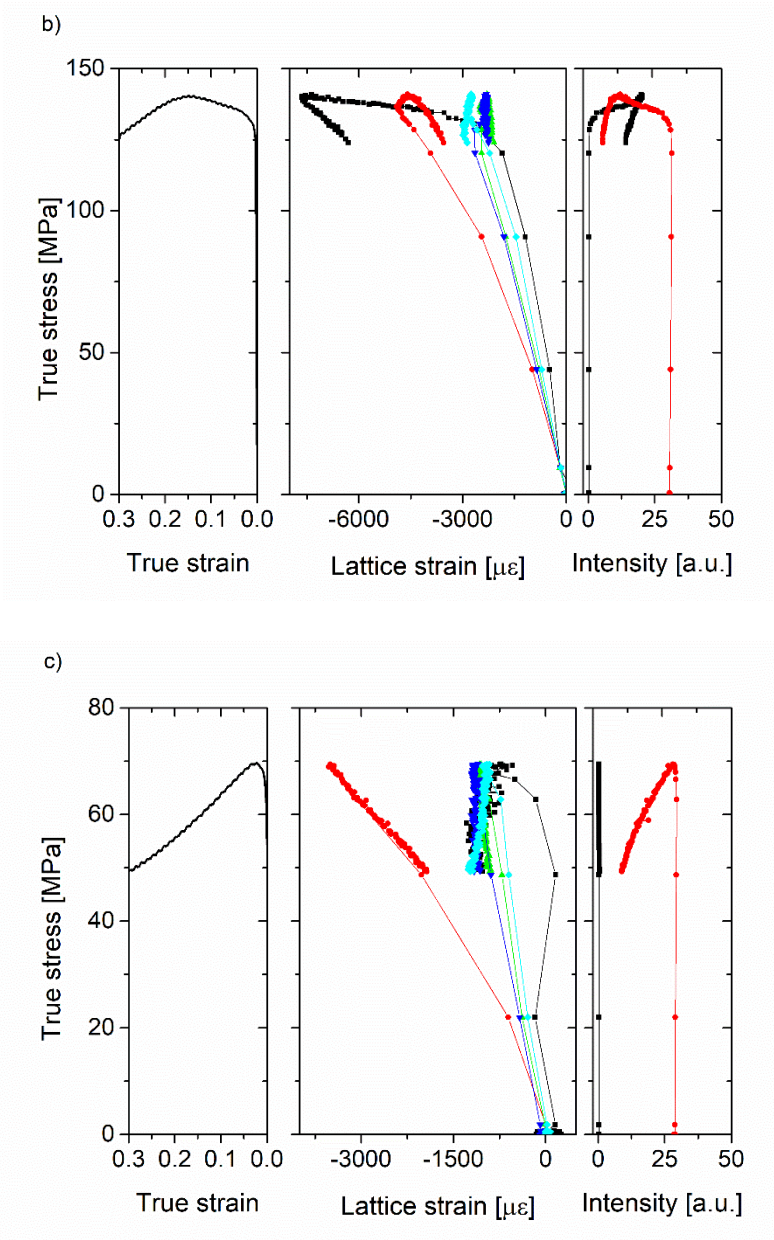

Fig. 4.27. Macroscopic stress-strain curves, the axial lattice strains as a function of the applied stress and evolution of the intensity of the major diffracted peaks of the Mg matrix during the compression test of the WZ42 alloy at a) 200 °C, b) 300 °C, and c) 350 °C.

The compressive deformation curves, the evolution of the lattice strain on the major Mg planes and on the $\{10\bar{1}8\}$ LPSO plane and change of the intensities for the (0002) and $\{10\bar{1}0\}$ peaks in the axial direction as a function of the applied stress measured in the WZ104 alloy are shown in Fig. 4.28. a-c for 200 °C, 300 °C, and 350 °C, respectively.

At 200 °C, the development of the lattice strains on the $\{10\bar{1}1\}$ and $\{10\bar{1}2\}$ planes are comparable to that at RT, Fig. 4.13.b, discussed in Section 4.2.4. The lattice strain on the $\{11\bar{2}0\}$, $\{10\bar{1}0\}$, and (0002) Mg planes deviate from the elastic linear response between 275 and 290 MPa. The absolute value of their lattice strains starts to increase at the macroscopic yield point. On the $\{11\bar{2}0\}$ and $\{10\bar{1}0\}$ planes it continues to increase till the end of the deformation with a slope slightly higher than that in the elastic regime. Contrary, the lattice strain on the (0002) peak increases till 308 MPa than decreases up to 326 MPa and afterward increases till the end of the deformation. The lattice strain on the $\{10\bar{1}8\}$ LPSO plane starts to deviate from the elastic response at the macroscopic yield point together with the Mg planes. Its lattice strain increases till 315 MPa and remains nearly constant during the rest of the deformation.

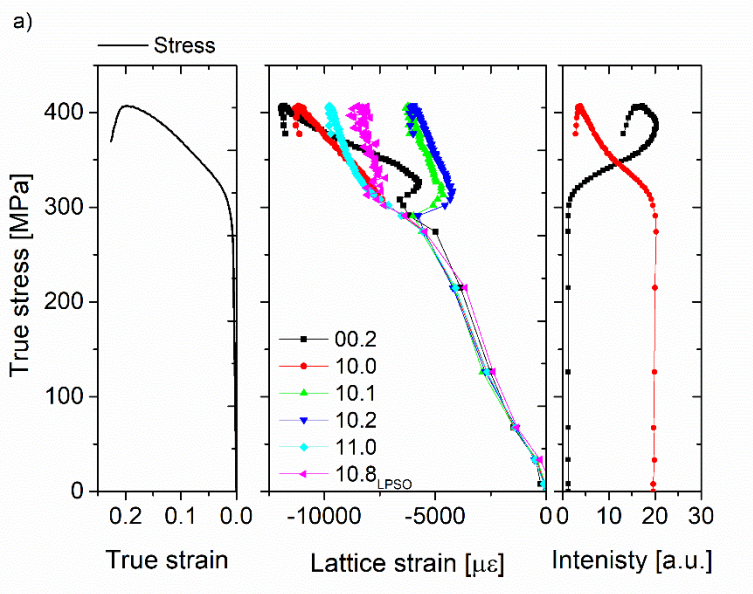

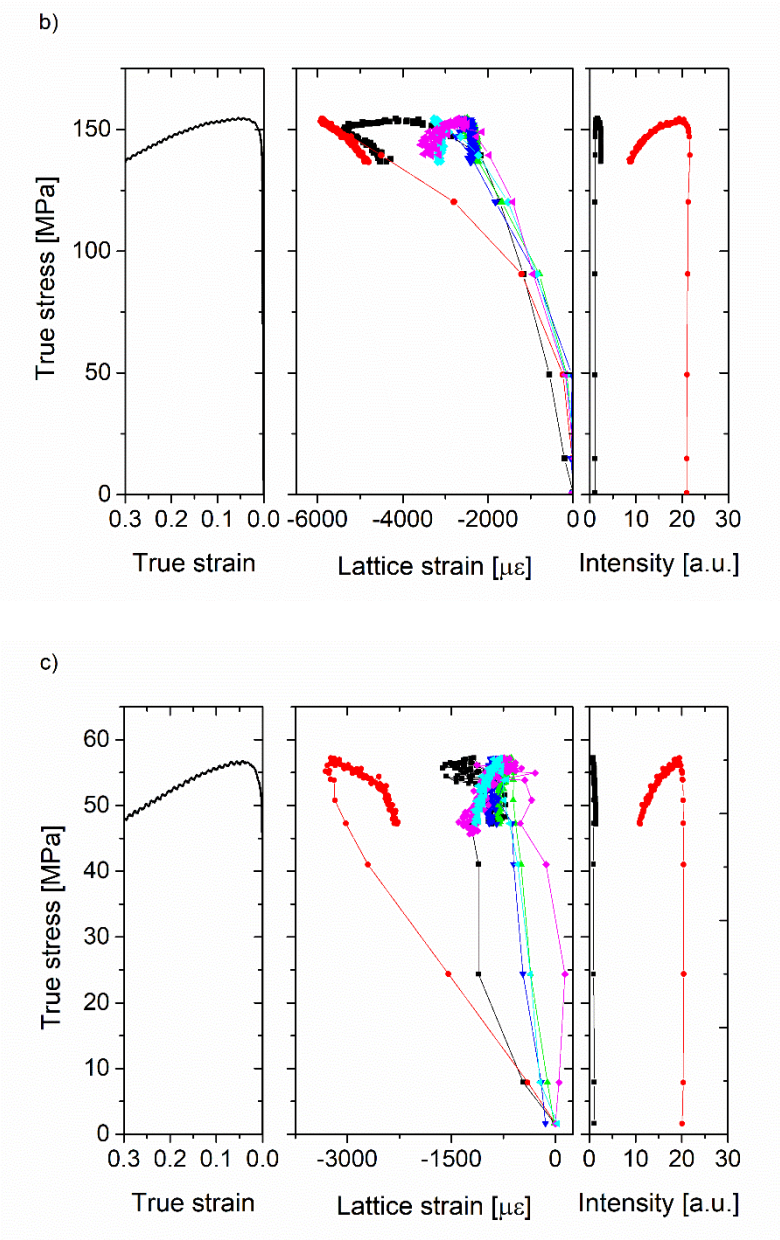

Fig. 4.28. Macroscopic stress-strain curves, the axial lattice strains as a function of the applied stress and evolution of the intensity of the major diffracted peaks of the Mg matrix and LPSO phase during the compression test of the WZ104 alloy at a) 200 °C, b) 300 °C, and c) 350 °C.

At 300 °C, the lattice strains on the $\{10\bar{1}0\}$ and (0002) planes increase up to 150 MPa (12.5 % of deformation) and significantly decreases with further deformation. In contrast, the value of the lattice strain on the $\{11\bar{2}0\}$ plane slightly increases during plastic deformation. There is no significant change in the lattice strain on the $\{10\bar{1}1\}$ and $\{10\bar{1}2\}$ planes. The $\{10\bar{1}8\}$ LPSO plane behaves similarly to the

$\{11\bar{2}0\}$ plane of Mg matrix. The intensity of the (0002) peak is practically constant during the entire deformation while that of the $\{10\bar{1}0\}$ peak is decreasing with increasing deformation.

The lattice strain on the $\{10\bar{1}0\}$ planes decreases and on the $\{11\bar{2}0\}$ plane slightly increases during the plastic deformation at 350 °C. The lattice strains on the other presented planes are nearly constant during the entire deformation. Similarly to that at 300 °C, the intensity of the (0002) peak is constant during the entire deformation while that of the $\{10\bar{1}0\}$ peak is decreasing with increasing deformation.

The axial distribution function of the (0002) diffraction peak before the deformation (in the as-extruded state) and at the end of the deformation as a function of temperature is presented in Fig. 4.29.a,b for the WZ42 and WZ104 alloy, respectively. As it is described previously in section 4.2.2.2., in the initial state, the intensity of the (0002) peak is concentrated at 90° for both alloys. At 200°C, as well as during RT deformation, with the ongoing deformation of alloys, the intensity at 90° decreases and concentrates at 5° (loading direction). A similar tendency is observed at 300 °C for the WZ42 alloy, but the change in the intensity is much smaller, compared to tests at lower temperatures. Moreover, a local maximum around 40° is formed. The evolution of the (0002) diffraction peak during deformation at 350 °C in the WZ42 alloy is completely different from the previous cases. The intensity in the axial direction does not increase, and intensity in the radial direction decrease in expense of more steady distribution of the intensity within 20-90° range. Contrary, at 300 °C and 350 °C in the WZ104 alloy no significant change in the distribution of the intensity of the (0002) peak is observed.

The calculated TVFs are plotted in Fig. 4.29. c and d for the WZ42 and WZ104 alloy, correspondingly. The determination of the TVF is described in section 4.2.2.2. The calculated TVF of the Mg matrix at RT deformation is 53%, at 200 °C – 39%, and at 300 °C – 22% for the WZ42 alloy; and for the WZ104 alloy deformed at RT and 200 °C - 31 % and 25%, respectively. The TVF during deformation at 300°C and 350 °C of the WZ104 alloy and at 350 °C of the WZ42 alloy cannot be calculated since there is no sign in the intensity change for the $\{10\bar{1}0\}$-(0002) conjugated planes related to the extension twinning. Thus the calculation of the TVF with this method is well applied at RT and 200 °C, but it is limited at higher temperatures. The additional local maximum at 40°, observed in the WZ42 alloy deformed at 300 °C, is supposed

to be the result of another mechanism, which will be discussed later. Therefore, the calculated TVF is rather the upper limit of the real TVF. It is important to keep in the mind, that the TVF is calculated in the Mg matrix, and therefore its value is related to the volume of the Mg matrix only, not to the entire sample.

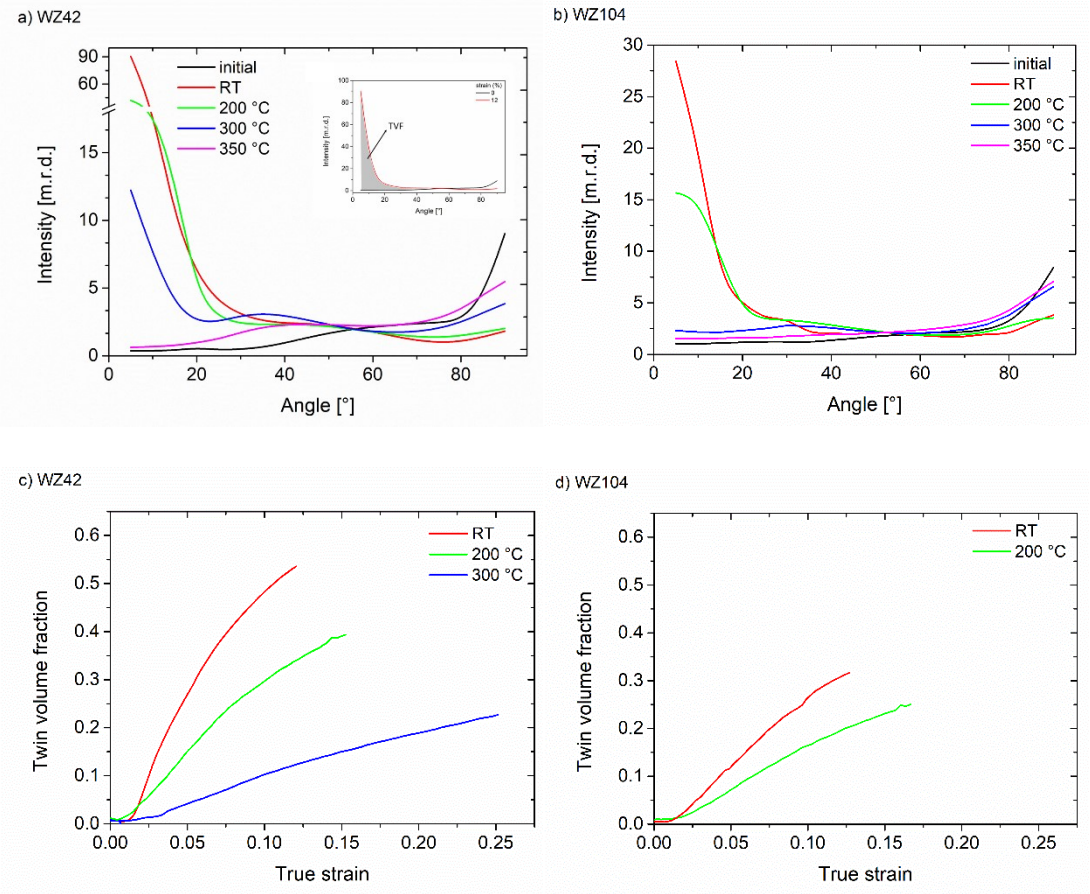

Fig 4.29. Axial distribution function variation for the (0002) *pole in the as-extruded (initial) state and after compression at RT, 200 °C, 300 °C, and 350 °C for a) WZ42 and b) WZ104 alloy; the calculated TVFs for experiments a) at RT, 200 °C, and 300 °C for the WZ42 alloy and d) at RT and 200 °C for the WZ104 alloy.*

4.3.1.2. Microscopy

To get more information on the orientation changes of the Mg matrix and the deformation of the LPSO phase, EBSD technique and BSE imaging were additionally applied. The microstructures of the WZ42 alloy deformed up to 2% of plastic strain at 200 °C, 300 °C, and 350 °C are shown in Fig. 4.30.a-c, respectively. In the sample deformed at 200°C, a lot of narrow twins can be observed, not only in the elongated

grains but also in the recrystallized grains well oriented for the activation of extension twins during compression along ED. The boundaries of the $\{10\bar{1}2\}$ extension twins are plotted in red in Fig. 4.30. The activity of this twin system is also obvious from the calculated IPF (lower right corner of Fig. 4.30.a), where an intensity at the (0001) pole is formed. In the sample, deformed at 300 °C up to 2% of plastic strain, the texture component at the (0001) pole corresponds to twins observed only in the elongated grains, see Fig. 4.30.b. At 350 °C, no twins are observed in the microstructure (Fig. 4.30.c).

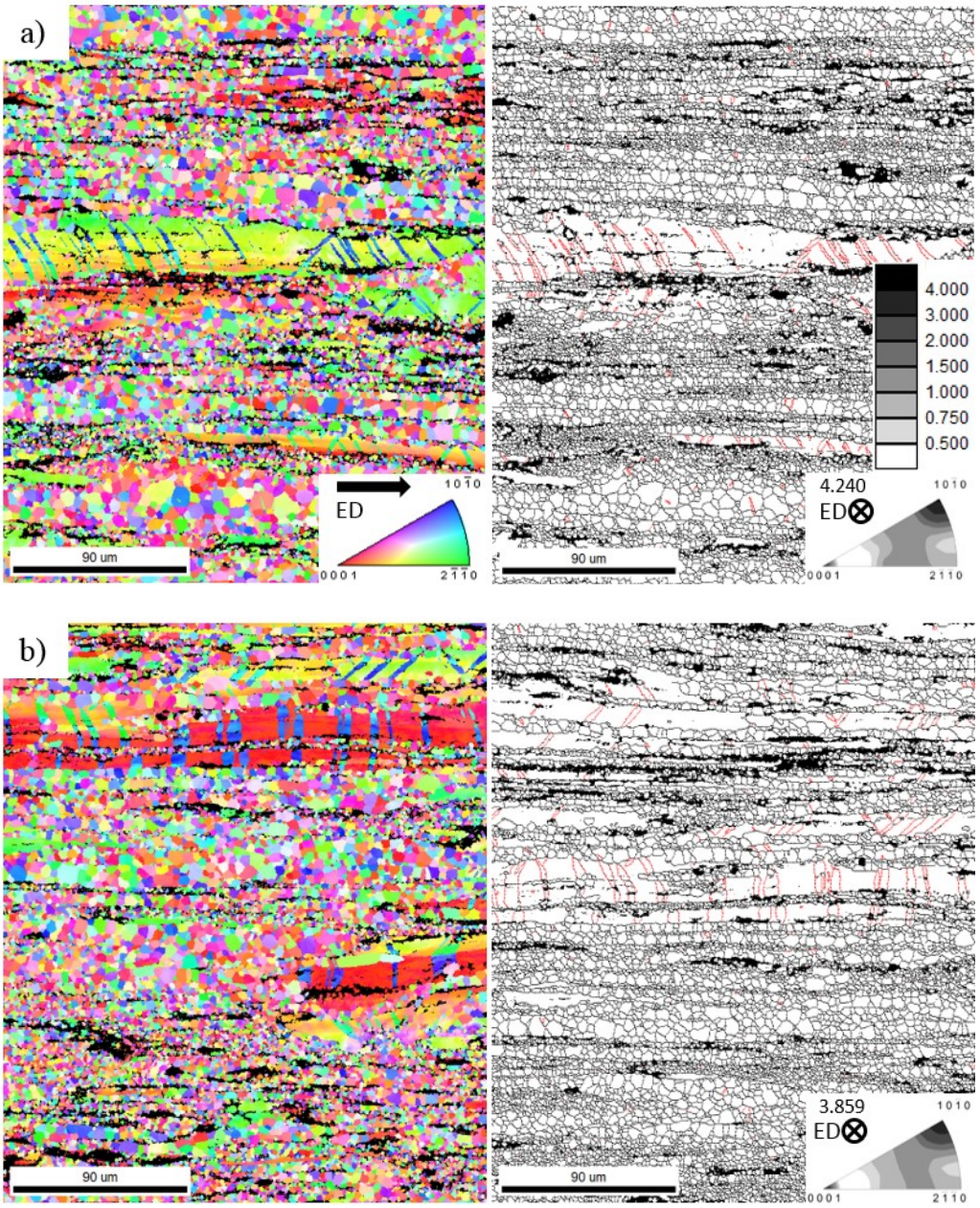

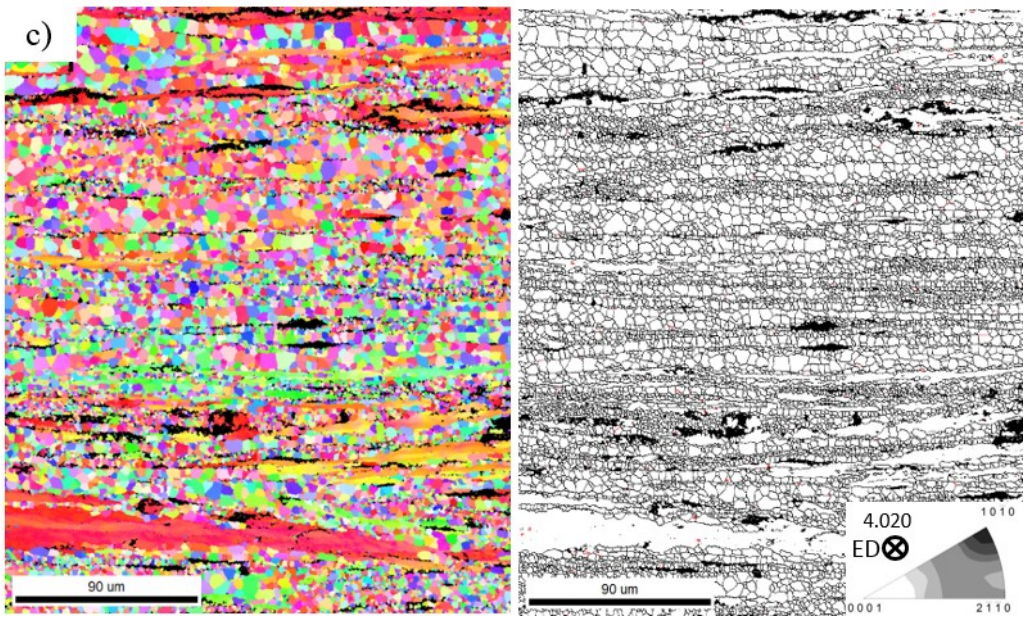

Fig. 4.30. The OIMs, the corresponding map with marked extension twin boundaries and calculated texture (IPF) for the WZ42 alloy deformed up to 2% of strain at a) 200 °C, b) 300 °C, and c) 350 °C. The scale of the IPFs is depicted in the (a). The numbers in the IPFs mark the maximum texture intensity as the multiple of random density (m.r.d.).

The OIM and GOS map of the WZ42 alloy deformed up to fracture at 200 °C is shown in Fig. 4.31.a. The twins nucleated after the macroscopic yield point (Fig. 4.30.a) proceed to develop and after fracture, the whole elongated grains are reoriented by nearly 90° resulting in the strong texture component at the (0001) pole, Fig. 4.31.a. No other twin type was observed in the alloy. From the GOS map, it is assumed that the deformation is homogeneously distributed in the recrystallized grains, while in the elongated grains relative high deformation is stored. These results are very similar to those obtained after RT deformation, section 4.2.2.3.

The OIMs and GOS maps of the WZ42 alloy deformed at 300 °C and 350 °C up to 30% of true strain are presented in Fig. 4.31.b,c, respectively. Although some twins are present in the microstructure deformed up to 2% of plastic strain at 300 °C, at the end of the deformation the texture component at the (0001) pole is not the dominant one. The intensity is distributed along the ring from $(10\bar{1}0)$ to $(2\bar{1}\bar{1}0)$ pole. In the GOS map shown in Fig. 4.31.b, some deformation free grains (color-coded as blue) can be observed. The volume fraction of grains with GOS ≤ 1° is 18%. The texture of the sample deformed until 30% of strain at 350 °C is significantly weaker than that in the initial state after extrusion. In the GOS map, besides the high fraction

of recrystallized grains with low internal strain, some larger grains with high stored deformation can be found. The volume fraction of the recrystallized grains with GOS ≤ 1° is 38%.

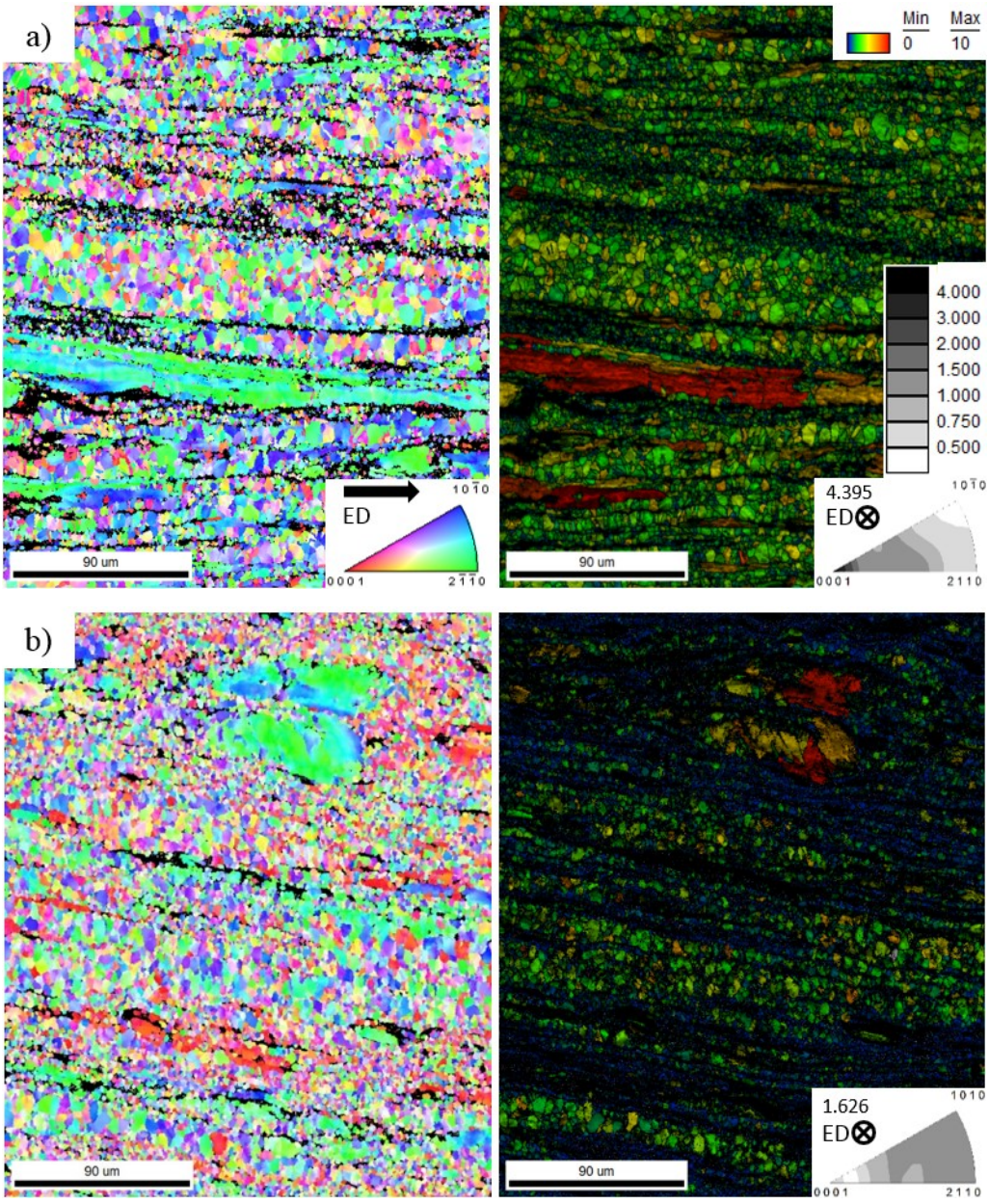

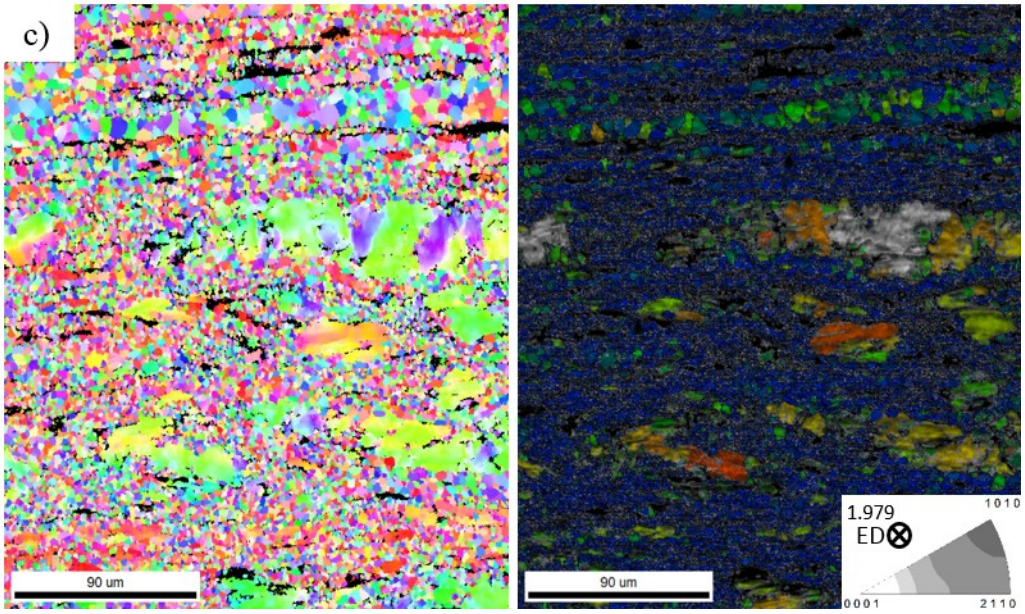

Fig. 4.31. The OIMs of the WZ42 alloy deformed till fracture a) at 200 °C; and up to 30% of strain at b) 300 °C, and c) 350 °C with the corresponding GOS map and calculated texture (IPF). GOS scale and the scale of the IPFs is depicted in the (a). The numbers in the IPFs mark the maximum texture intensity as the multiple of random density (m.r.d.).

The microstructures of the WZ104 alloy deformed up to 2% of plastic strain at 200°C, 300 °C, and 350 °C are presented in Fig. 4.32. Contrary to that in the WZ42 alloy, no twins are observed in the microstructure at this point of deformation. There are no big changes in the texture of these samples compared to the as-extruded state.

When the alloy is deformed until fracture at 200 °C (Fig. 4.33.a), quite intensive twinning is observed in the elongated grains, although some parts of these grains still have their original orientation (color-coded in red). The twinning also results in changes in the overall texture of the material: a very intensive maximum is formed at the (0001) pole. After the fracture, a relative high deformation is stored in the elongated grains with more even distribution of deformation in the recrystallized grains, see the GOS map in Fig. 4.33.a.

The microstructures of the WZ104 alloy deformed up to 30% of true strain at 300 °C and 350°C are presented in Fig. 4.33. b and c, respectively. No sign of twinning activity is observed in neither of the samples. However, a higher fraction of deformation-free recrystallized grains is present in the GOS maps comparing to the case of the WZ42 alloy at the same temperatures. The volume fraction of the grains with GOS ≤ 1° is 26% and 48% after deformation at 300 °C and 350 °C, respectively.

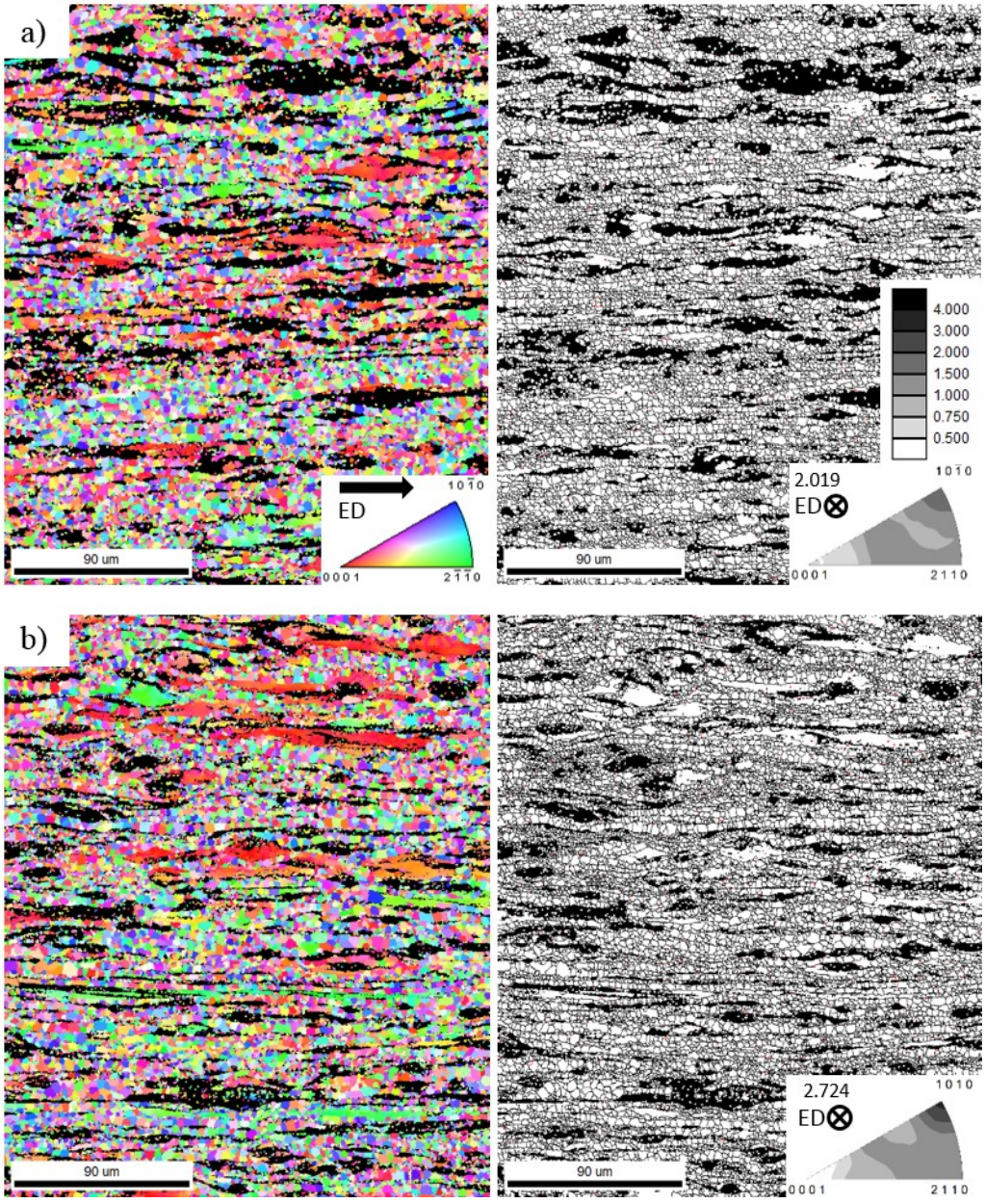
a)
90 um
ED
1010
0001
2110
4.000
3.000
2.000
1.500
1.000
0.750
0.500
1010
2.019
ED⊗
0001
2110
90 um
b)
90 um
2.724
ED⊗
1010
0001
2110
90 um

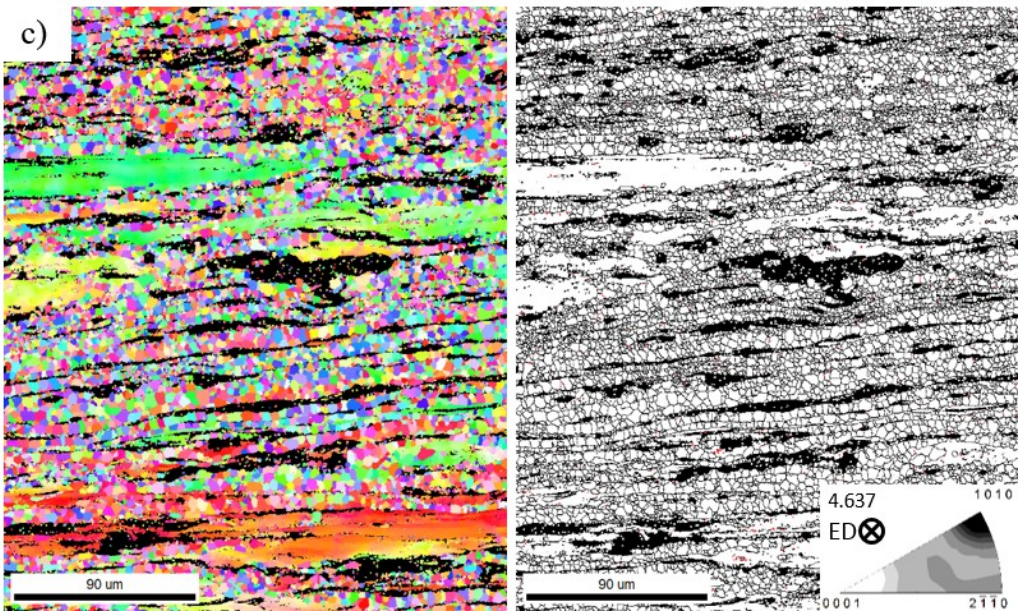

Fig. 4.32. The OIMs, the corresponding map with marked extension twin boundaries and calculated texture (IPF) for the WZ104 alloy deformed up to 2% of strain at a) 200 °C, b) 300 °C, and c) 350 °C. The scale of the IPFs is depicted in the (a). The numbers in the IPFs mark the maximum texture intensity as the multiple of random density (m.r.d.).

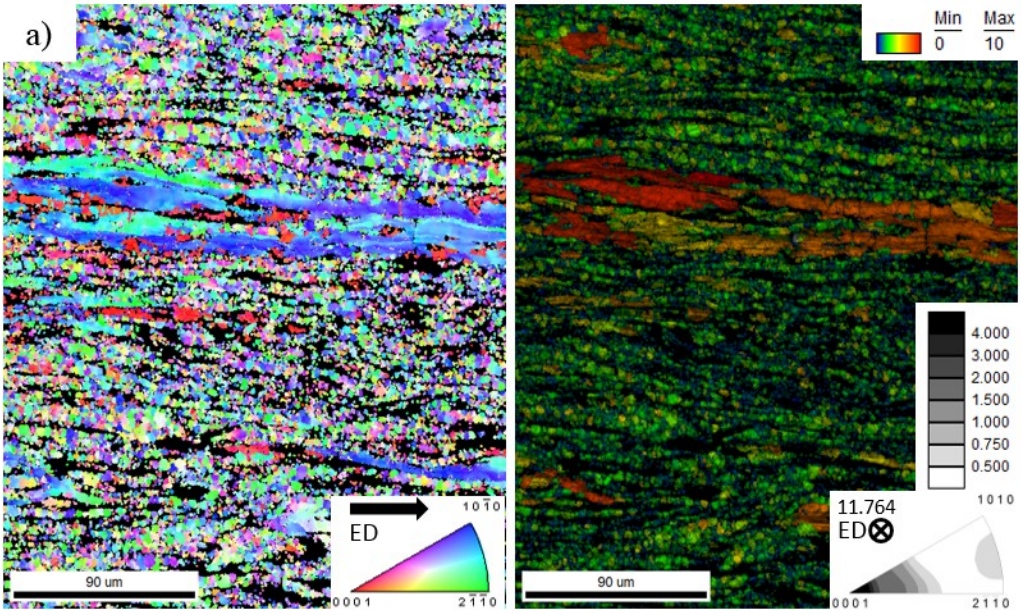

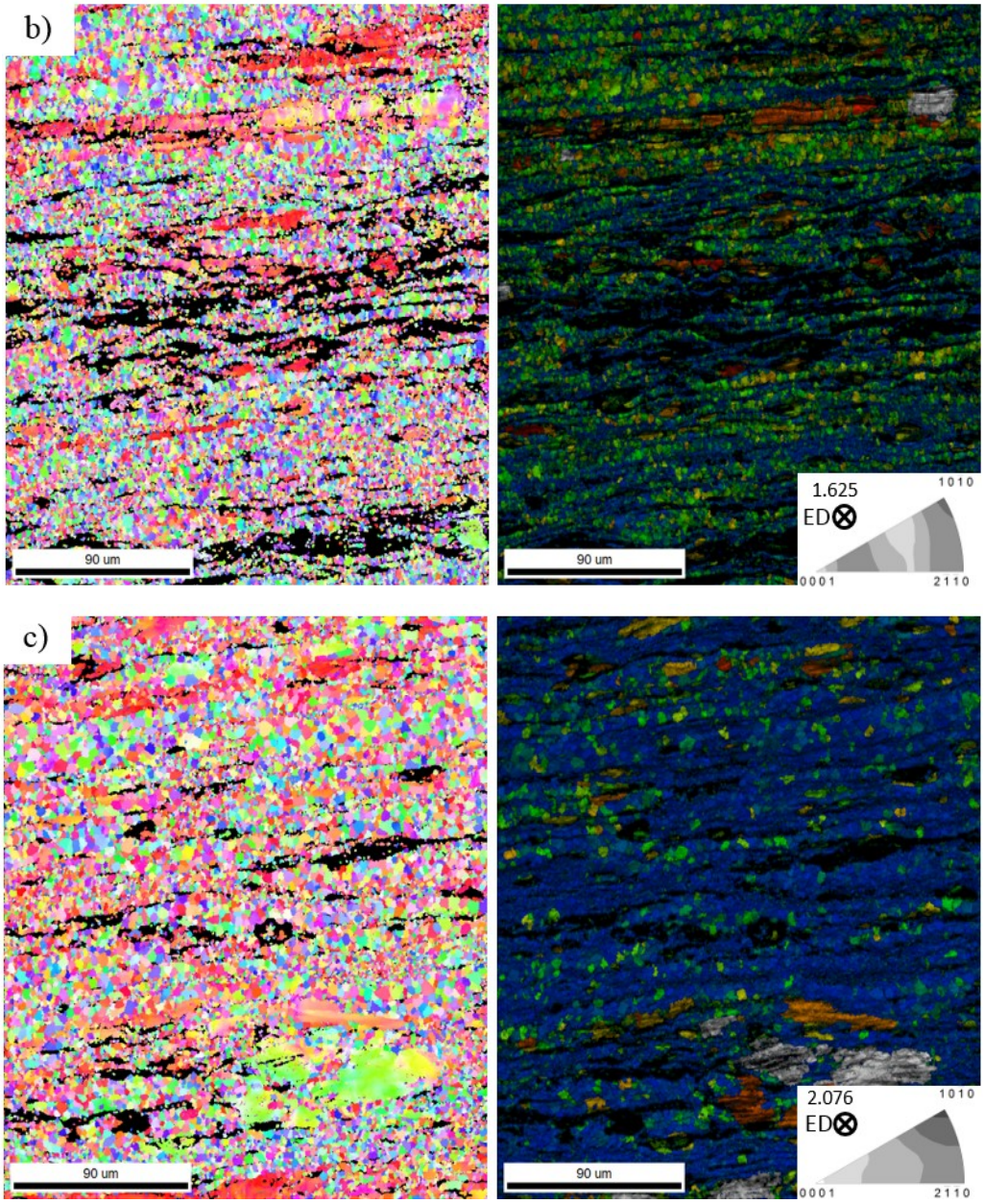

Fig. 4.33. The OIMs of the WZ104 alloy deformed till fracture a) at 200 °C; and up to 30% of strain at b) 300 °C, and c) 350 °C with the corresponding GOS map and calculated texture (IPF). GOS scale and the scale of the IPFs is depicted in the (a). The numbers in the IPFs mark the maximum texture intensity as the multiple of random density (m.r.d.).

To obtain information about the deformation of the LPSO phase the BSE images of the deformed WZ42 alloy were analyzed, Fig. 4.34. In addition to the high temperature deformation results, the microstructure deformed at RT is added for comparison. In the sample deformed at 200 °C, both kinks and cracks are observed throughout the microstructure. At 300 °C, kinking deformation is found to be the main

deformation mode. However, in the case of deformation at 350 °C, only a few kinks are observed. No cracks or debonding of the LPSO phase during compressive deformation up to 30 % at temperatures above 200 °C were found.

The BSE images of the deformed WZ104 alloy are shown in Fig. 4.35. Similarly to that at RT, very intense kinking deformation is seen in the samples deformed at 200 °C and 300 °C. However, at 350 °C, no significant kinking is observed in the microstructure.

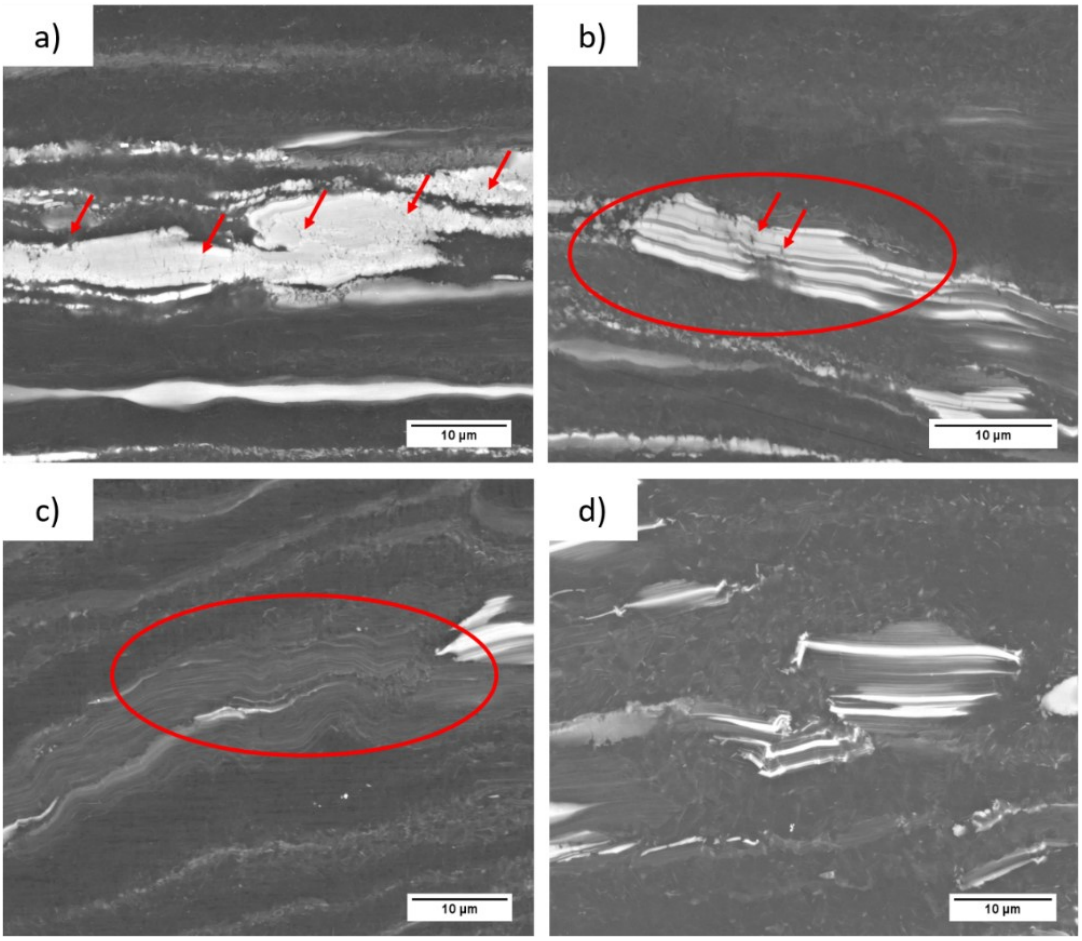

Fig. 4.34. BSE images after the deformation of the WZ42 alloy up to fracture at a) RT, and b) 200 °C; and up to 30% of strain at c) 300 °C, and d) 350 °C. The red arrows mark the cracks of the LPSO phase while the red circles mark the deformation kinks.

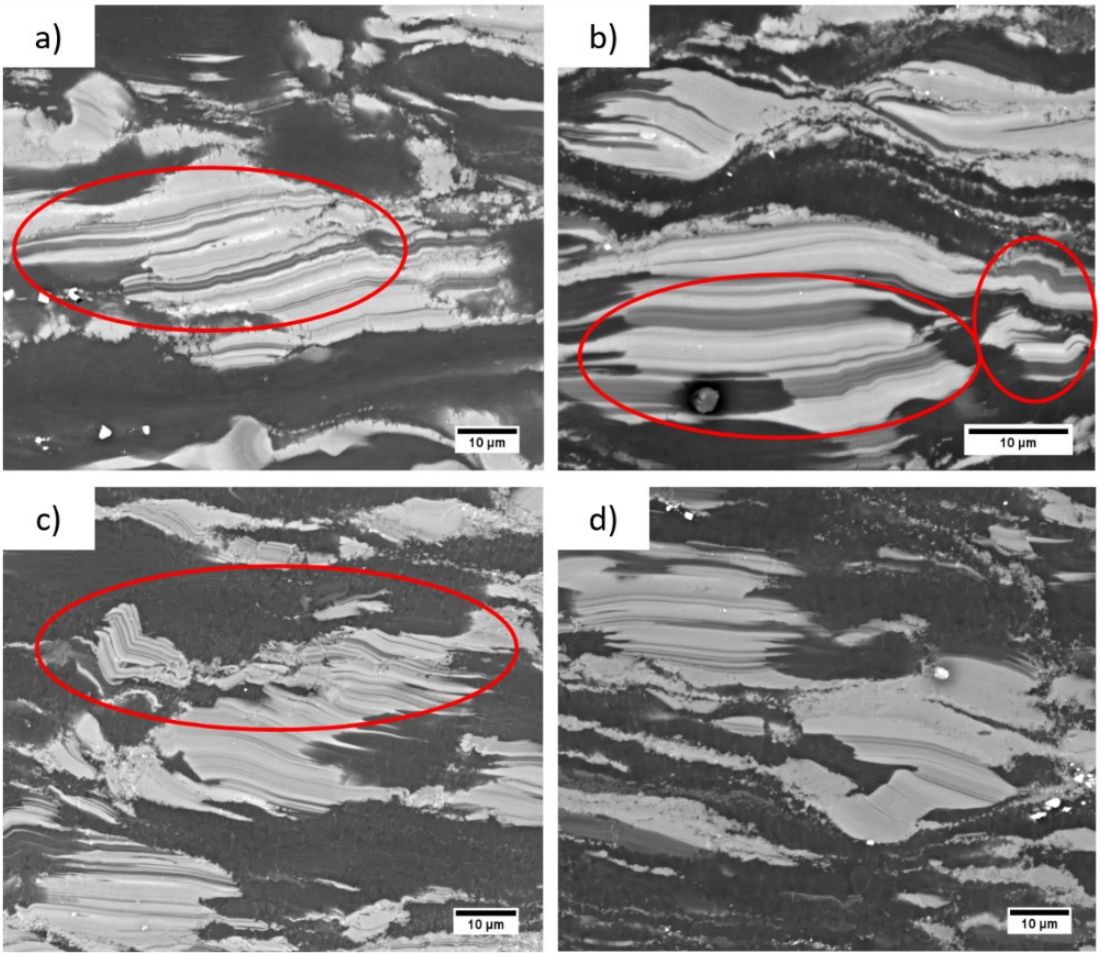

Fig. 4.35. BSE images after the deformation of the WZ104 alloy up to fracture at a) RT, and b) 200 °C; and up to 30% of strain at c) 300 °C, and d) 350 °C. The red circles mark the deformation kinks.

4.3.2. Discussion: compressive deformation at elevated temperatures

During deformation at high temperatures, there is a competition between dynamic softening and strain hardening. At the initial stage of deformation, the dislocation density dramatically increases [203]. Thus, strain hardening overcomes the dynamic softening and the true stress-true strain curves exhibit a rising trend of work hardening (see Fig.4.26.). With the increment of deformation, the internal stress accumulates and provides a driving force for the movement of dislocations such as dislocation climb or cross slip. At higher temperatures (300 °C and 350 °C), the dynamic softening, like dynamic recrystallization, occurs and starts to compensate for the effect of work hardening. The achieved high ductility at higher temperatures could

be linked to the dynamic recrystallization process as well as the randomly oriented recrystallized grains, which significantly contribute to the ductility of the alloys [4].

In the WZ42 alloy deformed at 200 °C, similarly to the deformation at RT, the grains with their $\{10\bar{1}1\}$ and $\{10\bar{1}2\}$ planes oriented parallel to the compression axis lose their elastic linearity at the macroscopic yield point which indicates the involvement of the basal slip in strain accommodation. Contrary to RT, at 200 °C no evidence of the micro-yielding is observed, see Fig. 4.27.a. However, after the yield point, the evolution of the intensities of the (0002) and $\{10\bar{1}0\}$ diffraction peaks and the axial distribution function of the (0002) peak in Fig. 4.29.a. indicates strong twinning activity. It is also proved by the microstructure observations, including texture development, see Figs. 4.30.a and 4.31.a. From the behavior of the (0002) diffraction peak, the involvement of a <c+a> slip is supposed at deformation above 275 MPa.

The macroscopic yielding of the WZ104 alloy at 200 °C is controlled by the basal slip and twinning becomes active slightly after the yield point. However, as it is presented in Figs. 4.28.a. and 4.29., the increment of the intensity of the (0002) diffraction peak is much lower than that in the WZ42 alloy. Correspondingly, no evidence of extension twins in the microstructure deformed up to 2% of strain is observed, Fig. 4.32. Nevertheless, at the end of deformation, from both the synchrotron diffraction data and the microscopy observations the importance of extension twinning is evident.

The convex shape of the deformation curve of the WZ42 alloy observed at 300 °C is the typical sign of the dislocation-dominated deformation. The observed strain hardening could be the result of the increasing number of obstacles (such as forest dislocations or twin boundaries) for free dislocation motion. Extension twinning still plays a role at the beginning of the plastic deformation, as reflected in the evolution of the intensities of the $\{10\bar{1}0\}$-(0002) conjugated planes. However, its contribution is much smaller compared to that at lower tested temperatures. The presence of the extension twins in the elongated grains is confirmed by the EBSD analysis, see Fig. 4.30.b. On the other hand, the 2nd order pyramidal slip, which has been found to be active at temperatures above 200 °C [136] cannot be excluded. Recently, Hagihara et al. have shown [204] that kinking can be activated at this temperature. As it is known, the (0002) planes of the Mg phase and the (00018)

planes of the LPSO phase are aligned [205]. Thus, despite the low volume content of the LPSO phase, the kinking process could influence the behavior of the Mg phase as well.

The deformation curve changes around 15% of strain and a dynamic softening accompanied by the decrease of the lattice strain and intensity of the $\{10\bar{1}0\}$ and (0002) diffraction peaks is observed. This behavior is the opposite of that measured at lower temperatures, where the lattice strains continued to increase till the end of the deformation. Therefore, the decrease of the lattice strains during the ongoing deformation could be the result of the dynamic recrystallization process. The results obtained by EBSD technique also indicate the activation of dynamic recrystallization at this temperature. Some deformation free grains (color-coded as blue in Fig. 4.30.b) in the GOS maps can be observed and the texture calculated from the EBSD data after deformation is weaker compared to that in the initial, as-extruded state of the alloy. After extrusion, the intensity is distributed along the $(10\bar{1}0)$-$(2\bar{1}\bar{1}0)$ ring with higher intensity at the $(10\bar{1}0)$ pole thanks to preferential orientation of the elongated grains. This maximum is significantly reduced during deformation at 300 °C by (i) extension twinning which rotates these planes to the (0001) pole and (ii) dynamic recrystallization which result in smoother distribution of the planes along the ring. Therefore, the local maximum observed around 40° from the axial direction in the axial distribution function of the (0002) peak, shown in Fig 4.29.a., is the result of the simultaneous activation of <c+a> slip and dynamic recrystallization.

Contrary to the WZ42 alloy, in the WZ104 alloy deformed at 300 °C, no sign of twinning activity is observed. The absolute value of the lattice strain on the (0002) plane increases up to 12.5% of deformation. Since the Schmid factor for the basal slip is zero for these grains (basal planes are oriented parallel to the axial axis, i.e. loading axis), the deformation is supposed to proceed by the activation of the non-basal slip or extension twinning. Hence, no significant change of the intensity of the (0002) diffraction peak is observed, the activation of non-basal slip system(s) is more likely. It is in agreement with the fact that CRSS for non-basal slip is reduced at elevated temperature [206, 207]. Further, the decrease of the lattice strain after 12.5% of deformation could be related to the dynamic recrystallization of the alloy, similar to that in the WZ42 alloy. The lattice strain on the $\{11\bar{2}0\}$ planes continues to increase till the end of the deformation, meaning that these grains bear higher stress. The grains

with their $\{11\bar{2}0\}$ planes oriented perpendicular to the ED have zero Schmid factor for the basal slip, therefore, the non-basal prismatic slip system should be activated [192]. Therefore, after 12.5 % of deformation, a competition between the non-basal slip and dynamic recrystallization may take place.

During deformation at 350 °C, the intensity changes of the $\{10\bar{1}0\}$-(0002) conjugated planes do not suggest any twinning activity in neither of the investigated alloys. The absence of twinning is also supported by the microstructure observations (Figs. 4.30.c and 4.32.c). At the same time, in the GOS map, a high fraction of recrystallized grains free of deformation can be found. It is in good agreement with the results of the diffraction measurements shown in Fig. 4.29., where the distribution of the intensity of the (0002) peak is more random, compared to the previous cases. Moreover, the decrement of the lattice strains after the yield point also suggests the dominance of the dynamic recrystallization process.

It is obvious that the deformation at RT proceeds mainly in the Mg matrix. However, with increasing deformation temperature the preference in deformation transfers from the Mg matrix to the LPSO phase. The formation of deformation kinks is more likely at elevated temperature (see Figs. 4.34. and 4.35.). Matsumoto and Uranagase have proposed [81] that the kink band is formed by a large number of edge dislocations generated on the basal plane as a result of cross-slip of prismatic <a> dislocation. This idea is intensively investigated by other researchers using HR-TEM [5, 179, 208]. The increase of the test temperature leads to decreasing the CRSS of the non-basal slip systems [206, 207] and therefore, it can favor the kinking process at elevated temperatures. On the other hand, at 350 °C, only a few kinks were observed independently on the volume fraction of the LPSO phase. Nevertheless, it is in agreement with already reported works [9, 204, 209], where it has been shown that the LPSO phase loses its strengthening effect at temperatures over 250-300 °C. Therefore, it is supposed that at this temperature, the deformation of the alloy mainly takes place in the Mg matrix and the dynamic recrystallization of the Mg matrix overcomes other processes. At temperatures above 200 °C, no debonding or microcracking was observed in the investigated alloys. Their absence could be related to the coherent interface between the Mg matrix and the LPSO phase along both the basal and prismatic planes as it has been proposed by Tahreen et al. [7].

Conclusions

In the thesis, a comprehensive study of deformation mechanisms of two extruded Mg-LPSO alloys was performed. Combination of several experimental methods, including transmission and scanning electron microscopy, *in-situ* acoustic emission and synchrotron diffraction were used for the investigation of the microstructure evolution and deformation mechanisms. The following conclusions can be drawn:

1. **Initial microstructure and texture of the Mg-LPSO alloys**

   The combination of the extrusion ratio of 18:1 with a slow extrusion speed of 0.5 mms^{-1} led to inhomogeneous microstructure with small recrystallized grains, non-recrystallized grains elongated along ED and fibers of the LPSO phase along ED in both studied Mg-LPSO alloys. The volume fraction of the LPSO phase increased with increasing amount of the alloying element (Y and Zn), thus the WZ104 alloy contains 32% and the WZ42 alloy – 10% volume fraction of the LPSO phase.

   In addition to the LPSO phase, precipitates of Mg_2Ca, W-phase, and YH_2 particles were found by TEM and EDAX analysis in both alloys.

   During extrusion, a significant texture with basal planes oriented parallel to ED was formed. The main contributors to the preferred texture were the elongated non-recrystallized grains, while the recrystallized grains showed nearly random orientation distribution. Synchrotron diffraction has shown that similarly to the Mg matrix, the LPSO phase also has a basal texture.

2. **Deformation behavior at room temperature**

   Although the ASK analysis has been already successfully applied to analyze and distinguish different sources of the AE signal during deformation of textured Mg alloys, it is proven to be a useful tool also in Mg alloys containing LPSO phase with more complex microstructure. A good agreement between the ASK results, synchrotron diffraction and microstructural observation was achieved.

   In extruded Mg alloys, the value of the yield strength in compression was reduced compared to tensile deformation, due to the preferred activation of extension twinning. However, in the WZ104 alloy, a reversed tension-compression yield

strength asymmetry was observed. It was shown by the *in-situ* synchrotron diffraction experiments that in the WZ42 alloy the compressive yielding was controlled by twinning in the elongated grains and by the basal slip in the recrystallized grains. Such behavior is common for Mg alloys with yield strength lower in compression than that in tension. Contrary, in the WZ104 alloy, the twinning activation was suppressed and the macroscopic yielding was controlled by basal slip. Therefore, the yield strength reached relative high values in compression. Moreover, the LPSO phase itself has a higher yield strength in compression than in tension. These effects together resulted in the reversed tension-compression yield asymmetry of the WZ104 alloy.

Even though the low volume fraction of the LPSO phase in the WZ42 alloy did not allow fitting the diffraction data of this phase, it was possible to study the lattice strain evolution on the $\{10\bar{1}8\}$ LPSO plane in the WZ104 alloy. It was proved that the LPSO phase bears higher deformation than the Mg matrix. Using BSE images, it was shown that at RT the LPSO phase can be deformed by deformation kinking in the WZ104 alloy, but no change of the LPSO phase in the WZ42 alloy was observed.

During tensile deformation, thanks to the alloys texture, the twin activation was reduced and the role of the non-basal slip was increased. The formation of the deformation kinks was also restricted. Thus a large number of cracks perpendicular to the loading direction were found in the microstructure at the end of the tensile deformation.

3. Deformation behavior at elevated temperature

The compressive deformation behavior at 200 °C of both alloys was similar to that observed at RT. The extension twinning still played an important role and the kink formation was intense during the plastic deformation of the alloys.

Although at 300 °C in the WZ42 alloy some extension twins at the yield point were present, they were not the dominant deformation mechanism anymore. The activation of the non-basal slip systems was confirmed by the diffraction measurements. At the later stage of the deformation, dynamic recrystallization resulted in a decrease of the lattice strains and caused a dynamic softening.

At 350 °C, the amount of the dynamically recrystallized grains was higher for both alloys than that at 300 °C. As a result, at the end of the deformation texture with lower intensity, compared to the as-extruded state and more even distribution of the (0002) diffraction peak was observed.

The increase of the temperature favored the activation of kinking of the LPSO phase, as it was shown by the BSE images. However, at 350 °C, barely any kinks were found in either of the investigated alloys and the deformation curves were quite similar to each other. Thus, the LPSO phase lost its strengthening effect at this deformation temperature.

Bibliography

[1] MICHALEK, J.J., P.Y. PAPALAMBROS and S.J. SKERLOS. A Study of Fuel Efficiency and Emission Policy Impact on Optimal Vehicle Design Decisions. *Journal of Mechanical Design*. 2004, vol. 126, no. 6, pp. 1062–1070.

[2] MORDIKE, B.L. and T. EBERT. Magnesium: Properties – applications - potential. *Materials Science and Engineering: A*. 2001, vol. 302, no. 1, pp. 37–45.

[3] FEDERAL AVIATION ADMINISTRATION. *Aircraft Materials Fire Test Handbook*. 27. May 2019.

[4] YAMASAKI, M., K. HASHIMOTO, K. HAGIHARA and Y. KAWAMURA. Effect of multimodal microstructure evolution on mechanical properties of Mg–Zn–Y extruded alloy. *Acta Materialia*. 2011, vol. 59, no. 9, pp. 3646–3658.

[5] HAGIHARA, K., N. YOKOTANI and Y. UMAKOSHI. Plastic deformation behavior of Mg12YZn with 18R long-period stacking ordered structure. *Intermetallics*. 2010, vol. 18, no. 2, pp. 267–276.

[6] HAGIHARA, K., Y. SUGINO, Y. FUKUSUMI, Y. UMAKOSHI and T. NAKANO. Plastic Deformation Behavior of $Mg_{12}ZnY$ LPSO-Phase with 14H-Typed Structure. *Materials Transactions*. 2011, vol. 52, no. 6, pp. 1096–1103.

[7] TAHREEN, N., D.F. ZHANG, F.S. PAN, X.Q. JIANG, C. LI, D.Y. LI and D.L. CHEN. Characterization of hot deformation behavior of an extruded Mg–Zn–Mn–Y alloy containing LPSO phase. *Journal of Alloys and Compounds*. 2015, vol. 644, pp. 814–823.

[8] GARCÉS, G., K. MÁTHIS, J. MEDINA, K. HORVÁTH, D. DROZDENKO, E. OÑORBE, P. DOBROŇ, P. PÉREZ, M. KLAUS and P. ADEVA. Combination of in-situ diffraction experiments and acoustic emission testing to understand the compression behavior of Mg-Y-Zn alloys containing LPSO phase under different loading conditions. *International Journal of Plasticity*. 2018, vol. 106, pp. 107–128.

[9] OÑORBE, E., G. GARCÉS, P. PÉREZ and P. ADEVA. Effect of the LPSO volume fraction on the microstructure and mechanical properties of $Mg–Y_{2X}–Zn_X$ alloys. *Journal of Materials Science*. 2012, vol. 47, no. 2, pp. 1085–1093.

[10] ABE, E., Y. KAWAMURA, K. HAYASHI and A. INOUE. Long-period ordered structure in a high-strength nanocrystalline Mg-1 at% Zn-2 at% Y

alloy studied by atomic-resolution Z-contrast STEM. *Acta Materialia*. 2002, vol. 50, no. 15, pp. 3845–3857.

[11] ITOI, T., T. SEIMIYA, Y. KAWAMURA and M. HIROHASHI. Long period stacking structures observed in Mg97Zn1Y2 alloy. *Scripta Materialia*. 2004, vol. 51, no. 2, pp. 107–111.

[12] GARCES, G., D.G. MORRIS, M.A. MUÑOZ-MORRIS, P. PEREZ, D. TOLNAI, C. MENDIS, A. STARK, H.K. LIM, S. KIM, N. SHELL and P. ADEVA. Plasticity analysis by synchrotron radiation in a Mg97Y2Zn1 alloy with bimodal grain structure and containing LPSO phase. *Acta Materialia*. 2015, vol. 94, pp. 78–86.

[13] HAGIHARA, K., A. KINOSHITA, Y. SUGINO, M. YAMASAKI, Y. KAWAMURA, H.Y. YASUDA and Y. UMAKOSHI. Effect of long-period stacking ordered phase on mechanical properties of Mg97Zn1Y2 extruded alloy. *Acta Materialia*. 2010, vol. 58, no. 19, pp. 6282–6293.

[14] HORVÁTH KLAUDIA, DROZDENKO DARIA, DANIŠ STANISLAV, GARCÉS GERARDO, MÁTHIS KRISTIÁN, KIM SHAE and DOBROŇ PATRIK. Characterization of Microstructure and Mechanical Properties of Mg–Y–Zn Alloys with Respect to Different Content of LPSO Phase. *Advanced Engineering Materials*. 2017, vol. 20, no. 1, p. 1700396.

[15] Japanese motor manufacturers looking for alternatives to rare-earth metals. *Green Car Congress*.

[16] ČAPEK, J., K. MÁTHIS, B. CLAUSEN, J. STRÁSKÁ, P. BERAN and P. LUKÁŠ. Study of the loading mode dependence of the twinning in random textured cast magnesium by acoustic emission and neutron diffraction methods. *Materials Science and Engineering: A*. 2014, vol. 602, pp. 25–32.

[17] MURÁNSKY, O., M.R. BARNETT, D.G. CARR, S.C. VOGEL and E.C. OLIVER. Investigation of deformation twinning in a fine-grained and coarse-grained ZM20 Mg alloy: Combined in situ neutron diffraction and acoustic emission. *Acta Materialia*. 2010, vol. 58, no. 5, pp. 1503–1517.

[18] MÁTHIS, K., P. BERAN, J. ČAPEK and P. LUKÁŠ. *In-situ* neutron diffraction and acoustic emission investigation of twinning activity in magnesium. *Journal of Physics: Conference Series*. 2012, vol. 340, p. 012096.

[19] POMPONI, E. and A. VINOGRADOV. A real-time approach to acoustic emission clustering. *Mechanical Systems and Signal Processing*. 2013, vol. 40, no. 2, pp. 791–804.

[20] YOO, M.H. Slip, twinning, and fracture in hexagonal close-packed metals. *Metallurgical Transactions A*. 1981, vol. 12, no. 3, pp. 409–418.

[21] LUBLINER, J. *Plasticity Theory*. B.m.: Courier Corporation, 2008.

[22] CHRISTIAN, W. and S. MAHAJANT. DEFORMATION TWINNING. *Progress in Materials Science*. 1995, vol. 39, no. 1, pp. 1–157.

[23] ANANTHAKRISHNA, G. Current theoretical approaches to collective behavior of dislocations. *Physics Reports*. 2007, vol. 440, no. 4, pp. 113–259.

[24] HULL, D. and D.J. BACON. Chapter 1 - Defects in Crystals. In: D. HULL and D. J. BACON, eds. *Introduction to Dislocations (Fifth Edition)*. Oxford: Butterworth-Heinemann, 2011, pp. 1–20.

[25] ILLKOVÁ, K. Influence of Solid Solution Elements and Precipitate Formation on the Mechanical Behaviour of Magnesium Alloys. *Dissertation thesis*. 2013.

[26] SCHMID, E. and G. WASSERMANN. Über die Textur gezogener Magnesium- und Zinkdrähte. *Naturwissenschaften*. 1929, vol. 17, no. 18, pp. 312–314.

[27] ANDO, S. and H. TONDA. Non-Basal Slips in Magnesium and Magnesium-Lithium Alloy Single Crystals. *Materials Science Forum*. 2000, vol. 350-351, pp. 43-48.

[28] STAROSELSKY, A. and L. ANAND. A constitutive model for hcp materials deforming by slip and twinning: application to magnesium alloy AZ31B. *International Journal of Plasticity*. 2003, vol. 19, no. 10, pp. 1843–1864.

[29] KRATOCHVÍL, P., P. LUKÁČ and B. SPRUŠIL. *Úvod do fyziky kovu I.* Praha 1984.

[30] MISES R. V. Mechanik der plastischen Formänderung von Kristallen. *ZAMM - Journal of Applied Mathematics and Mechanics / Zeitschrift für Angewandte Mathematik und Mechanik*. 2006, vol. 8, no. 3, pp. 161–185.

[31] KIM, G.S. Small Volume Investigation of Slip and Twinning in Magnesium Single Crystals. *Dissertation thesis*. 2011.

[32] WONSIEWICZ, B.C. PLASTICITY OF MAGNESIUM CRYSTALS. *Dissertation thesis*. 1966.

[33] CHAPUIS, A. and J.H. DRIVER. Temperature dependency of slip and twinning in plane strain compressed magnesium single crystals. *Acta Materialia*. 2011, vol. 59, no. 5, pp. 1986–1994.

[34] KLEINER, S. and P.J. UGGOWITZER. Mechanical anisotropy of extruded Mg–6% Al–1% Zn alloy. *Materials Science and Engineering: A*. 2004, vol. 379, no. 1, pp. 258–263.

[35] DOBROŇ, P., J. BOHLEN, F. CHMELÍK, P. LUKAC, D. LETZIG and K. KAINER. Mechanical anisotropy of AZ31 magnesium alloy sheet investigated by the acoustic emission technique. *Kovove Materialy*. 2007, vol. 45, pp. 129–133.

[36] BARNETT, M.R., M.D. NAVE and C.J. BETTLES. Deformation microstructures and textures of some cold rolled Mg alloys. *Materials Science and Engineering: A*. 2004, vol. 386, no. 1, pp. 205–211.

[37] AKHTAR, A. and E. TEGHTSOONIAN. Solid solution strengthening of magnesium single crystals—I alloying behaviour in basal slip. *Acta Metallurgica*. 1969, vol. 17, no. 11, pp. 1339–1349.

[38] AKHTAR, A. and E. TEGHTSOONIAN. Solid solution strengthening of magnesium single crystals—ii the effect of solute on the ease of prismatic slip. *Acta Metallurgica*. 1969, vol. 17, no. 11, pp. 1351–1356.

[39] OBARA, T., H. YOSHINGA and S. MOROZUMI. {11$\bar{2}$2} ⟨1123⟩ Slip system in magnesium. *Acta Metallurgica*. 1973, vol. 21, no. 7, pp. 845–853.

[40] AGNEW, S.R. and Ö. DUYGULU. Plastic anisotropy and the role of non-basal slip in magnesium alloy AZ31B. *International Journal of Plasticity*. 2005, vol. 21, no. 6, pp. 1161–1193.

[41] BAKARIAN, P.W. and C.H. MATHEWSON. Slip and twinning in magnesium single crystals at elevated temperatures. *Transaction of the Metallurgical Society of Aime*. 1943, vol. 1943, no. 152, pp. 226–254.

[42] KELLY, E.W. and W.F. HOSFORD. Deformation characteristics of textured magnesium. *Transaction of the Metallurgical Society of Aime*. 1968, vol. 242, no. 4, pp. 654–661.

[43] CHRISTIAN, J.W. and S. MAHAJAN. Deformation twinning. *Progress in Materials Science*. 1995, vol. 39, no. 1, pp. 1–157.

[44] COTTRELL, A.H. and B.A. BILBY. LX. A mechanism for the growth of deformation twins in crystals. *The London, Edinburgh, and Dublin*

Philosophical Magazine and Journal of Science. 1951, vol. 42, no. 329, pp. 573–581.

[45] MAHAJAN, S. and D.F. WILLIAMS. Deformation Twinning in Metals and Alloys. *International Metallurgical Reviews*. 1973, vol. 18, no. 2, pp. 43–61.

[46] BILBY BRUCE ALEXANDER, CROCKER A. G. and COTTRELL ALAN HOWARD. The theory of the crystallography of deformation twinning. *Proceedings of the Royal Society of London. Series A. Mathematical and Physical Sciences*. 1965, vol. 288, no. 1413, pp. 240–255.

[47] FARKAS, G. Investigation of residual stresses and deformation mechanisms of magnesium-based composites by means of neutron diffraction and acoustic emission methods. *Dissertation thesis*. 2017.

[48] BROWN, D.W., S.R. AGNEW, M.A.M. BOURKE, T.M. HOLDEN, S.C. VOGEL and C.N. TOMÉ. Internal strain and texture evolution during deformation twinning in magnesium. *Materials Science and Engineering: A*. 2005, vol. 399, no. 1, pp. 1–12.

[49] BARNETT, M.R. Twinning and the ductility of magnesium alloys: Part I: "Tension" twins. *Materials Science and Engineering: A*. 2007, vol. 464, no. 1, pp. 1–7.

[50] PARTRIDGE, P.G. The crystallography and deformation modes of hexagonal close-packed metals. *Metallurgical Reviews*. 1967, vol. 12, no. 1, pp. 169–194.

[51] WU, W., H. QIAO, K. AN, X. GUO, P. WU and P.K. LIAW. Investigation of deformation dynamics in a wrought magnesium alloy. *International Journal of Plasticity*. 2014, vol. 62, pp. 105–120.

[52] SARKER, D. and D.L. CHEN. Detwinning and strain hardening of an extruded magnesium alloy during compression. *Scripta Materialia*. 2012, vol. 67, no. 2, pp. 165–168.

[53] BARNETT, M.R. Twinning and the ductility of magnesium alloys. *Materials Science and Engineering: A*. 2007, vol. 464, no. 1, pp. 8–16.

[54] TOMÉ, C.N., I.J. BEYERLEIN, J. WANG and R.J. MCCABE. A multi-scale statistical study of twinning in magnesium. *JOM*. 2011, vol. 63, no. 3, pp. 19–23.

[55] WANG, J., I.J. BEYERLEIN and C.N. TOMÉ. An atomic and probabilistic perspective on twin nucleation in Mg. *Scripta Materialia*. 2010, vol. 63, no. 7, pp. 741–746.

[56] VINOGRADOV, A., E. VASILEV, M. SELEZNEV, K. MÁTHIS, D. ORLOV and D. MERSON. On the limits of acoustic emission detectability for twinning. *Materials Letters*. 2016, vol. 183, pp. 417–419.

[57] BARNETT, M.R. A rationale for the strong dependence of mechanical twinning on grain size. *Scripta Materialia*. 2008, vol. 59, no. 7, pp. 696–698.

[58] DOBROŇ, P., F. CHMELÍK, S. YI, K. PARFENENKO, D. LETZIG and J. BOHLEN. Grain size effects on deformation twinning in an extruded magnesium alloy tested in compression. *Scripta Materialia*. 2011, vol. 65, no. 5, pp. 424–427.

[59] BEYERLEIN, I.J., L. CAPOLUNGO, P.E. MARSHALL, R.J. MCCABE and C.N. TOMÉ. Statistical analyses of deformation twinning in magnesium. *Philosophical Magazine*. 2010, vol. 90, no. 16, pp. 2161–2190.

[60] JONAS, J.J., S. MU, T. AL-SAMMAN, G. GOTTSTEIN, L. JIANG and Ė. MARTIN. The role of strain accommodation during the variant selection of primary twins in magnesium. *Acta Materialia*. 2011, vol. 59, no. 5, pp. 2046–2056.

[61] MU, S., J.J. JONAS and G. GOTTSTEIN. Variant selection of primary, secondary and tertiary twins in a deformed Mg alloy. *Acta Materialia*. 2012, vol. 60, no. 5, pp. 2043–2053.

[62] BARNETT, M.R., N. STANFORD, A. GHADERI and F. SISKA. Plastic relaxation of the internal stress induced by twinning. *Acta Materialia*. 2013, vol. 61, no. 20, pp. 7859–7867.

[63] ZHU, Y.M., M. WEYLAND, A.J. MORTON, K. OH-ISHI, K. HONO and J.F. NIE. The building block of long-period structures in Mg–RE–Zn alloys. *Scripta Materialia*. 2009, vol. 60, no. 11, pp. 980–983.

[64] ZHU, Y.M., A.J. MORTON and J.F. NIE. The 18R and 14H long-period stacking ordered structures in Mg–Y–Zn alloys. *Acta Materialia*. 2010, vol. 58, no. 8, pp. 2936–2947.

[65] NAKASHIMA, K., H. IWASAKI, T. MORI, T. MOHRI, M. MABUCHI, M. NAKAMURA, T. ASAHINA and K. HIGASHI. Tensile Properties of a P/M Mg-5Y-6Re Alloy. *Materials Science Forum*. vol. 350-351, pp. 87-92 2000.

[66] NISHIDA, M., T. YAMAMURO, M. NAGANO, Y. MORIZONO and Y. KAWAMURA. Electron Microscopy Study of Microstructure Modifications in RS P/M Mg97Zn1Y2 Alloy. *Materials Science Forum*. 2003, vol. 419-422, pp. 715-720.

[67] MATSUDA, M., S. II, Y. KAWAMURA, Y. IKUHARA and M. NISHIDA. Variation of long-period stacking order structures in rapidly solidified Mg97Zn1Y2 alloy. *Materials Science and Engineering: A*. 2005, vol. 393, no. 1, pp. 269–274.

[68] KAWAMURA, Y. and M. YAMASAKI. Formation and Mechanical Properties of $Mg_{97}Zn_1RE_2$ Alloys with Long-Period Stacking Ordered Structure. *MATERIALS TRANSACTIONS*. 2007, vol. 48, no. 11, pp. 2986–2992.

[69] ABE, E., A. ONO, T. ITOI, M. YAMASAKI and Y. KAWAMURA. Polytypes of long-period stacking structures synchronized with chemical order in a dilute Mg–Zn–Y alloy. *Philosophical Magazine Letters*. 2011, vol. 91, no. 10, pp. 690–696.

[70] CHINO, Y., M. MABUCHI, S. HAGIWARA, H. IWASAKI, A. YAMAMOTO and H. TSUBAKINO. Novel equilibrium two phase Mg alloy with the long-period ordered structure. *Scripta Materialia*. 2004, vol. 51, no. 7, pp. 711–714.

[71] NISHIDA, M., Y. KAWAMURA and T. YAMAMURO. Formation process of unique microstructure in rapidly solidified Mg97Zn1Y2 alloy. *Materials Science and Engineering: A*. 2004, vols. 375–377, pp. 1217–1223.

[72] INOUE, A., M. MATSUSHITA, Y. KAWAMURA, K. AMIYA, K. HAYASHI and J. KOIKE. Novel Hexagonal Structure of Ultra-High Strength Magnesium-Based Alloys. *MATERIALS TRANSACTIONS*. 2002, vol. 43, no. 3, pp. 580–584.

[73] LUO, Z.P. and S.Q. ZHANG. High-resolution electron microscopy on the X-Mg12ZnY phase in a high strength Mg-Zn-Zr-Y magnesium alloy. *Journal of Materials Science Letters*. 2000, vol. 19, no. 9, pp. 813–815.

[74] ONO, A., E. ABE, T. ITOI, M. HIROHASHI, M. YAMASAKI and Y. KAWAMURA. Microstructure Evolutions of Rapidly-Solidified and Conventionally-Cast $Mg_{97}Zn_1Y_2$ Alloys. *MATERIALS TRANSACTIONS*. 2008, vol. 49, no. 5, pp. 990–994.

[75] YOSHIMOTO, S., M. YAMASAKI and Y. KAWAMURA. Microstructure and Mechanical Properties of Extruded Mg-Zn-Y Alloys with 14H Long Period Ordered Structure. *MATERIALS TRANSACTIONS*. 2006, vol. 47, no. 4, pp. 959–965.

[76] TANAKA, R. and K. YUGE. Thermodynamic stability of Mg–Y–Zn ternary alloys through first-principles. *Intermetallics*. 2016, vol. 72, pp. 25–29.

[77] ITOI, T., T. SUZUKI, Y. KAWAMURA and M. HIROHASHI. Microstructure and Mechanical Properties of Mg-Zn-Y Rolled Sheet with a $Mg_{12}ZnY$ Phase. *MATERIALS TRANSACTIONS*. 2010, vol. 51, no. 9, pp. 1536–1542.

[78] HAGIHARA, K., M. HONNAMI, R. MATSUMOTO, Y. FUKUSUMI, H. IZUNO, M. YAMASAKI, T. OKAMOTO, T. NAKANO and Y. KAWAMURA. In-Situ Observation on the Formation Behavior of the Deformation Kink Bands in Zn Single Crystal and LPSO Phase. *MATERIALS TRANSACTIONS*. 2015, vol. 56, no. 7, pp. 943–951.

[79] ITOI, T., T. INAZAWA, M. YAMASAKI, Y. KAWAMURA and M. HIROHASHI. Microstructure and mechanical properties of Mg-Zn-Y alloy sheet prepared by hot-rolling. *Materials Science and Engineering: A*. 2013, vol. 560, pp. 216–223.

[80] MATSUMOTO, R., M. OTSU, M. YAMASAKI, T. MAYAMA, H. UTSUNOMIYA and Y. KAWAMURA. Application of mixture rule to finite element analysis for forging of cast Mg–Zn–Y alloys with long period stacking ordered structure. *Materials Science and Engineering: A*. 2012, vol. 548, pp. 75–82.

[81] MATSUMOTO, R. and M. URANAGASE. Deformation Analysis of the Long-Period Stacking-Ordered Phase by Using Molecular Dynamics Simulations: Kink Deformation under Compression and Kink Boundary Migration under Tensile Strain. *MATERIALS TRANSACTIONS*. 2015, vol. 56, no. 7, pp. 957–962.

[82] MINE, Y., R. MAEZONO, H. ODA, M. YAMASAKI, Y. KAWAMURA and K. TAKASHIMA. Deformation Behavior of Long-Period Stacking Ordered Structured Single Crystals in $Mg_{85}Zn_6Y_9$ Alloy. *MATERIALS TRANSACTIONS*. 2015, vol. 56, no. 7, pp. 952–956.

[83] CHUANG, W.S., C.H. HSIEH, J.C. HUANG, P.H. LIN, K. TAKAGI, Y. MINE and K. TAKASHIMA. Relation between sample size and deformation mechanism in Mg-Zn-Y 18R-LPSO single crystals. *Intermetallics*. 2017, vol. 91, pp. 110–119.

[84] CHUANG, W.S., J.C. HUANG, P.H. LIN, C.H. HSIEH, Y.H. LIN, K. TAKAGI, Y. MINE and K. TAKASHIMA. Deformation mechanisms and mechanical properties of (0001) Mg-Zn-Y 18R-LPSO single crystals. *Journal of Alloys and Compounds*. 2019, vol. 772, pp. 288–297.

[85] CHEN, R., S. SANDLÖBES, C. ZEHNDER, X. ZENG, S. KORTE-KERZEL and D. RAABE. Deformation mechanisms, activated slip systems and critical resolved shear stresses in an Mg-LPSO alloy studied by micro-pillar compression. *Materials & Design*. 2018, vol. 154, pp. 203–216.

[86] MIURA, S., S. IMAGAWA, T. TOYODA, K. OHKUBO and T. MOHRI. Effect of Rare-Earth Elements Y and Dy on the Deformation Behavior of Mg Alloy Single Crystals. *MATERIALS TRANSACTIONS*. 2008, vol. 49, no. 5, pp. 952–956.

[87] HAGIHARA, K., T. NAKANO and Y. UMAKOSHI. Plastic deformation behaviour in Ni3Ti single crystals with D024 structure. *Acta Materialia*. 2003, vol. 51, no. 9, pp. 2623–2637.

[88] HAGIHARA, K., T. TANAKA, T. NAKANO and Y. UMAKOSHI. Plastic deformation behavior of Ni3(Ti0.90Nb0.10) single crystals with the nine-layered ordered rhombohedral structure. *Acta Materialia*. 2005, vol. 53, no. 19, pp. 5051–5059.

[89] HAGIHARA, K., T. TANAKA, T. NAKANO, P. VEYSSIÈRE and Y. UMAKOSHI. Effects of the anisotropy of the anti-phase boundary energy on the yield-stress anomaly in Ni3 X compounds with close-packed crystal structures. *Philosophical Magazine Letters*. 2007, vol. 87, no. 10, pp. 705–712.

[90] OROWAN, E. A TYPE OF PLASTIC DEFORMATION NEW IN METALS. *Nature*. 1942, vol. 149, no. 3788, p. 643.

[91] HESS, J.B. and C.S. BARRETT. Structure and nature of kink bands in zinc. *JOM*. 1949, vol. 1, no. 9, pp. 599–606.

[92] GILMAN, J.J. Mechanism of ortho kink-band formation in Compressed Zinc Monocrystals. *JOM*. 1954, vol. 6, no. 5, pp. 621–629.

[93] EGUSA, D., M. YAMASAKI, Y. KAWAMURA and E. ABE. Micro-Kinking of the Long-Period Stacking/Order (LPSO) Phase in a Hot-Extruded $Mg_{97}Zn_1Y_2$ Alloy. *MATERIALS TRANSACTIONS*. 2013, vol. 54, no. 5, pp. 698–702.

[94] HAGIHARA, K., T. MAYAMA, M. HONNAMI, M. YAMASAKI, H. IZUNO, T. OKAMOTO, T. OHASHI, T. NAKANO and Y. KAWAMURA. Orientation dependence of the deformation kink band formation behavior in Zn single crystal. *International Journal of Plasticity*. 2016, vol. 77, pp. 174–191.

[95] HAGIHARA, K., M. YAMASAKI, M. HONNAMI, H. IZUNO, M. TANE, T. NAKANO and Y. KAWAMURA. Crystallographic nature of deformation bands shown in Zn and Mg-based long-period stacking ordered (LPSO) phase. *Philosophical Magazine*. 2015, vol. 95, no. 2, pp. 132–157.

[96] YAMASAKI, M., K. HAGIHARA, S. INOUE, J.P. HADORN and Y. KAWAMURA. Crystallographic classification of kink bands in an extruded Mg–Zn–Y alloy using intragranular misorientation axis analysis. *Acta Materialia*. 2013, vol. 61, no. 6, pp. 2065–2076.

[97] MATSUMOTO, R., M. URANAGASE and N. MIYAZAKI. Molecular Dynamics Analyses of Deformation Behavior of Long-Period-Stacking-Ordered Structures. *MATERIALS TRANSACTIONS*. 2013, vol. 54, no. 5, pp. 686–692.

[98] PALACHE, C. Contributions to the mineralogy of sterling hill, new jersey: morphology of graphite, arsenopyrite, pyrite, and arsenic. *American Mineralogist*. 1941, vol. 26, no. 12, pp. 709–717.

[99] FREISE E. J., KELLY ANTHONY and COTTRELL ALAN HOWARD. Twinning in graphite. *Proceedings of the Royal Society of London. Series A. Mathematical and Physical Sciences*. 1961, vol. 264, no. 1317, pp. 269–276.

[100] SKINNER, J. and N. GANE. The deformation and twinning of graphite crystals under a point load. *The Philosophical Magazine: A Journal of Theoretical Experimental and Applied Physics*. 1973, vol. 28, no. 4, pp. 827–837.

[101] CROCKER, A.G. and J.S. ABELL. The crystallography of deformation kinking. *The Philosophical Magazine: A Journal of Theoretical Experimental and Applied Physics*. 1976, vol. 33, no. 2, pp. 305–310.

[102] KUHLMANN-WILSDORF, D. Theory of plastic deformation: - properties of low energy dislocation structures. *Materials Science and Engineering: A*. 1989, vol. 113, pp. 1–41.

[103] HALL, E.O. The Deformation and Ageing of Mild Steel: III Discussion of Results. *Proceedings of the Physical Society. Section B*. 1951, vol. 64, no. 9, pp. 747–753.

[104] PETCH, N.J. The Cleavage Strength of Polycrystals. *Journal of the Iron and Steel Institute*. 1953, vol. 174, pp. 25–28.

[105] CHOKSHI, A.H., A. ROSEN, J. KARCH and H. GLEITER. On the validity of the hall-petch relationship in nanocrystalline materials. *Scripta Metallurgica*. 1989, vol. 23, no. 10, pp. 1679–1683.

[106] SURYANARAYANA, C. The structure and properties of nanocrystalline materials: Issues and concerns. *JOM*. 2002, vol. 54, no. 9, p. 24.

[107] *Physical Foundations of Materials Science | Günter Gottstein | Springer*.

[108] GLADMAN, T. Precipitation hardening in metals. *Materials Science and Technology*. 1999, vol. 15, no. 1, pp. 30–36.

[109] OROWAN, E. Zur Kristallplastizität. III. *Zeitschrift für Physik*. 1934, vol. 89, no. 9, pp. 634–659.

[110] SWIOSTEK, J., J. BOHLEN, D. LETZIG and K.U. KAINER. Comparison of Microstructure and Mechanical Properties of Indirect and Hydrostatic Extruded Magnesium Alloys. In: *Magnesium*. B.m.: John Wiley & Sons, Ltd, 2005, pp. 278–284.

[111] SILLEKENS, W.H., J. a. F.M. SCHADE VAN WESTRUM, A.J. DEN BAKKER and P.-J. VET. Hydrostatic Extrusion of Magnesium: Process Mechanics and Performance. *Materials Science Forum*. 2003, vol. 426-432, pp. 629-636.

[112] BOHLEN, J., S. YI, D. LETZIG and K.U. KAINER. Effect of rare earth elements on the microstructure and texture development in magnesium–manganese alloys during extrusion. *Materials Science and Engineering: A*. 2010, vol. 527, no. 26, pp. 7092–7098.

[113] GARCES, G., P. PEREZ, S. CABEZA, H.K. LIN, S. KIM, W. GAN and P. ADEVA. Reverse tension/compression asymmetry of a Mg–Y–Zn alloys containing LPSO phases. *Materials Science and Engineering: A*. 2015, vol. 647, pp. 287–293.

[114] ILLKOVA, K., P. DOBROŇ, F. CHMELÍK, K.U. KAINER, J. BALÍK, S. YI, D. LETZIG and J. BOHLEN. Effect of aluminium and calcium on the microstructure, texture, plastic deformation and related acoustic emission of extruded magnesium–manganese alloys. *Journal of Alloys and Compounds*. 2014, vol. 617, pp. 253–264.

[115] YI, S., J. BOHLEN, F. HEINEMANN and D. LETZIG. Mechanical anisotropy and deep drawing behaviour of AZ31 and ZE10 magnesium alloy sheets. *Acta Materialia*. 2010, vol. 58, no. 2, pp. 592–605.

[116] VICTORIA-HERNANDEZ, J., S. YI, D. LETZIG, D. HERNANDEZ-SILVA and J. BOHLEN. Microstructure and texture development in hydrostatically extruded Mg–Al–Zn alloys during tensile testing at intermediate temperatures. *Acta Materialia*. 2013, vol. 61, no. 6, pp. 2179–2193.

[117] *http://www.substech.com/dokuwiki/doku.php?id=aluminum_extrusion*. Status to the date 23/04/2019.

[118] ALS-NIELSEN, J. and D. MCMORROW. *Elements of Modern X-ray Physics, 2nd Edition*. 2011.

[119] ČAPEK, J. Investigation of basic deformation mechanisms of magnesium alloys by means of advanced in-situ methods and theoretical modeling. *Dissertation thesis*. 2017.

[120] HEIPLE, C.R. and S.H. CARPENTER. Acoustic emission produced by deformation of metals and alloys - A review. *Journal of Acoustic Emission*. 1987, vol. 6, pp. 177–204.

[121] HEIPLE, C.R. and S.H. CARPENTER. Acoustic emission produced by deformation of metals and alloys. II. *Journal of Acoustic Emission*. 1987, vol. 6, pp. 215–237.

[122] STEPHENS RWB, POLLOCK AA. Waveforms and frequency spectra of acoustic emissions. *Journal of the Acoustical Society of America*. 1971, vol. 50, pp. 904-910.

[123] GUMBSCH, P. and H. GAO. Dislocations Faster than the Speed of Sound. *Science*. 1999, vol. 283, no. 5404, pp. 965–968.

[124] SHASHKOV, I. Multiscale study of the intermittency of plastic deformation by acoustic emission method. *Dissertation thesis*. 2012.

[125] DROZDENKO, D., J. ČAPEK, B. CLAUSEN, A. VINOGRADOV and K. MÁTHIS. Influence of the solute concentration on the anelasticity in Mg-Al alloys: A multiple-approach study. *Journal of Alloys and Compounds*. 2019, vol. 786, pp. 779–790.

[126] WELCH, P. The use of fast Fourier transform for the estimation of power spectra: A method based on time averaging over short, modified periodograms.

IEEE Transactions on Audio and Electroacoustics. 1967, vol. 15, no. 2, pp. 70–73.

[127] DROZDENKO, D., J. BOHLEN, F. CHMELÍK, P. LUKÁČ and P. DOBROŇ. Acoustic emission study on the activity of slip and twin mechanisms during compression testing of magnesium single crystals. *Materials Science and Engineering: A*. 2016, vol. 650, pp. 20–27.

[128] GRAFF, S., W. BROCKS and D. STEGLICH. Yielding of magnesium: From single crystal to polycrystalline aggregates. *International Journal of Plasticity*. 2007, vol. 23, no. 12, pp. 1957–1978.

[129] MURÁNSKY, O., M.R. BARNETT, V. LUZIN and S. VOGEL. On the correlation between deformation twinning and Lüders-like deformation in an extruded Mg alloy: In situ neutron diffraction and EPSC.4 modelling. *Materials Science and Engineering: A*. 2010, vol. 527, no. 6, pp. 1383–1394.

[130] AGNEW, S.R., C.N. TOMÉ, D.W. BROWN, T.M. HOLDEN and S.C. VOGEL. Study of slip mechanisms in a magnesium alloy by neutron diffraction and modeling. *Scripta Materialia*. 2003, vol. 48, no. 8, pp. 1003–1008.

[131] MURÁNSKY, O., D.G. CARR, M.R. BARNETT, E.C. OLIVER and P. ŠITTNER. Investigation of deformation mechanisms involved in the plasticity of AZ31 Mg alloy: In situ neutron diffraction and EPSC modelling. *Materials Science and Engineering: A*. 2008, vol. 496, no. 1, pp. 14–24.

[132] STOHR, par J.F. and J.P. POIRIER. Etude en microscopie electronique du glissement pyramidal 1122 〈1123〉 dans le magnesium. *The Philosophical Magazine: A Journal of Theoretical Experimental and Applied Physics*. 1972, vol. 25, no. 6, pp. 1313–1329.

[133] AGNEW, S.R., J.A. HORTON and M.H. YOO. Transmission electron microscopy investigation of 〈c+a〉 dislocations in Mg and α-solid solution Mg-Li alloys. *Metallurgical and Materials Transactions A*. 2002, vol. 33, no. 3, pp. 851–858.

[134] UNGÁR, T. and A. BORBÉLY. The effect of dislocation contrast on x-ray line broadening: A new approach to line profile analysis. *Applied Physics Letters*. 1996, vol. 69, no. 21, pp. 3173–3175.

[135] UNGÁR, T., J. GUBICZA, G. RIBÁRIK and A. BORBÉLY. Crystallite size distribution and dislocation structure determined by diffraction profile

analysis: principles and practical application to cubic and hexagonal crystals. *Journal of Applied Crystallography*. 2001, vol. 34, no. 3, pp. 298–310.

[136] MÁTHIS, K., K. NYILAS, A. AXT, I. DRAGOMIR-CERNATESCU, T. UNGÁR and P. LUKÁČ. The evolution of non-basal dislocations as a function of deformation temperature in pure magnesium determined by X-ray diffraction. *Acta Materialia*. 2004, vol. 52, no. 10, pp. 2889–2894.

[137] MÁTHIS, K., G. CSISZÁR, J. ČAPEK, J. GUBICZA, B. CLAUSEN, P. LUKÁŠ, A. VINOGRADOV and S.R. AGNEW. Effect of the loading mode on the evolution of the deformation mechanisms in randomly textured magnesium polycrystals – Comparison of experimental and modeling results. *International Journal of Plasticity*. 2015, vol. 72, pp. 127–150.

[138] MÁTHIS, K., J. ČAPEK, B. CLAUSEN, T. KRAJŇÁK and D. NAGARAJAN. Investigation of the dependence of deformation mechanisms on solute content in polycrystalline Mg–Al magnesium alloys by neutron diffraction and acoustic emission. *Journal of Alloys and Compounds*. 2015, vol. 642, pp. 185–191.

[139] BAE, S.-H., K.H. JUNG, Y.-C. SHIN, D.J. YOON and M. KAWASAKI. Development of mechanical properties in a CaO added AZ31 magnesium alloy processed by equal-channel angular pressing. *Materials Characterization*. 2016, vol. 112, pp. 105–112.

[140] HA, S.-H., J.-K. LEE, H.-H. JO, S.-B. JUNG and K. KIM SHAE. Behavior of CaO and Calcium in pure Magnesium. *Rare Metals*. 2006, vol. 25, nos. 6, Supplement 2, pp. 150–154.

[141] HA, S.-H., J.-K. LEE and S.K. KIM. Effect of CaO on Oxidation Resistance and Microstructure of Pure Mg. *MATERIALS TRANSACTIONS*. 2008, vol. 49, no. 5, pp. 1081–1083.

[142] LEE, J.-K. and S.K. KIM. Effect of CaO Addition on the Ignition Resistance of Mg-Al Alloys. *MATERIALS TRANSACTIONS*. 2011, vol. 52, no. 7, pp. 1483–1488.

[143] BUZOLIN, R.H., M. MOHEDANO, C.L. MENDIS, B. MINGO, D. TOLNAI, C. BLAWERT, K.U. KAINER, H. PINTO and N. HORT. Corrosion behaviour of as-cast ZK40 with CaO and Y additions. *Transactions of Nonferrous Metals Society of China*. 2018, vol. 28, no. 3, pp. 427–439.

[144] SON, H.-W., J.-W. LEE and S.-K. HYUN. Effects of CaO addition and strain rate on the texture evolution of AZ31 alloy. *Materials Science and Engineering: A*. 2019, vol. 744, pp. 724–732.

[145] SCHWARZER, R.A., D.P. FIELD, B.L. ADAMS, M. KUMAR and A.J. SCHWARTZ. Present State of Electron Backscatter Diffraction and Prospective Developments. MA: Springer US, 2009, pp. 1–20.

[146] MISHRA, S.K., P. PANT, K. NARASIMHAN, A.D. ROLLETT and I. SAMAJDAR. On the widths of orientation gradient zones adjacent to grain boundaries. *Scripta Materialia*. 2009, vol. 61, no. 3, pp. 273–276.

[147] THOMAS, I., S. ZAEFFERER, F. FRIEDEL and D. RAABE. High-Resolution EBSD Investigation of Deformed and Partially Recrystallized IF Steel. *Advanced Engineering Materials*. 2003, vol. 5, no. 8, pp. 566–570.

[148] ALLAIN-BONASSO, N., F. WAGNER, S. BERBENNI and D.P. FIELD. A study of the heterogeneity of plastic deformation in IF steel by EBSD. *Materials Science and Engineering: A*. 2012, vol. 548, pp. 56–63.

[149] *https://en.wikipedia.org/w/index.php?title=Transmission_electron_ microscopy&oldid=887185493*. Status to the date 12/06/2019.

[150] SCHELL, N., A. KING, F. BECKMANN, T. FISCHER, M. MÜLLER and A. SCHREYER. The High Energy Materials Science Beamline (HEMS) at PETRA III. *Materials Science Forum*. 2014, vol. 772, pp. 57-61.

[151] TOLNAI, D., G. SZAKÁCS, G. REQUENA, A. STARK, N. SCHELL, K.U. KAINER and N. HORT. Study of the Solidification of AS Alloys Combining In Situ Synchrotron Diffraction and Differential Scanning Calorimetry. *Materials Science Forum*. 2013, vol. 765, pp. 286-290.

[152] HAMMERSLEY, A.P., S.O. SVENSSON, M. HANFLAND, A.N. FITCH and D. HAUSERMANN. Two-dimensional detector software: From real detector to idealised image or two-theta scan. *High Pressure Research*. 1996, vol. 14, nos. 4–6, pp. 235–248.

[153] BARRIOBERO-VILA, P., J. GUSSONE, K. KELM, J. HAUBRICH, A. STARK, N. SCHELL and G. REQUENA. An in situ investigation of the deformation mechanisms in a β-quenched Ti-5Al-5V-5Mo-3Cr alloy. *Materials Science and Engineering: A*. 2018, vol. 717, pp. 134–143.

[154] WRIGHT, S.I. Fundamentals of Automated EBSD. MA: Springer US, 2000, pp. 51–64.

[155] EGUSA, D. and E. ABE. The structure of long period stacking/order Mg–Zn–RE phases with extended non-stoichiometry ranges. *Acta Materialia*. 2012, vol. 60, no. 1, pp. 166–178.

[156] HORVÁTH, K., D. DROZDENKO, K. MÁTHIS, G. GARCÉS and P. DOBROŇ. Characterization of Active Deformation Mechanisms in Mg Alloys with LPSO Phase. *Acta Physica Polonica A*. 2018, vol. 134, no. 3, pp. 815–819.

[157] GARCES, G., M.A. MUÑOZ-MORRIS, D.G. MORRIS, J.A. JIMENEZ, P. PEREZ and P. ADEVA. The role of extrusion texture on strength and its anisotropy in a Mg-base alloy composed of the Long-Period-Structural-Order phase. *Intermetallics*. 2014, vol. 55, pp. 167–176.

[158] EL-TAHAWY, M., K. MÁTHIS, G. GARCÉS, T. MATSUMOTO, M. YAMASAKI, Y. KAWAMURA and J. GUBICZA. Type and density of dislocations in a plastically deformed long-period stacking ordered magnesium alloy. *Journal of Alloys and Compounds*. 2019, vol. 771, pp. 629–635.

[159] MONGSTAD, T., C. PLATZER-BJÖRKMAN, S.Zh. KARAZHANOV, A. HOLT, J.P. MAEHLEN and B.C. HAUBACK. Transparent yttrium hydride thin films prepared by reactive sputtering. *Journal of Alloys and Compounds*. 2011, vol. 509, pp. S812–S816.

[160] VAN GOGH, A.T.M., D.G. NAGENGAST, E.S. KOOIJ, N.J. KOEMAN, J.H. RECTOR, R. GRIESSEN, C.F.J. FLIPSE and R.J.J.G.A.M. SMEETS. Structural, electrical, and optical properties of La 1 − z Y z H x switchable mirrors. *Physical Review B*. 2001, vol. 63, no. 19, p. 195105.

[161] HUIBERTS, J.N., R. GRIESSEN, J.H. RECTOR, R.J. WIJNGAARDEN, J.P. DEKKER, D.G. de GROOT and N.J. KOEMAN. Yttrium and lanthanum hydride films with switchable optical properties. *Nature*. 1996, vol. 380, no. 6571, pp. 231-234.

[162] VAJDA, P. Chapter 137 Hydrogen in rare-earth metals, including RH2+x phases. In: *Handbook on the Physics and Chemistry of Rare Earths*. B.m.: Elsevier, 1995, pp. 207–291.

[163] GRÖBNER, J., A. KOZLOV, X.Y. FANG, J. GENG, J.F. NIE and R. SCHMID-FETZER. Phase equilibria and transformations in ternary Mg-rich Mg–Y–Zn alloys. *Acta Materialia*. 2012, vol. 60, no. 17, pp. 5948–5962.

[164] ZHU, J., X.H. CHEN, L. WANG, W.Y. WANG, Z.K. LIU, J.X. LIU and X.D. HUI. High strength Mg-Zn-Y alloys reinforced synergistically by Mg12ZnY

phase and Mg3Zn3Y2 particle. *Journal of Alloys and Compounds*. 2017, vol. 703, pp. 508–516.

[165] XU, D.K., W.N. TANG, L. LIU, Y.B. XU and E.H. HAN. Effect of Y concentration on the microstructure and mechanical properties of as-cast Mg–Zn–Y–Zr alloys. *Journal of Alloys and Compounds*. 2007, vol. 432, no. 1, pp. 129–134.

[166] XU, D.K., L. LIU, Y.B. XU and E.H. HAN. Effect of microstructure and texture on the mechanical properties of the as-extruded Mg–Zn–Y–Zr alloys. *Materials Science and Engineering: A*. 2007, vol. 443, no. 1, pp. 248–256.

[167] XU, D.K., W.N. TANG, L. LIU, Y.B. XU and E.H. HAN. Effect of W-phase on the mechanical properties of as-cast Mg–Zn–Y–Zr alloys. *Journal of Alloys and Compounds*. 2008, vol. 461, no. 1, pp. 248–252.

[168] JAIN, A. and S.R. AGNEW. Modeling the temperature dependent effect of twinning on the behavior of magnesium alloy AZ31B sheet. *Materials Science and Engineering: A*. 2007, vol. 462, no. 1, pp. 29–36.

[169] JAIN, J., W.J. POOLE, C.W. SINCLAIR and M.A. GHARGHOURI. Reducing the tension–compression yield asymmetry in a Mg–8Al–0.5Zn alloy via precipitation. *Scripta Materialia*. 2010, vol. 62, no. 5, pp. 301–304.

[170] MÁTHIS, K., J. ČAPEK, Z. ZDRAŽILOVÁ and Z. TROJANOVÁ. Investigation of tension–compression asymmetry of magnesium by use of the acoustic emission technique. *Materials Science and Engineering: A*. 2011, vol. 528, no. 18, pp. 5904–5907.

[171] VINOGRADOV, A. and A. LAZAREV. Continuous acoustic emission during intermittent plastic flow in α-brass. *Scripta Materialia*. 2012, vol. 66, no. 10, pp. 745–748.

[172] MURÁNSKY, O., D.G. CARR, P. ŠITTNER and E.C. OLIVER. In situ neutron diffraction investigation of deformation twinning and pseudoelastic-like behaviour of extruded AZ31 magnesium alloy. *International Journal of Plasticity*. 2009, vol. 25, no. 6, pp. 1107–1127.

[173] CLAUSEN, B., C.N. TOMÉ, D.W. BROWN and S.R. AGNEW. Reorientation and stress relaxation due to twinning: Modeling and experimental characterization for Mg. *Acta Materialia*. 2008, vol. 56, no. 11, pp. 2456–2468.

[174] DROZDENKO, D., J. BOHLEN, S. YI, P. MINÁRIK, F. CHMELÍK and P. DOBROŇ. Investigating a twinning–detwinning process in wrought Mg alloys by the acoustic emission technique. *Acta Materialia*. 2016, vol. 110, pp. 103–113.

[175] SILVA, C.J., A. KULA, R.K. MISHRA and M. NIEWCZAS. Mechanical properties of Mg-Sc binary alloys under compression. *Materials Science and Engineering: A*. 2017, vol. 692, pp. 199–213.

[176] BOHLEN, J., P. DOBRON, L. NASCIMENTO, K. PARFENENKO, F. CHMELIK and D. LETZIG. The Effect of Reversed Loading Conditions on the Mechanical Behaviour of Extruded Magnesium Alloy AZ3. *Acta Physica Polonica A*. 2012, vol. 122, no. 3, pp. 444–449.

[177] DOBROŇ, P., F. CHMELÍK, K. PARFENENKO, D. LETZIG and J. BOHLEN. On the effect of the extrusion speed on microstructure and plastic deformation of ZE10 and ZEK100 magnesium alloys - An acoustic emission study. *Acta Physica Polonica A*. 2012, vol. 122, no. 3, pp. 593–596.

[178] YIN, D.L., J.T. WANG, J.Q. LIU and X. ZHAO. On tension–compression yield asymmetry in an extruded Mg–3Al–1Zn alloy. *Journal of Alloys and Compounds*. 2009, vol. 478, no. 1, pp. 789–795.

[179] SHAO, X.H., Z.Q. YANG and X.L. MA. Strengthening and toughening mechanisms in Mg–Zn–Y alloy with a long period stacking ordered structure. *Acta Materialia*. 2010, vol. 58, no. 14, pp. 4760–4771.

[180] MATSUDA, M., S. II, Y. KAWAMURA, Y. IKUHARA and M. NISHIDA. Interaction between long period stacking order phase and deformation twin in rapidly solidified Mg97Zn1Y2 alloy. *Materials Science and Engineering: A*. 2004, vol. 386, no. 1, pp. 447–452.

[181] SHAO, J., Z. CHEN, T. CHEN, Z. HU, X. ZHOU and C. LIU. The effect of LPSO on the deformation mechanism of Mg–Gd–Y–Zn–Zr magnesium alloy. *Journal of Magnesium and Alloys*. 2016, vol. 4, no. 2, pp. 83–88.

[182] TORONCHUK, J.P. ACOUSTIC EMISSION DURING TWINNING OF ZINC SINGLE CRYSTALS. *Materials Evaluation*. 1977, vol. 35, no. 10, pp. 51–53.

[183] VINOGRADOV, A., D. ORLOV, A. DANYUK and Y. ESTRIN. Effect of grain size on the mechanisms of plastic deformation in wrought Mg–Zn–Zr alloy revealed by acoustic emission measurements. *Acta Materialia*. 2013, vol. 61, no. 6, pp. 2044–2056.

[184] LOU, X.Y., M. LI, R.K. BOGER, S.R. AGNEW and R.H. WAGONER. Hardening evolution of AZ31B Mg sheet. *International Journal of Plasticity*. 2007, vol. 23, no. 1, pp. 44–86.

[185] BOHLEN, J., F. CHMELÍK, P. DOBROŇ, D. LETZIG, P. LUKÁČ and K.U. KAINER. Acoustic emission during tensile testing of magnesium AZ alloys. *Journal of Alloys and Compounds*. 2004, vol. 378, no. 1, pp. 214–219.

[186] MIRZA, F.A., D.L. CHEN, D.J. LI and X.Q. ZENG. Low cycle fatigue of a rare-earth containing extruded magnesium alloy. *Materials Science and Engineering: A*. 2013, vol. 575, pp. 65–73.

[187] GARCÉS, G., E. OÑORBE, P. PÉREZ, I.A. DENKS and P. ADEVA. Evolution of internal strain during plastic deformation in magnesium matrix composites. *Materials Science and Engineering: A*. 2009, vol. 523, no. 1, pp. 21–26.

[188] GARCÉS, G., E. OÑORBE, P. PÉREZ, M. KLAUS, C. GENZEL and P. ADEVA. Influence of SiC particles on compressive deformation of magnesium matrix composites. *Materials Science and Engineering: A*. 2012, vol. 533, pp. 119–123.

[189] TANE, M., Y. NAGAI, H. KIMIZUKA, K. HAGIHARA and Y. KAWAMURA. Elastic properties of an Mg–Zn–Y alloy single crystal with a long-period stacking-ordered structure. *Acta Materialia*. 2013, vol. 61, no. 17, pp. 6338–6351.

[190] AGNEW, S.R., D.W. BROWN and C.N. TOMÉ. Validating a polycrystal model for the elastoplastic response of magnesium alloy AZ31 using in situ neutron diffraction. *Acta Materialia*. 2006, vol. 54, no. 18, pp. 4841–4852.

[191] GHARGHOURI, M.A., G.C. WEATHERLY, J.D. EMBURY and J. ROOT. Study of the mechanical properties of Mg-7.7at.% Al by in-situ neutron diffraction. *Philosophical Magazine A*. 1999, vol. 79, no. 7, pp. 1671–1695.

[192] AGNEW, S.R., R.P. MULAY, F.J. POLESAK, C.A. CALHOUN, J.J. BHATTACHARYYA and B. CLAUSEN. In situ neutron diffraction and polycrystal plasticity modeling of a Mg–Y–Nd–Zr alloy: Effects of precipitation on individual deformation mechanisms. *Acta Materialia*. 2013, vol. 61, no. 10, pp. 3769–3780.

[193] OÑORBE, E., G. GARCÉS, P. PÉREZ, S. CABEZAS, M. KLAUS, C. GENZEL, E. FRUTOS and P. ADEVA. The evolution of internal strain in

Mg–Y–Zn alloys with a long period stacking ordered structure. *Scripta Materialia*. 2011, vol. 65, no. 8, pp. 719–722.

[194] RICHETON, T., P. DOBRON, F. CHMELIK, J. WEISS and F. LOUCHET. On the critical character of plasticity in metallic single crystals. *Materials Science and Engineering: A*. 2006, vol. 424, no. 1, pp. 190–195.

[195] YOSHINAGA, H., T. OBARA and S. MOROZUMI. Twinning deformation in magnesium compressed along the C-axis. *Materials Science and Engineering*. 1973, vol. 12, no. 5, pp. 255–264.

[196] PAUFLER, P. W. F. HOSFORD. The mechanics of crystals and textured polycrystals. *Oxford University Press*, New York–Oxford 1993.

[197] REED-HILL, R.E. A study of the {1011} and {1013} twinning modes in magnesium. *Transaction of the Metallurgical Society of Aime*. 1960, vol. 218, pp. 554–558.

[198] YOSHIDA, K. Prediction of ductile fracture induced by contraction twinning in AZ31 sheet subjected to uniaxial and biaxial stretching modes. *International Journal of Plasticity*. 2016, vol. 84, pp. 102–137.

[199] KOIKE, J. Enhanced deformation mechanisms by anisotropic plasticity in polycrystalline Mg alloys at room temperature. *Metallurgical and Materials Transactions A*. 2005, vol. 36, no. 7, pp. 1689–1696.

[200] ARSENAULT, R.J. and M. TAYA. Thermal residual stress in metal matrix composite. *Acta Metallurgica*. 1987, vol. 35, no. 3, pp. 651–659.

[201] GARCÉS, G., G. REQUENA, D. TOLNAI, P. PÉREZ, P. ADEVA, J.A. JIMÉNEZ, A. STARK and N. SCHELL. Coeficiente de dilatación térmica de la fase LPSO. *Revista de Metalurgia*. 2015, vol. 51, no. 2, p. 043.

[202] GARCES, G., M.A. MUÑOZ-MORRIS, D.G. MORRIS, P. PEREZ and P. ADEVA. Optimization of strength by microstructural refinement of MgY2Zn1 alloy during extrusion and ECAP processing. *Materials Science and Engineering: A*. 2014, vol. 614, pp. 96–105.

[203] HUGHES, D.A. and N. HANSEN. The microstructural origin of work hardening stages. *Acta Materialia*. 2018, vol. 148, pp. 374–383.

[204] HAGIHARA, K., Z. LI, M. YAMASAKI, Y. KAWAMURA and T. NAKANO. Strengthening mechanisms acting in extruded Mg-based long-period stacking ordered (LPSO)-phase alloys. *Acta Materialia*. 2019, vol. 163, pp. 226–239.

[205] GONG, W., K. AIZAWA, S. HARJO, J. ABE, T. IWAHASHI and T. KAMIYAMA. Neutron Diffraction on LPSO Structure in Mg-Zn-Y Alloys. *MATERIALS TRANSACTIONS*. 2013, vol. 54, no. 6, pp. 974–976.

[206] ION, S.E., F.J. HUMPHREYS and S.H. WHITE. Dynamic recrystallisation and the development of microstructure during the high temperature deformation of magnesium. *Acta Metallurgica*. 1982, vol. 30, no. 10, pp. 1909–1919.

[207] KOCKS, U.F. and D.G. WESTLAKE. The importance of twinning for the ductility of CPH polycrystals. *Transaction of the Metallurgical Society of Aime*. 1967, vol. 239, pp. 1107–1109.

[208] HAGIHARA, K., Y. FUKUSUMI, M. YAMASAKI, T. NAKANO and Y. KAWAMURA. Non-Basal Slip Systems Operative in $Mg_{12}ZnY$ Long-Period Stacking Ordered (LPSO) Phase with 18R and 14H Structures. *MATERIALS TRANSACTIONS*. 2013, vol. 54, no. 5, pp. 693–697.

[209] HORVÁTH, K., D. DROZDENKO, K. MÁTHIS, G. GARCÉS and P. DOBROŇ. Acoustic Emission Study of High Temperature Deformation of Mg–Zn–Y Alloys with LPSO Phase. *Magnesium Technology 2018*. 2018, pp. 203–208.